

Many-Body Dynamics of Ultracold Atoms in Optical Lattices

INAUGURAL-DISSERTATION

von

Carlos Alberto Parra Murillo

Many-Body Dynamics of Ultracold Atoms in Optical Lattices

INAUGURAL-DISSERTATION

zur Erlangung der Doktorwürde
der Naturwissenschaftlich-Mathematischen Gesamtfakultät
der Ruprecht-Karls-Universität Heidelberg

vorgelegt von
MSc.-Phys. Carlos Alberto Parra Murillo
aus Medellín, Kolumbien

Tag der mündlichen Prüfung: 29. Mai 2013

Many-Body Dynamics of Ultracold Atoms in Optical Lattices

Gutachter:

PD Dr. Sandro Wimberger

Prof. Dr. Jürgen Berges

... to Maria Pastora, Natalia and Sophia

Acknowledgment

It has been a long way to finally arrive to this point and I would like to thank to all that people who made this possible. Unfortunately this page is not enough to mention all of them.

First at all, I am very grateful to my supervisor, Dr. Sandro Wimberger, for the possibility to work in his group and for introducing me in this very interesting field of ultracold atoms. I thank him for supporting my ideas along these three years and also for providing contact with many researchers working in this and related fields. I would also like to thank him for many suggestions, the proofreading of my thesis, and comments during this project.

I am greatly thankful to Dr. Javier Madroñero for his precious guidance, especially concerning to the implementation of sophisticated numerical methods for diagonalization and time evolution. I thank him for his ideas on spectral analysis and the proofreading part of my thesis and his comments. Special gratitude is devoted to Patrick Plötz for providing me his the code, for his help in how to use it and for several good discussions. I would like also to thank him for the friendship and his kind help at my arrival in Germany.

Furthermore I would like to thank Prof. Dr. Jürgen Berges for being the second referee of my thesis. I also wish to express my gratitude to the Graduate School of Fundamental Physics in Heidelberg and in particular to Sonja Bartsch, Melanie Steiert, Gesine Heinzelmänn and Prof. Sandra Klevansky for their kind support and encouragements.

My days in Heidelberg would not have been so nice without the people, friends and colleagues I met here: Ghazal Tayebirad, Georgios Kordas, Stephan Burkhart, Mathias Kraft, Anton Ivanov, Felix Ziegler, Sara Tegami, Boris Novak, Julia Link, Fabian Rolando, Santiago Casas, Alda Arias, Macla, Camilo, Maria P. Gonzalez, Gabriela and Rainer Hopp, Katharina Hopp, Chahan, Gonzalo Cabal, Carlos Granados, Julia Campos and Sofia Mayorca. They made of my days something especial and funny. To my colleagues: thank you very much for the very pleasant working environment at the office -108 (Sparta), at ITP19.

Quiero especialmente agradecerles mis ex-orientadores Prof. Paulo Sérgio Soares Guimarães and Prof. Herbert Vinck por sus enseñanzas, consejos y mi previa formación científica.

Que hubiera sido de mi vida en el viejo continente y anteriormente en Brasil de no haber tenido la oportunidad de conocer a mis grandes amigos Claudia Schneider y Guilherme Tosi. A ellos les agradezco sus consejos, su apoyo y su compañía durante este largo camino lejos de casa. A mi querida Sophia Hopp, por su inmensa paciencia, amor y compañía. Sus sonrisas siempre llenaron de alegría días y momentos de grandes dificultades.

Muy especialmente a mi Madre Maria Pastora y mi hermana Natalia que en la distancia siempre me han apoyado y están ahí para levantarme con su amor y consejos.

Carlos Alberto Parra Murillo
Heidelberg, March 2013

Zusammenfassung

Wir untersuchen komplexe Vielteilchensysteme, welche aus ultrakalten bosonischen Atomen in optischen Gittern bestehen. Motiviert durch neueste Experimente, die auf kontrollierte Weise höhere Energiebänder mit ultrakalten Atomen bevölkern, sollen die physikalischen Eigenschaften und auftretenden Phänomene in einem Szenario beschrieben werden, das aus den beiden untersten Bloch-Bändern besteht. In diesem Zusammenhang verwenden wir eindimensionale bichromatische optische Gitter, deren leicht zu verändernde Eigenschaften die Implementierung eines gut isolierten Zwei-Band Systems erlauben. Die zugrunde liegenden Ein- und Vielteilchenphysik wird mit Hilfe eines Zwei-Band-Bose-Hubbard-Hamiltonians untersucht. Zudem wird eine externe Kraft eingeführt, die die Interbanddynamik treibt. Dieses Vielteilchen-Wannier-Stark-System wird durch das numerische Studium seiner spektralen und dynamischen Eigenschaften in Bezug auf wichtige Systemparameter charakterisiert. Relaxation und kontrollierte nicht-adiabatische Dynamik über die spektralen Resonanzen werden durch Quantum Sweeps untersucht. Zusätzlich implementieren wir einen effektiven Hamiltonian, um die spektralen Eigenschaften eines eindimensionalen optischen Gitters mit kontrollierter Dissipation zu charakterisieren. Wir zeigen, dass die Stabilität langlebiger lokalisierter Vielteilchenzustände, d.h. diskreter solitonischer Zustände, mit guter Genauigkeit durch Zerfallraten des komplexen Spektrums des effektiven (nicht-hermiteschen) Hamiltonians beschrieben werden kann.

Abstract

In this work, we study complex many-body systems consisting of ultracold bosonic atoms in optical lattices. Motivated by the state-of-the-art of experiments realizing higher bands physics with ultracold atoms, we use a one-dimensional bichromatic optical lattice, whose properties permit to engineer a very well isolated two-band system. The underlying single- and many-particle physics is investigated based on a two-band Bose-Hubbard Hamiltonian. An external Stark force is introduced to drive the inter-band dynamics. In a first, and main part of this work, we numerically characterize our many-body Wannier-Stark system through its spectral and dynamical properties, in terms of important system parameters. We present a detailed study of the diffusion in Hilbert space. Relaxation and controlled non-adiabatic dynamics are studied by driving the system across the spectral resonances, mainly by using quantum sweeps. In a second part, we implement an effective Hamiltonian in order to characterize the spectral properties of a leaky one-dimensional optical lattice with controlled dissipation. We show that the stability of long-lived localized many-body states, i.e. discrete solitonic states, can be described with good accuracy by the decay rates statistics of the accessible complex energy spectrum of the effective (non-hermitian) Hamiltonian.

Contents

1	Introduction	xi
2	Preliminaries	3
2.1	Ultracold Atoms in Optical Lattices	3
2.1.1	Bose-Einstein Condensation	3
2.1.2	Optical Lattices	4
2.2	Tight-Binding Approach	7
2.2.1	The Wannier-Stark System: Some Known Results	8
2.3	The Bose-Hubbard Hamiltonian	10
2.3.1	Two-Band Many-Body Wannier-Stark Hamiltonian (TBMWSH)	12
2.3.2	Quantum Chaos and the Bose-Hubbard Model	13
2.3.3	On the Mean-Field Description	14
2.4	Experimental Realizations	16
3	Many-Body Wannier-Stark System: Spectral Analysis	19
3.1	Our System	19
3.1.1	Two-Band Many-Body Wannier-Stark Hamiltonian (TBMWSH)	19
3.2	Static Analysis of the TBMWSH	22
3.2.1	Non-interacting Many-Body Hamiltonian: The Manifold Approach	23
3.2.2	Effects of the Interparticle Interaction	30
3.2.3	Emergence of Quantum Chaos	43
3.3	Summary	49
4	Many-Body Wannier-Stark System: Dynamical Analysis	51
4.1	Adiabatic Theorem and Landau-Zener Transitions	51
4.2	Ergodicity and Mixing	54
4.3	Spectral Diffusion in the Many-body Interacting Regime	56
4.3.1	Local Sweeps	61
4.3.2	Global Sweeps	69
4.4	Summary	73
5	An Open Many-Body System: Decay-rate Analysis	75
5.1	Non-Hermitian Approach to a Noisy Bose-Hubbard Model	75
5.2	A Dissipative Bose-Hubbard System	76
5.2.1	A Spectral Approach	77
5.3	Summary	84
	APPENDIX	89

A	Band Structure, Wannier functions and Bose-Hubbard Parameters	91
A.1	Band Structure	91
A.2	Wannier Functions	94
A.3	Seed basis and Bose-Hubbard Parameters	95
B	Floquet-Lanczos Diagonalization	99
B.1	Floquet Bose-Hubbard Hamiltonian	99
B.2	Lanczos Algorithm	100
C	Random Matrix Theory: Some Tools	105
C.1	Random Matrix Theory	105
D	AC Detection by Fidelity Change	109
D.1	Fidelity Change	109
	BIBLIOGRAPHY	111

Chapter 1

Introduction

In modern physics, especially in quantum mechanics, strongly correlated systems are intrinsically related to the concept of complexity. The rapid development of high precision experimental techniques allows one nowadays to investigate more in detail a huge variety of complex systems, for instance, their physical properties and new phenomena. One can also test fundamental theories and predictions. A remarkable example is the experimental realization of the so-called Bose-Einstein condensate (BEC), first proposed in 1924(5) by S. Bose [1] and A. Einstein [2]. This macroscopic state was experimentally reported, after more than 50 years, for several groups in the 90's [3–6]. BECs and ultracold atoms have opened a new road for understanding the microworld in more clean manner. Their many applications and emerging effects have capture the attention of many experimental and theoretical groups around the world and it is still a field in progress [7–10].

In this framework, *Quantum simulation* is a fundamental and very exciting concept, which was first suggested by Feynman in 1982 [11]. It states that the properties of complex systems can be better understood by engineering analogous (and easier to handle) systems, which mimic the properties of the original ones. In this manner, we have seen that paradigms as the quantum electronic transport in semiconductors can be emulated by using ultracold bosonic atoms trapped in completely controllable optical potentials. An increasing number of single and many-particle phenomena has been already realized in experiments, for instance, one can find, among others: atomic Bloch oscillations, Landau-Zener transitions, dark and bright solitonic states and Josephson oscillations. There are still a number of realizable systems and effects that might be not only simulated, but further investigated in the near future [7, 9].

Throughout the last decade much attention was paid to weakly interacting systems, for which the fundamental physics is amazingly described through mean field approaches as, for instance, the Gross-Pitaevskii equation. Now, in the regime of strong atom-atom interaction, single-band Bose-Hubbard-type Hamiltonians in 1D, 2D and 3D are standard approaches due to their accurated description of the phenomenology of in this kind of systems [7, 9, 12]. Some of the most interesting effects reported in the last years are: simulation of phenomena as quantum magnetic phase transitions [13] and magnetic frustration [14], artificial strong magnetic fiels [15] and Higgs modes [16]. All this offers an unique opportunity for further studies on single- and many-particle dynamics by, for instance, tuning different system parameters, which makes possible real time dynamical passages across critical points [17] or regions characterized by strong spectral correlations, i.e. by *avoided crossings* [18–21]. To study this type of controlled processes, nowadays a very powerful method is the *quantum quench/sweep*. This permits to address investigations on time-dependent phenomena as diffusion in Hilbert space, dynamical relaxation and macroscopic properties of isolated quantum systems, say, statistical equilibrium and further thermalization [22–24].

This Work

In this thesis, we investigate two complex many-body systems consisting of ultracold atoms in optical lattices, motivated by the state-of-the-art of experiments investigating higher band physics [25, 26] and controlled dissipation [27–29]. We especially focus our attention on the following two paradigms of the many-body physics: (i) the two-band many-body Wannier-Stark problem, and (ii) a leaky one-band many-body lattice system.

For the former, we use an one-dimensional bichromatic optical lattice, in order to isolate the two-lowest Bloch energy bands. The underlying physics is then investigated based on a Bose-Hubbard Hamiltonian. We numerically study its spectral properties, in terms of a few system parameters. Diffusion, localization, relaxation towards equilibrium and controlled non-adiabatic dynamics are just examples of the physical phenomena that can be studied in our system. For different initial conditions, we drive our system across the spectral resonances. This is usually done by quantum sweeps/quenches in various realistic scenarios. For the open system, we implement an effective Hamiltonian in order to characterize the spectral properties of a one-dimensional optical lattice with spatially controlled dissipation.

This thesis is organized as follows:

Chapter 2: This chapter provides the fundamental concepts, ideas and basic physics of ultracold bosonic atoms and optical lattices. We introduce the many-body problems that are studied in chapters 3, 4 and 5, along with an overview of previous results. A brief state-of-the-art of experiments with ultracold atoms is presented in order to motivate our investigation.

Chapter 3: In this chapter we formally introduce our main system, the main questions and the numerical techniques used to study the spectral properties of a two-band Many-Body Wannier-Stark problem. We introduce the *manifold approach* based on the concept of occupation numbers, which allows a clear understanding of the many-body eigenspectrum. Through this method we establish the conditions for the onset of spectral mixing, non-integrability and quantum chaos, in terms of experimentally motivated parameters. We show that it is possible to make predictions about the dynamical effects as relaxation towards equilibrium. In addition, we generalize the method in [30] to characterize spectral regions with high degree of mixing, due to the presence of a cluster of avoided crossings.

Chapter 4: This chapter is devoted to the dynamical analysis of the Many-Body Wannier-Stark system. We study the inter-band transport and the relaxation processes by sweeping the system essentially across resonances. To do this, we define the Stark force as a time-dependent parameter. Thus we investigate the role of the initial states in the dynamics. We show that mostly all predictions from chapter 3 are consistent with the analysis in time-domain. We show the high sensitivity of the dynamics on the spectral properties, especially, when the non-integrability takes place. The equivalence between the various definitions of equilibrium state is established and its connection to the manifold approach.

Chapter 5: This chapter presents the study of a single-band many-body system, which is open by controlled *in-situ* dissipation. We show that by the study of the complex quantum spectrum, one can recognize and characterize quantum macroscopic states, and their properties in terms of the system parameters. We show that predictions about the dynamical behaviour can be still done from the complex spectrum as in the previous chapters (see refs. [31, 32]).

Chapter 5.3: In this last chapter we summarize the findings, present the conclusions and open questions for future researches.

2.1 Ultracold Atoms in Optical Lattices

Atomic gases near to the absolute zero temperature and optical lattices created by the interference of counter-propagating laser beams form together one of the cleanest systems created in the laboratory. In fact, these setups allow one to emulate physical phenomena ranging from molecular systems [33–35] to the manipulation of single atoms with high precision [27–29, 36]. Ultracold atoms in optical lattices have been used as a toy model for both, experimental and theoretical investigations, to improve the understanding of fundamental theories of the modern physics. For instance, today one of the most challenging issues is the understanding of phenomena as superfluidity and superconductivity [37].

In this thesis, we study complex many-body systems, which are modeled by using ultracold atoms in optical lattices. Therefore, we aim this introductory chapter to present basic concepts which shall be used throughout this work, in order to help the reader to understand better the methods, statements and findings that will be exposed along, mainly, in the next two chapters. Here we revisit some well-known results connected with the study of many-body systems and end up with a brief overview of the experimental state-of-the-art, in order to put our system in the framework of future experimental realizations of strongly correlated quantum systems.

2.1.1 Bose-Einstein Condensation

An atomic cloud, at temperature T , is predicted to undergo a phase transition when the de-Broglie wavelength of the characteristic thermal motion,

$$\lambda_{dB} = \sqrt{\frac{2\pi\hbar^2}{Mk_B T}}, \quad (2.1)$$

is of the order of the mean interparticle distance, $d = \rho^{-1/3}$, where ρ is the density of the gas. M is the mass of the atomic cloud, k_B is the Boltzmann constant and \hbar is the Planck's constant. In this process the ground state of the system becomes macroscopically occupied and the atoms form coherent "giant" matter wave giving thus rise to one of the most interesting state of the matter, the so-called *Bose-Einstein condensate* [38]. This phenomenon was firstly studied by Bose [1] and Einstein [2] in the 1920s for ideal gases which obey the Bose-Einstein statistics. In the experiments, it was only observed after more than 60 years in a series of experiments (Cornell [3,4], Ketterle [5] and Bradley [6]) in 1995, using different atomic vapors, say, rubidium, sodium and lithium respectively.

The theory states that a non-interacting gas at $T = 0$ consisting of a total particle number N can be described by the product of single particle wave functions $\phi(\vec{r})$:

$$\psi(\vec{r}_1, \vec{r}_2, \dots, \vec{r}_N) = \prod_{i=1}^N \phi(\vec{r}_i). \quad (2.2)$$

The Bose-Einstein condensate is thus described by the macroscopic wave function $\Psi(\vec{r})$ [39], or also referred to as the *order parameter*. This is simply the wave function of the time-independent Schrödinger equation for the single particle lowest energy state of a confining potential, in which the condensation phenomenon takes place. This macroscopic quantum state is affected by the internal atomic interaction and also by the shape of the confining potential.

In a dilute gas the dominating atomic interactions are the inelastic binary collisions, or two-body interactions, which are treated in the context of the scattering theory. At the first two-body level, the interaction between the atoms is described by the Van der Waals potential $V(r) = -C_6/r^6$ [7], which captures the main features of the atom-atom interaction. With the help of the Van der Waals coefficient C_6 , it is possible to define the characteristic length $a_c = (2M_r C_6/\hbar^2)^{1/4}$, (M_r is the reduced mass of the two atoms), at which the interaction energy equals the kinetic energy of the atomic motion. At low temperature, the regime of ultracold atoms $\sim 10^{-3}\text{K}$, the relevant collisions are of the *s*-wave type. Therefore, short-range interactions between the confined atoms can be described by the pseudopotential (see [7,8] for details)

$$V_{pp}(r) = g\delta(\vec{r})\frac{\partial}{\partial r}(r\cdots), \quad (2.3)$$

with $g = 4\pi\hbar^2 a/2M_r$, and a defined as the scattering length. In addition, magnetic and optical Feshbach resonances are a very useful tool, since they allow one to tune of the strength of atom-atom interaction via, for instance, resonantly binding states [40, 41]. In this way, one has the facility of working with repulsive (for $a > 0$), attractive (for $a < 0$) or even with no interaction between the atoms [7].

2.1.2 Optical Lattices

Optical lattices are nowadays one of the fanciest systems used in many laboratories around the world to emulate and to investigate strongly correlated many-body quantum systems. Due to the facilities and the high precision at controlling the parameters and geometry of an optical lattice, these systems allow one to construct analogous models of different complex systems. Especially, models of the solid state physics can actually be realized. The idea of quantum simulation has opened a very extense research field (see [7–9] for a review).

An optical lattice belongs to the family of potentials, in which neutral ultracold atoms can be trapped by the interaction between their atomic dipolar momentum and the electric field. The periodic potentials are generated by the interference of counter-propagating laser beams. The spatial period of the resulting standing wave profile is $\lambda/2$, where λ is the wavelength of the laser used. From the theoretical point of view, the interaction between matter (atoms) and light (laser) can be described by the classical Hamiltonian

$$H_{\text{dip}} = \vec{d}_0 \cdot \vec{E}(\vec{r}), \quad (2.4)$$

where \vec{d}_0 is dipolar momentum of the atoms. Thus the force exerted by the electric field on the atoms is given by

$$\vec{F}_{\text{dip}} = \frac{1}{2}\alpha(\omega_L)\nabla[|\vec{E}(\vec{r})|^2], \quad (2.5)$$

2. Preliminaries

with $\alpha(\omega_L)$ standing for the atomic polarizability and ω_L is the field frequency. Due to interaction with the electric field the atoms experience an optical dipole potential given by

$$V_{\text{dip}}(\vec{r}) = \frac{3\pi c^2 \Gamma}{2\omega_0^3 \Delta} \langle |E(\vec{r})|^2 \rangle, \quad (2.6)$$

with $\Delta = \omega_L - \omega_0$ being the detuning between the frequency of the field and the atomic transition frequency ω_0 . Here the atom is treated as two-level system, with decay rate given by Γ . An optical potential is repulsive for the blue detuning $\Delta > 0$ and attractive for the respective red one $\Delta < 0$ [7]. Depending on the profile of the laser used to create the optical potential, the shape of the lattice can be varied. For instance, the simplest potential is generated by a gaussian profile, which results in the dipole potential

$$V_{\text{dip}}(\vec{r}) \simeq -V_0 e^{-2r/\omega_z^2} \sin(k_L z), \quad (2.7)$$

where $k_L = 2\pi/\lambda$ is the recoil momentum of the atoms in the lattice, ω_z is an axial trapping frequency [7] and V_0 is the maximum depth of the potential. 2D and 3D optical lattices can be created by modifying the angle between two- or three counter-propagating laser beams. They are usually set to be orthogonal to each other. In this work, we are interested in an one-dimensional optical lattice generated by superposing two standing waves with spatial periodicities λ and $\lambda/2$ as sketched in Fig. 2.1 (left panel). Our dipole potential reads

$$V(x) = -V_0(\cos(2k_L x) + s_0 \cos(4k_L x + \phi)), \quad \text{with } s_0 = \frac{V_1}{V_0}, \quad (2.8)$$

where ϕ is the phase difference between the two cosinusoidal waves with amplitudes V_0 and V_1 respectively. This engineered potential allows one to isolate the two-lowest Bloch bands of the corresponding band structure, hence we can neglect the effects of the third and higher bands (see Fig. 2.1). This setup is commonly referred to as the miniband structure or bichromatic optical lattice, and its properties can be easily controlled by means of the parameters $s_0 = V_1/V_0$ and ϕ [20, 42].

By adding an external field $V_{\text{ws}}(x) = Fx$ [43], we can thus define the Wannier-Stark system. A standard way to experimentally implement the latter system is done by inducing a shift in the frequencies of the counter-propagating beams. This can be done by using an acusto-optic modulator [9], which results in the induction of an accelerated motion of the final standing wave. Later on we shall show how such an equivalence can be mathematically set through a gauge-type transformation.

Bloch and Wannier Functions

Given a spinless particle in a periodic potential described by the Hamiltonian

$$\hat{H}_0 = -\frac{\hbar^2}{2m_0} \frac{\partial^2}{\partial x^2} + V(x), \quad \text{with } V(x + d_L) = V(x), \quad (2.9)$$

with d_L being the spatial period of the lattice, the respective eigenfunctions of the system are the so-called Bloch functions. They are obtained by multiplying the free particle wave function with an enveloped function which contains the information of the potential $V(x)$, i.e. it has the same periodicity. These functions are given by

$$\psi_k^\beta(x) = e^{ikx} u_k^\beta(x), \quad \text{with } u_k^\beta(x + d_L) = u_k^\beta(x), \quad (2.10)$$

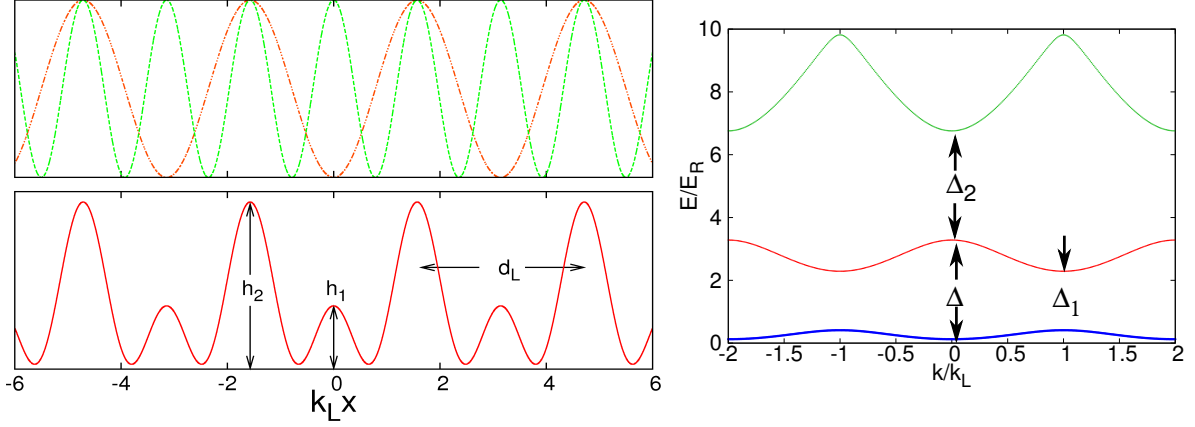


Figure 2.1: (Left) Sketch of the construction of the bichromatic optical lattice in Eq. (2.8). The periodic potential is generated using two optical potentials with wavelength λ and $\lambda/2$. $h_1 = V_0(s_0 - 1)$, $h_2 = V_0(s_0 + 1)$ and d_L represent the two maxima of the potential and the spatial period of the new lattice respectively. (Right) Typical band structure for the potential shown in the left panel. Δ , Δ_1 and Δ_2 represent the energy separation between the Bloch bands at different values of k , which can be modified by the lattice parameters s_0 and ϕ . In this way, it is possible to energetically isolate the two-lowest Bloch bands from the rest of the spectrum (see details in App. A.1).

where k is the magnitude of the momentum of the particle, commonly called quasimomentum. β is the band index. The periodicity of the potential $V(x)$ implies that the eigenenergies of $H\psi_k^\beta(x) = \varepsilon_{\beta,k}\psi_k^\beta(x)$, are also periodic in the quasimomentum space. Therefore, the study of the system properties is reduced to a set of energies lying within the so-called First Brillouin zone (FB), i.e. $\varepsilon_{\beta,k} \in [-\pi/d_L, \pi/d_L)$. The extended spectrum ε vs k is obtained by shifting the momentum by multiples of $2\pi/d_L$. In Fig. 2.1(right panel) we show the respective energy dispersion $\varepsilon(k)$, or band structure of the system, for the bichromatic optical potential in Eq.(2.8). The above treatment is the content of the famous *Bloch theorem*, which was originally introduced by Felix Bloch to describe the behavior of electrons in crystals (see refs. [44, 45]).

Wannier Functions

The Bloch waves defined in Eq. (2.10) are functions extended over the entire lattice system and form a basis of the Hilbert space. Yet, one can introduce a new set of localized functions (*in situ*), which form also a suitable basis of the Hilbert space [46]. An immediate application of these functions is given by the construction of the so-called tight-binding Hamiltonians. These latter are the starting point of different researches on single particle and many-body phenomena within the context of optical lattices.

The Wannier functions are defined as Fourier transform of the Bloch functions Eq. (2.10) as

$$\chi_{\beta,l}(x) = \sqrt{\frac{d_L}{2\pi}} \int_{-1}^1 e^{-ix_l k} \psi_k^\beta(x) dk, \quad (2.11)$$

with $x_l = d_L l$, and l labels the lattice site. The analyticity of the Bloch functions must be guaranteed in order to obtain the optimal highly localized Wannier functions [47]. This nontrivial issue can be solved by setting conveniently the argument of the exponential function in Eq. (2.10), i.e.

2. Preliminaries

by considering a more general definition of the Bloch functions given by

$$\Psi_k^\beta(x) = e^{i\theta(k)} \psi_k^\beta(x), \quad \theta(k + 2\pi/d_L) = \theta(k), \quad (2.12)$$

with an arbitrary periodic function $\theta(k)$. A clever choice of the latter function will bring us to optimally localized Wannier functions which drop exponentially as $|x| > d_L$ [47–50]. That is

$$\lim_{x \rightarrow \pm\infty} \chi_{\beta,l}(x) \sim e^{-h|x|}. \quad (2.13)$$

In App. A.1 we discuss in detail the calculation of both, Bloch and Wannier functions for the bichromatic optical potential defined by Eq. (2.8). Let us now explicitly show the above mentioned application of these functions.

2.2 Tight-Binding Approach

In this section we briefly show the derivation of the tight-binding model. This is one of the most used approaches to study quantum lattice systems, and it is also very useful in solid state physics and condensed matter physics [47]. In order to obtain the tight-binding Hamiltonian \hat{H}_{TB} , we use the Wannier functions (2.11). Every position in the coordinate space can be reached through the translation operator \hat{S}_{x_l} , with $x_l = ld_L$. For simplicity we denote Wannier functions by the ket $|x_l, \beta\rangle$, where β is the band index. A Hamiltonian \hat{H} in the Wannier representation is obtained by using closure and orthonormalization relations of the Wannier functions given by

$$\sum_{l,\beta} |x_l, \beta\rangle \langle x_l, \beta| = \mathbf{1}, \quad \langle x_l, \beta | x_{l'}, \beta' \rangle = \delta_{\beta,\beta'} \delta_{l,l'}, \quad (2.14)$$

as follows

$$\mathbf{1} \hat{H} \mathbf{1} = \sum_{\beta,\beta'} \sum_{l,l'} \langle x_l, \beta | \hat{H} | x_{l'}, \beta' \rangle |x_l, \beta\rangle \langle x_{l'}, \beta'|. \quad (2.15)$$

By using the equation (2.11) with the integral replaced by a summation and the definition of the Bloch functions, we obtain the next relation

$$\begin{aligned} \langle x_l, \beta | \hat{H} | x_{l'}, \beta' \rangle &= \sum_{k,k'} e^{-i(kl-k'l')d_L} \int dx (\psi_{k'}^\beta(x))^* H_0(x) \psi_k^{\beta'}(x) \\ &= \sum_{k,k'} e^{-i(kl-k'l')d_L} \delta(k-k') \delta_{\beta,\beta'} \varepsilon_{\beta,k} \\ &= \delta_{\beta,\beta'} \sum_k e^{-ik(l-l')d_L} \varepsilon_{\beta,k} \equiv E_{l-l'}^\beta. \end{aligned} \quad (2.16)$$

The Hamiltonian is thus reduced to

$$\hat{H}^\beta = E_0^\beta \sum_l |x_l, \beta\rangle \langle x_l, \beta| + \sum_{l,l'} E_{l-l'}^\beta |x_l, \beta\rangle \langle x_{l'}, \beta|, \quad (2.17)$$

where the coefficient $E_{l-l'}^\beta$ drops to zero as a function of $|l-l'|$. For different applications and taking advantage of the localization properties of the Wannier functions, the equation (2.17) can be effectively reduced to the nearest-neighbor problem. This is the *the tight-binding approach* [45], whose Hamiltonian is given by

$$\hat{H}_{TB} = E_0^\beta \sum_l |x_l, \beta\rangle \langle x_l, \beta| + \sum_{\langle l,l' \rangle} J_{l,l'}^\beta |x_l, \beta\rangle \langle x_{l'}, \beta|. \quad (2.18)$$

Here $\langle l, l' \rangle$ denotes the nearest-neighbors, and $J_{l,l'}^\beta$ is the hopping strength between the wells x_l and $x_{l'}$. The symmetry properties of the Wannier functions are given by

$$\chi_{\beta,l}(-x) = (-1)^{\beta-1} \chi_{\beta,l}(x). \quad (2.19)$$

The tight-binding approximation serves to derivate the celebrated Bose-Hubbard Hamiltonian [12], which describes the behavior of ultracold atoms trapped in an optical lattice. We shall see in Chapters 3 and 4, that, under certain conditions, our many-body Hamiltonian can be reduced to a TB-type effective model based on higher band excitations. This shall be done in order to understand the origin of an effect referred to as localization in the energy space, first studied by reported Levitov et. al. [51] and also studied by Izrailev et al. [52, 53]. In addition, the spatial localization of the electron (atom) wave functions in disordered system is also investigated through TB-type Hamiltonians, where the Anderson model is the famous one [54, 55].

2.2.1 The Wannier-Stark System: Some Known Results

Weakly interacting many-body and single particle limits of the Wannier-Stark system have been both, theoretically and experimentally studied by several authors in the meanfield regime [9, 43, 56, 57]. Therein the physics is well described by the nonlinear Schrödinger equation, also called as Gross-Pitaevskii equation. Yet, the scenario of strongly correlated particles in tilted optical lattices was mostly investigated in the single-band approximation [58, 59], where some interesting effects as simulation of quantum Ising chains using ultracold atoms have reported (see ref. [60]). Along with the experiments, there are also different theoretical works where many-body effects in tilted optical lattices have been studied in detail [19, 30, 61, 62].

In this section, we want to summarize some known results, especially for the single particle Wannier-Stark system. The Hamiltonian reads

$$\hat{H}_0 = -\frac{\hbar^2}{2m_0} \frac{\partial^2}{\partial x^2} + V(x) + Fx, \quad \text{with } V(x + d_L) = V(x), \quad (2.20)$$

where F is a static external force, which is usually treated as a control parameter. By using the tight-binding approximation described in the previous section, we rewrite the latter Hamiltonian in the single-band approximation as

$$\hat{H}_{TB} = \sum_l (E_0 + d_L l F) |x_l\rangle \langle x_l| - \frac{J}{2} \sum_{\langle l, l' \rangle} |x_l\rangle \langle x_{l'}|. \quad (2.21)$$

This Hamiltonian can be easily diagonalized and its energy spectrum is found to be given by $\varepsilon_l = E_0 + l d_L F$ [59]. The eigenfunctions are given by

$$|w_l\rangle = \sum_m J_{m-l} \left(\frac{J}{2d_L F} \right) \hat{a}_m^\dagger |0\rangle, \quad (2.22)$$

where $J_{m-l}(x)$ is a Bessel function of the first kind. These states are commonly referred to as Wannier-Stark states, and they are localized functions in the coordinate space at the l th lattice site. Schematically, for a fixed force, the eigenenergies of the Wannier-Stark system represent a set of equidistant states, so-called Wannier-Stark ladder [43] as shown in Fig. 2.2. For every Bloch band one can construct its respective Wannier-Stark ladder, which are energetically separated by an energy gap, as for instance, Δ_g in the two-band approximation introduced in the

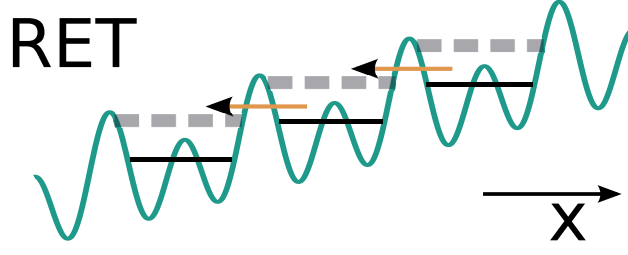


Figure 2.2: Resonantly enhanced tunneling (RET) condition for the nearest neighboring double wells, i.e., for a first order resonance.

previous section. A well-known feature of the Wannier-Stark system is that its respective eigenfunctions are metastable states, because of the unbounded potential Fx . The lifetime of the Wannier-Stark state is given by $\tau_\beta = 1/\Gamma_\beta$, which implies that the eigenenergies must be corrected by adding the complex part as follows

$$\varepsilon_l^\beta = E_\beta + ld_L F - i\frac{\Gamma_\beta}{2}. \quad (2.23)$$

Note that every band has its own decay rate Γ_β . This is schematically represented by the wider single particle levels in Fig. 2.2. In this manner, the Wannier-Stark levels are embedded resonances in a continuum defined by the equation Eq. (2.23). For more details of the calculation of decay rates we suggest the reference [43] and the perturbative approach reported by Tomadin et al. [58] in the many-body scenario.

Bloch oscillations are one of the most interesting phenomena that can be seen in the Wannier-Stark system [63]. Neglecting the effects of higher bands, the evolution of gaussian-shaped initial condition with quasimomentum $k = 0$ (and width $\Delta k \ll FB$) shows that the wave packet undergoes oscillations within the First Brillouin zone. The generating mechanism of this effect is the external force, since it accelerates the wave packet and the period of those oscillations is given by $T_B = 2\pi\hbar/d_L F$. This time scale is usually referred to as the Bloch period.

Landau-Zener Tunneling

A second and very important phenomenon is the Landau-Zener transition, which is also induced by the external field. Through this mechanism, particles lying in the lowest Bloch band can be promoted to higher bands via dynamical quantum tunneling. In this manner, when a system, beforehand performing Bloch oscillations, will undergoes changes in its structure through particle losses. This effect is naturally enhanced when two different Wannier-Stark ladders get close to each other at values of the force approximately given by

$$F_{|l-l'|} \approx \frac{\Delta_{\beta,\beta'}}{d_L |l-l'|}, \quad (2.24)$$

where $\Delta_{\beta,\beta'}$ is the energy separation between the Bloch bands (see Fig. 2.1). l and l' are the lattice sites, whose lower (upper) and upper (lower) single particle levels become degenerate respectively. This scenario is sketched in Fig. 2.2, where the resonant tunneling occurs between states at distance $|l-l'| = 1$. Following the notation from ref. [64], we define $r = |l-l'|$ as the order of resonance with $r \in \mathbb{Z}$. Hereafter, the vicinity of the Stark force F_r will be referred to as

the resonant regime (or RET regime)¹. Plötz et al. [64] has also computed a more accurate formula for the single particle resonance between the two lowest Bloch bands, which contains the dipole-like coupling strength C_0 . This coupling will be defined in the next section. The formula reads

$$F_r = \frac{\Delta_g}{d_L \sqrt{r^2 - 4C_0^2}}. \quad (2.25)$$

In the time-domain, the Bloch oscillations are not completely suppressed by the Landau-Zener transitions. The finite occurrence probability can be obtained using the celebrated Landau-Zener formula [65, 66]

$$P_{LZ} = e^{-\pi/\gamma}, \quad \text{with } \gamma = \frac{4\alpha}{(\Delta E)^2}, \quad (2.26)$$

which is valid only for a two-level system. When two single particle states are coupled via the Stark force, this manifests itself by the appearance of an *avoided crossing* (AC). It means, that the individual levels repel each other since they are not allowed to cross, due to a symmetry breaking occurs. Yet, the avoided crossing is very useful spectral property and it will be amply studied in Chapter 4. This spectral feature allows one to study three different types of dynamical transport, when concerning the promotion of particles to excited states and vice versa (see for example ref. [10]). The latter process can be done, for instance, by suddenly quenching the Stark force F until the resonant positions F_r and afterwards letting the system freely evolves. Another way is by setting the external force as a time-dependent parameter $F(t)$. In this way, one can sweep the system across the avoided crossing of width ΔE , with a predefined sweeping rate α in Eq.(2.26).

Landau-Zener theory allows one to compute the expected decay rate Γ_{LZ} , due to the coupling of the particles with the continuum, via these repeated tunnelling processes. This is given by

$$\Gamma_{LZ} = \frac{\omega_B}{2\pi} \exp \left[-\frac{\pi^2}{32} \frac{\Delta E^2}{d_L F E_R} \right], \quad (2.27)$$

where E_R denotes the recoil energy and $\omega_B = 2\pi/T_B$ (see ref. [67, 68] for details).

So far, we have introduced a very important phenomenon: Landau-Zener tunneling. This defines the main properties of the system that we will study in most of this thesis. Let us now quickly show how ultracold atoms are theoretically studied in the tight-binding regime.

2.3 The Bose-Hubbard Hamiltonian

In this section we sketch the derivation of Bose-Hubbard Hamiltonian. This is a standard procedure, which can be found in different textbooks and in many scientific papers. To begin with, let us consider the spinless single particle Hamiltonian \hat{H}_0 in Eq. (2.9). Here it is worth pointing out that one of the great advantages of the optical lattices is that in those systems the orbital degree of freedom can be separated entirely from spin and charge [7, 25]. We can use the Wannier functions to define field operators

$$\hat{\phi}(x) = \sum_{\beta, l} \chi_{\beta, l}(x) \hat{a}_l^\beta, \quad (2.28)$$

¹RET stands for Resonantly Enhanced Tunneling, see ref. [56] for details.

2. Preliminaries

where β and l are the band and lattice site indexes respectively. To change the representation of our Hamiltonian to the corresponding one in the second quantization formalism, we can use the transformation

$$(\hat{H}) = \int dx \hat{\phi}^\dagger(x) H(x) \hat{\phi}(x). \quad (2.29)$$

The interparticle interaction is considered as a two-body process, which can be described by the pseudopotential (2.3) [7]. For 1D optical potentials the interparticle interaction is given by the formula

$$V_{pp} = g_{1D} \int dx \int dx' \hat{\psi}^\dagger(x') \hat{\psi}^\dagger(x') \delta(x - x') \hat{\psi}(x) \hat{\psi}(x), \quad (2.30)$$

where the interaction strength is given by $g_{1D} = 4\pi a_{1D}/M_r$. a_{1D} is the reduced one-dimensional scattering constant [69]. In the following we set $\hbar = 1$ and the energy unit is given by the recoil energy $E_r = k_L^2/2m$. In addition, we use the rescaling

$$k \rightarrow k/k_L, \quad x \rightarrow k_L x, \quad V_i \rightarrow V_i/E_r. \quad (2.31)$$

By using the field operators in Eq. (2.28), we obtain the following expressions

$$\hat{H}_0 = \sum_{l,l'} \sum_{\beta,\beta'} a_{l,\beta}^\dagger a_{l',\beta'} E_{l-l'}^\beta \delta_{\beta,\beta'} \quad (2.32)$$

$$\hat{V}_{pp} = g_{1D} \sum_{l_1, l_2, l_3, l_4} \sum_{\beta_1, \beta_2, \beta_3, \beta_4} M_{l_1 l_2 l_3 l_4}^{\beta_1 \beta_2 \beta_3 \beta_4} a_{l_1, \beta_1}^\dagger a_{l_2, \beta_2}^\dagger a_{l_3, \beta_3} a_{l_4, \beta_4} \quad (2.33)$$

with the prefactors defined by

$$J_{l-l'}^\beta \equiv \int \chi_\beta^*(x - x_l) H_0(x) \chi_\beta(x - x_{l'}) dx = E_{l-l'}^\beta \quad (2.34)$$

$$M_{l_1 l_2 l_3 l_4}^{\beta_1 \beta_2 \beta_3 \beta_4} \equiv g_{1D} \int \chi_{\beta_1}^*(x - x_{l_1}) \chi_{\beta_2}^*(x - x_{l_2}) \chi_{\beta_3}(x - x_{l_3}) \chi_{\beta_4}(x - x_{l_4}) dx. \quad (2.35)$$

One can thus obtain the corresponding Bose-Hubbard Hamiltonian for an infinite number of bands. In absence of the external fields the Bloch bands can be coupled via the interparticle interaction Eq. (2.33). In the single band approximation the optical potential is engineered to have only one period ($s_0 = 0$ in Eq. (2.8)). The wells of the lattice are deep enough, in order to guarantee that the gap Δ_1 is larger, and the excited bands can be disregarded (see Fig. 2.1). In this way, the single-band Bose-Hubbard Hamiltonian is given by

$$\hat{H} = \sum_{l=1}^L -\frac{J}{2} \left(\hat{a}_{l+1}^\dagger \hat{a}_l + h.c. \right) + \sum_{l=1}^L \frac{W}{2} \hat{n}_l (\hat{n}_l - 1) + \sum_{l=1}^L E_0 \hat{n}_l. \quad (2.36)$$

We shall later on discuss some of the properties of this Hamiltonian, which is mostly used in the chapter 5. Let us now introduce our main system: the many-body Wannier-Stark system based on a two-band Bose-Hubbard model.

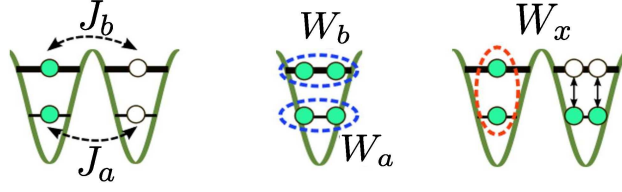


Figure 2.3: The figure sketches the process considered in the two-band many-body approximation described in the main text. We must keep in mind that the potential used in our realization has a double-well structure instead of the single one used in previous works (see for instance Fig. 2.4).

2.3.1 Two-Band Many-Body Wannier-Stark Hamiltonian (TBMWSH)

In analogy with the last section, we can transform the external field $V_{\text{ws}}(x) = Fx$ into the second quantization formalism, by using the field operators (2.28) as follows

$$F(\hat{x}) = d_L F \int \hat{\phi}^\dagger(x) \cdot x \cdot \hat{\phi}(x) dx, \quad (2.37)$$

which in terms of the Wannier functions reads

$$F(\hat{x}) = d_L F \sum_{l,l'} C_{l-l'}^{\beta\beta'} a_{l,\beta}^\dagger a_{l',\beta'}. \quad (2.38)$$

The prefactors given by

$$C_{l-l'}^{\beta\beta'} \equiv \int \chi_\beta^*(x) x \chi_{\beta'}(x - d_L(l-l')) dx = \int \chi_\beta^*(x) x \chi_{\beta'}(x + d_L(l-l')) dx. \quad (2.39)$$

The two-band approximation is obtained by conveniently setting the values for V_0 , s_0 and ϕ in Eq. (2.8). We choose those parameters such that the gap Δ_2 is much larger than the gap between the two lowest Bloch bands, i.e. Δ_1 (Fig. 2.1). The regimes of validity of this approximation are shown in detail in App. A.1. One can notice that the two lowest Bloch bands become flatter as s_0 increases. In this manner, the miniband structure is expected to be a very clean setup with negligible dissipation to higher bands. Under the latter considerations and, by defining the hopping terms (see Fig. 2.3) and the energy gap as

$$J_a \equiv J_1^{\beta=a}, \quad J_b \equiv J_1^{\beta=b}, \quad \Delta_g \equiv \Delta_1 = |E^b - E^a| = |J_0^{\beta=b} - J_0^{\beta=a}|, \quad (2.40)$$

and interparticle interaction as

$$W_a \equiv 2M_{llll}^{1111}, \quad W_b \equiv 2M_{llll}^{2222}, \quad W_x \equiv 2M_{llll}^{1122}, \quad (2.41)$$

the two-band Bose-Hubbard Hamiltonian finally reads

$$\begin{aligned} \hat{H} = & \sum_{\beta=a,b} \left[\sum_{l=1}^L -\frac{J_\beta}{2} (\hat{\beta}_{l+1}^\dagger \hat{\beta}_l + h.c.) + \sum_{l=1}^L \frac{W_\beta}{2} \hat{n}_l^\beta (\hat{n}_l^\beta - 1) \right] \\ & + \sum_{l=1}^L 2W_x \hat{n}_l^a \hat{n}_l^b + \Delta_g \hat{n}_l^b + \frac{W_x}{2} (\hat{b}_l^\dagger \hat{b}_l^\dagger \hat{a}_l \hat{a}_l + h.c.) \end{aligned} \quad (2.42)$$

$$+ \sum_{l=1}^L \sum_{s=0}^2 d_L F C_s (\hat{a}_{l+s}^\dagger \hat{b}_l + h.c.) + d_L F \sum_{l=1}^L \sum_{\beta=a,b} l \hat{n}_l^\beta. \quad (2.43)$$

2. Preliminaries

This is our workhorse that will be used in order to describe physics of the many-body Wannier-Stark system. Here, we label the two lowest Bloch bands by $\beta = a, b$ and $d_L = 2\pi$. The multiple processes involved by our Hamiltonian are sketched in Fig. 2.3 and 2.4. We shall discuss in detail the properties of \hat{H} in Chapter 3. Let us now make a brief overview of some well known and interesting results on chaos in the tilted Bose-Hubbard Hamiltonian.

2.3.2 Quantum Chaos and the Bose-Hubbard Model

Throughout this work, a very important concept of the modern quantum physics will come up recurrently, especially, in Chapters 3 and 4: *Quantum chaos*. This concept has been amply discussed by physicists and mathematicians over more than 40 years, and it has been named in different ways due to the lack of a precise definition. Especially for those systems with few degrees of freedom without classical analogous. Some authors suggest various names, for instance, *Quantum complexity* and *wave chaos* [52], when referring to the appearance of signature of chaos in quantum mechanical systems (see ref. [70] for a review). Chaos in the classical context can be defined as the loss of integrals of motions, or through the study of the *Lyapunov exponents* [71]. For quantum systems, the most accepted definition of chaos is established by the Bohigas-Giannoni-Schmit conjecture [72]. This sets the connection between spectral fluctuation properties of quantum systems that are chaotic in the classical limit, and the predictions from the celebrated random matrix theory (RMT) (see [70, 73, 74] and references therein).

Random matrices were introduced by Wigner in the 1960s [73] to study problems in nuclear physics. Today, RMT is a powerful statistical tool to establish the conditions for the onset of chaos in quantum systems through the analysis of their respective quantum energy spectrum. In this work, we aim to study the spectral properties of the many-body Wannier-Stark system. It shall be shown that in the vicinity of the resonant regime (RET) (Eq.(2.25)), the degree of complexity is drastically enhanced by the interaction. This manifests itself by the presence of large cluster of avoided crossings. In this scenario, RMT predictions become very useful to understand the underlying physics of our many-particle system. Let us now define some robust RMT measures.²

Given the energy spectrum $\{\varepsilon_i\}$ of a Hamiltonian system, random matrix theory predicts that distribution $P(\{s_i\})$ of levels spacings $s_i = (\varepsilon_{i+1} - \varepsilon_i) / \langle \{\varepsilon_{i+1} - \varepsilon_i\} \rangle$ must follow the three following types of gaussian distribution

$$\begin{aligned} P(s) &= \frac{\pi}{2} s \exp\left(-\frac{\pi}{4} s^2\right), & (\text{GOE}), \\ P(s) &= \frac{32}{\pi} s^2 \exp\left(-\frac{4}{\pi} s^2\right), & (\text{GUE}), \\ P(s) &= \frac{2^{18}}{3^6 \pi} s^4 \exp\left(-\frac{64}{9\pi} s^2\right), & (\text{GSE}). \end{aligned} \tag{2.44}$$
$$\tag{2.45}$$

The type of ensemble distribution depends on the properties of the Hamiltonian. If the Hamiltonian matrix is real and symmetric, and invariant under time-reversal operations, the distribution $P(s)$ is expected to be that one for the *Gaussian Orthogonal Ensemble* (GOE). This is usually referred to as *Wigner surmise*. For Hamiltonians with broken time-reversal symmetry, the distribution $P(s)$ follows the *Gaussian Unitary Ensemble* distribution (GUE), and for those systems

² All RMT tools used in this work are summarized in App. C.

with time-reversal symmetry and no rotational symmetry, we have the *Gaussian Symplectic Ensemble* (GSE) distribution [70].

The Bose-Hubbard Hamiltonian possesses a time-reversal symmetry when it is diagonalized in the Fock states basis. Therefore the respective level spacing distribution must be compared to GOE ensemble in the fully chaotic regime. In the last years, Kolovsky et al. [21] studied in detail the spectral properties of the single-band tilted Bose Hubbard Hamiltonian

$$\hat{H} = \sum_{l=1}^L -\frac{J}{2} (\hat{a}_{l+1}^\dagger \hat{a}_l + h.c.) + \sum_{l=1}^L \frac{W}{2} \hat{n}_l (\hat{n}_l - 1) + \sum_{l=1}^L d_L F l \hat{n}_l. \quad (2.46)$$

In this paper it was shown that the Hamiltonian (2.46) undergoes full transition to quantum chaos, when the interparticle interaction W is comparable to the hopping strength J . This is valid for filling factors $N/L \sim 1$ and finite Stark force F . In addition, they reported the existence of a temporal symmetry, when the greatest common divisor of N and L is an integer, i.e. $\text{gcd}(N, L) \in \mathbb{Z}$ (see more details in ref. [59]).

Other authors have amply studied possible extensions of the findings reported by Kolovsky and co-workers. For instance, Tomadin et al. [58, 75] studied a perturbative approach to the open system. They show that by the statistical analysis of the decay rate of the complex eigenenergies, it is possible to infer about the complex dynamics in a Landau-Zener scenario. In another interesting work, H. Venzl et al. [19] reported the existence of robust solitonic-like states, when sweeping the system across the quantum chaotic regions from the energy spectrum. Such a kind of states is also studied by Plötz et al. [30], who show that, up to these latter states, the spectral regions containing a large set of avoided crossings (AC) can be characterized by the RMT distributions for the widths of the AC. Furthermore, it is shown that the quantum fidelity is a very good parameter for ACs detection (see D and C for details).

This is just a short overview showing the big interest of the community to continue studying the Bose-Hubbard-type Hamiltonians due to their overwhelming complexity (see refs. [76–78]), and also because is realizable in experiments [79]. We shall show throughout this work more interesting phenomena that can be understood with effective models.

2.3.3 On the Mean-Field Description

Motivated by the macroscopic occupation of the ground state of the confining potential, the field operator $\hat{\Psi}(\vec{r}, t)$ can be constructed using the wave function of the Bose-Einstein condensate (sec. 2.1.1). This can be replaced by its expectation value as

$$\hat{\Psi}(\vec{r}, t) \approx \sqrt{N_0} \Psi_0(\vec{r}, t) + \delta\hat{\Psi}(\vec{r}, t). \quad (2.47)$$

Here $N_0 \gg 1$ is the occupation number of the ground state. $\Psi_0(\vec{r}, t)$ is a complex function whose modulus represents the condensate density $n_0(\vec{r}, t) = |\Psi_0(\vec{r}, t)|^2$. In the limit of small quantum depletion of the condensate, $\delta\hat{\Psi}(\vec{r}) \rightarrow 0$, the time evolution of the wave function $\Psi_0(\vec{r}, t)$ is obtained through the Heisenberg equation Ansatz:

$$i\hbar \frac{\partial}{\partial t} \hat{\Psi}(\vec{r}, t) = [\hat{\Psi}(\vec{r}, t), \hat{H}]. \quad (2.48)$$

This yields to the famous time-dependent Gross-Pitaevskii equation (GPE)

$$i\hbar \frac{\partial}{\partial t} \Psi_0(\vec{r}, t) = \left(-\frac{\hbar^2}{2m} \nabla^2 + V_{\text{ct}}(\vec{r}) + \tilde{g} |\Psi_0(\vec{r}, t)|^2 \right) \Psi_0(\vec{r}, t), \quad (2.49)$$

2. Preliminaries

where $V_{\text{ct}}(\vec{r})$ is the confining potential and

$$\tilde{g} = \frac{4\pi\hbar^2 a}{m} N = gN, \quad (2.50)$$

with the interaction strength g defined as in the previous section (see ref. [8, 80] for details of the derivation). In the one-dimensional context, the GPE is obtained by replacing $g \rightarrow g_{1D}$. That is, by following the quasi-one-dimensional approximation introduced by Olshanii ref. [69]. Yet, for deep enough optical lattices, the GPE can be reduced to the so-called "tight-binding regime" (sec. 2.2). The equation (2.49) is thus reduced to the discrete nonlinear Schrödinger equation

$$i\hbar \frac{d}{dt} \Psi_{0,l} = J(\Psi_{0,l+1} + \Psi_{0,l-1}) + \tilde{W} |\Psi_{0,l}|^2 \Psi_{0,l} + \epsilon_l \Psi_{0,l}, \quad (2.51)$$

where J is the nearest neighbor coupling, i.e. the hopping. ϵ_n is the linear on-site energy and \tilde{W} is the nonlinear parameter defined by $\tilde{W} = W/N$. These coefficients can be computed by the relations [9]:

$$J \simeq - \int dx \left[\frac{\hbar^2}{2m} (\partial_x \chi_l \cdot \partial_x \chi_{l+1}) + \chi_l V_{\text{ct}} \chi_{l+1} \right] \quad (2.52)$$

$$\epsilon_l = \int dx \left[\frac{\hbar^2}{2m} (\partial_x \chi_l)^2 + V_{\text{ct}} \chi_l^2 \right] \quad (2.53)$$

$$\tilde{W} = g_{1D} N \int dx |\chi_l|^4 \quad (2.54)$$

where $\chi_l(x)$ is the single-band Wannier function defined in Eq. (2.11).

The mean-field limit works out at describing the weakly correlated systems of N particles, with $N \gg 1$. This means that the GPE can equivalently be obtained by rescaling the single-band Bose-Hubbard Hamiltonian (2.46) by the total particle number N . This is done by defining the c -numbers as $\hat{a}/\sqrt{N} \rightarrow c$, where the commutator $[\hat{a}, \hat{a}^\dagger] \rightarrow 0$ as $N \rightarrow \infty$. A surprising effect appears when the effective interaction energy WN beats the hopping strength J . Under this circumstance, the lowest-energy solution of the discrete nonlinear Schrödinger equation is a localized function around one lattice site. This phenomenon is the so-called *discrete self-trapping* and it has been already observed in different laboratories [8, 9]. The dynamics of the Bose-Einstein condensate is characterized by the ratio

$$\Lambda = \frac{WN}{J}, \quad (2.55)$$

and the critical value for *self-trapping* is given by $\Lambda > 2$ [9]. We shall see in Chapter 5 that by the interplay between the nonlinear parameter \tilde{W} and controlled dissipation mechanisms [31, 32], very interesting phenomena take place. For instance, we shall see the formation of many-body solitons. These robust states appear exactly in the *self-trapping* regime. Through the analysis of the quantum spectrum of the metastable many-body system, we show that, one can easily identify relatively stable quantum states, corresponding to previously predicted solitonic many-body structures [31, 32].

So far, we have presented important features and well-known results for Bose-Einstein condensates, and ultracold atoms in optical lattices. This overview concerned mostly the theoretical tools and proposals for the realization of weakly and strongly correlated many-body systems. The next section will be devoted to a short summary of the relevant up-to-date experiments realizing the type of systems studied here.

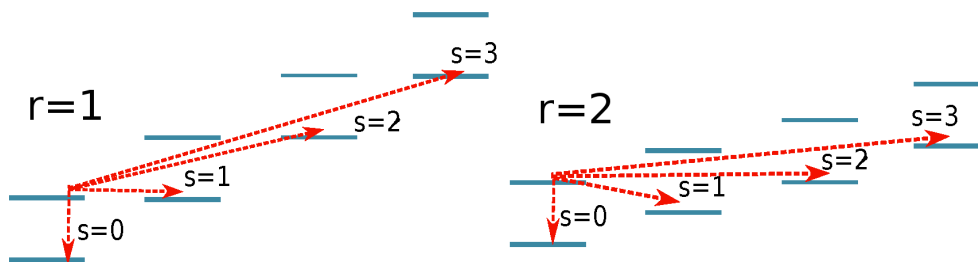


Figure 2.4: Dipole-induced tunneling processes. Every resonance r has $s = 0, 1, \dots, r, r + 1, \dots, L - 1$ inter-band coupling terms with transition strengths FC_s .

2.4 Experimental Realizations

This work presents theoretical results on both, static and dynamical spectral characterization of the two-band many-body Wannier-Stark system. Towards future experimental realizations of our system, we set some reasonable modifications with respect to the model studied by Plötz [81]. These are:

- We engineer our optical lattice to be a periodic chain of double-well traps. This is done by introducing a second lattice with half the spatial period of the original one. This new lattice system is shown in the left panel of Fig. 2.1 along with their respective band structure. As mentioned previously, in order to get rid off of the effects induced by the third and higher bands, our setup can be changed at will using the lattice parameters s_0 and ϕ . With them, and for a not necessarily deep lattice $V_0 \approx 5$ we can make the ratio $\Delta_1/\Delta_2 \ll 1$. This is straightforwardly obtained for $\phi = \pi$ and $s_0 \geq 1$ (see Fig. A.2). Under such a condition the two-band Bose-Hubbard Hamiltonian (2.42) is a very well isolated system.
- The main modification is the introduction of the dipole-induced inter-band couplings with strengths $C_{s>1}$ (see Eq. (A.18)). These transitions are sketched in Fig. 2.4. In previous works, only the transition C_0 has been considered. We shall show the main changes introduced by the additional long-range couplings.

With the rapid advances in the field of ultracold atoms in optical lattices, today there are many different proposals to simulate quantum phenomena. Most of them pay much attention to the underlying physics emulated by the single-band Bose-Hubbard Hamiltonians [7, 9, 12]. Now it is possible to load higher Bloch bands with high precision using different techniques. But in most of the experimental studies used 2D or 3D lattice structures (mainly to map out the respective Brillouin zones). In our case, we consider an one-dimensional system, in which Landau-Zener tunneling is the signature of the participation of higher bands in the dynamics. This phenomenon has been already studied in many different experiments (see [9, 10] for an overview).

Let us make an overview over the experimental ingredients at hand:

Bichromatic Potentials

It is already well established that in experiments with optical lattices there is a high controllability of the parameters. Since the period of the standing wave can be modified using tunable lasers,

2. Preliminaries

to control the spatial period d_L is not a difficult issue. In this way, single particle energy bands (Bloch bands) are nowadays routinely engineered in experiments using a bichromatic optical potential of the kind [82, 83]

$$V(x) = -V_0 [\cos(2k_L x) + s_0 \cos(4k_L x + \phi)].$$

Apart from the observation of atomic Bloch oscillations and Landau-Zener tunneling [9, 10, 56, 57], bichromatic potentials were implemented to study atomic interference in momentum space, the so-called Stückelberg interferometry [83], also reported for a single-periodic optical lattice [84–87].

Ring traps

Boundary conditions are another important ingredient in our system. In the numerical implementation of our Hamiltonian (2.42), we study its gauge-transformed version [59], that allows us naturally to assume periodic boundary conditions (PBC). In that context, our system might be implemented into a ring-shaped optical lattice. Nowadays, there are several observations of trapping of ultracold atoms in ring-shaped potential. For instance, the creation of persistent currents of Bose-Einstein condensates with lifetimes ~ 10 s as reported in refs. [88–91]. Other authors, for example, Gaunt et al. [92], have reported experimental protocols based on digital holography to create atom traps with well defined background potential, i.e. with differently shaped optical confinements.

Tilted potentials and relaxation dynamics

In the literature one can find a number of papers, whose researches are based on the one-band approach. A famous phenomenon was observed by Greiner et. al. [13, 79]. Therein, they reported the simulation of the phase transition between superfluid and Mott-insulator states. Recently, a quantum antiferromagnetic spin chains was experimentally realized by sing tilted optical lattices [60]. It was also experimentally observed that 1D strongly correlated many-particle systems can undergo relaxation towards equilibrium [93]. Theoretical studies on this kind of systems are based often in DMRG simulation [94], which in most of the cases use only for single-band Hamiltonian. In chapter 4, we aim to study the induced relaxation of predefined initial many-body states by means of quantum sweeps and quenches. Our calculations are based on the numerically integration of the time-dependent Schrödinger equation, or on a direct diagonalization of the many-body Hamiltonian (2.42).

Experiments in higher bands

In the framework of tilted periodic potential, Holthaus et al. showed the basis for the experimental realization of well-known phenomena referred to as Bloch oscillation and Landau-Zener transitions using of ultracold atoms [65, 95, 96]. These phenomena that are originally predicted for solid state systems, can already be studied in different experimental setups (see refs. [9, 56] and references within). However, all these works are based on mean-field predictions through the GPE 2.3.3, which is essentially governed by the single particle physics.

As we shall see in the chapters 3 and 4, by including the second band, some other interesting many-body effects can be adressed. These becomes more interesting especially in the

domain of strongly interacting Wannier-Stark ladders. In a recent work by Arimondo et al. [10], it was reported that it is experimentally possible to create protocols to drive quantum systems across an *avoided crossing*, in order to prepare specific quantum states. To be more precise, they studied the super-adiabatic dynamics in a two-level system to obtain high-fidelity of the quantum transformation of the initial state prepared in the ground state into the final excited state. The mechanism for such a population transference is the Landau-Zener tunneling. We shall see that the kind of dynamical evolution presented for this simple system can be implemented in a many-body scenario, as set by our tilted two-band Bose-Hubbard model (2.42). There, the complexity is enhanced due to the clustering of ACs, induced mainly by the interparticle interaction. This is a perfect setup to study multi-state transitions, quantum diffusion and relaxation.

In a more general sense, the interest on the physics of higher Bloch bands has increased in the last years, whether in one-, two- and three dimensional optical lattices. Due to the two-fold, three-fold and higher-order degeneracy of the Wannier states, The creation of exotic states in higher bands (p, d, f -orbitals) has been reported in several experiments [25, 26, 97, 98]. For instance, Wirth et al. [25] showed that by using bosonic rubidium-87 atoms trapped in the s -orbital of 2D optical lattice, it is possible to promote the atoms to the p -orbital via resonant tunneling. The lifetime of the bosons in such an orbital can be made long enough (~ 20 ms) by using double-well optical lattices, in order to establish coherence and perform measurements.

After this short overview, we see that the techniques to manipulate ultracold atoms in optical lattices have been amazingly improved over the last years. It is also remarkable that, today the physics of a few-body system can also be observed in the labs as reported by Jochim et al. [99]. The future is then very promising for the kind of setups that as those investigated in this work. Therefore, our system can be thought to be experimentally motivated, thus expecting future realizations of some of the predicted many-body effects that we will present throughout this work.

Many-Body Wannier-Stark System: Spectral Analysis

Among the many interesting systems that can be studied using ultracold atoms in optical lattice setups, one can find the Wannier-Stark problem (see sec. 2.2.1). The main goal of this chapter is to present a detailed study of the properties and emerging phenomena of this system, with special focus on the strongly interacting many-body regime. As mentioned in the previous chapter, the tilted single-band Bose-Hubbard model has been amply studied. In this, the onset of *quantum chaos* is achieved by applying an external Stark Force [19, 30, 43, 58, 59]. We now focus our efforts on an extended version of this problem: the two-band system. Special emphasis is put on the mechanisms to couple the Bloch bands, in order to make predictions on the diffusion, and relaxation dynamics towards equilibrium. Some of these effects can be steered by the important parameters as: the Stark force, interaction strength and potential depth.

We start our study with an characterization of the the many-body Wannier-Stark energy spectrum. It shall be shown that the transition between chaos and spectral regularity can determined by mainly three parameters: the filling factor of the optical lattice, the energy gap between the Bloch bands and the order of resonance Eq. (2.25). Aspects of integrability of our Hamiltonian system are crucial for expected predictions.

3.1 Our System

3.1.1 Two-Band Many-Body Wannier-Stark Hamiltonian (TBMWSH)

In section 2.2.1, we have shortly described our many-body system. We now explain the concepts that our study involves and what are precisely the questions we want to be answered. Our system consists of ultracold bosonic atoms in one-dimensional optical lattice, subjected to an additional Stark force F (see Fig. 3.1). By including such a external potential, we can stimulate the quantum transport of atoms along the lattice and at the same time, the force couples the lowest Bloch bands to the higher ones [9, 56, 59, 64, 66, 67, 75, 100]. The mechanism responsible for the latter transition is the well-known Landau-Zener tunneling phenomenon [65], which can also induce dissipation. It means reduction of the total particle number, of course, it depends on how system and enviroment get defined. In this chapter, we essentially study a closed system, for which the total particle number N is constant, hence a good quantum number.

In chapter 2 we have shown that the two-band Bose-Hubbard Hamiltonian reads

$$\hat{H} = \sum_{\beta=a,b} \hat{H}(\beta) + \hat{H}_1 + \hat{H}_2 + \hat{H}_D, \quad (3.1)$$

where every term defined as follows

$$\hat{H}(\beta) = \sum_{l=1}^L \left[-\frac{J_\beta}{2} (\hat{\beta}_{l+1}^\dagger \hat{\beta}_l + h.c.) + \frac{W_\beta}{2} \hat{n}_l^\beta (\hat{n}_l^\beta - 1) + 2\pi F l \hat{n}_l^\beta \right] \quad (3.2)$$

$$\hat{H}_1 = \sum_{l=1}^L \sum_{s=0}^{L-1} 2\pi F C_s (\hat{a}_{l+s}^\dagger \hat{b}_l + h.c.) \quad (3.3)$$

$$\hat{H}_2 = \sum_{l=1}^L \frac{W_x}{2} (\hat{b}_l^\dagger \hat{b}_l^\dagger \hat{a}_l \hat{a}_l + h.c.) \quad (3.4)$$

$$\hat{H}_D = \sum_{l=1}^L 2W_x \hat{n}_l^a \hat{n}_l^b + \Delta_g \hat{n}_l^b. \quad (3.5)$$

The bosonic annihilation (creation) operators are given by $\hat{\beta}_l$ ($\hat{\beta}_l^\dagger$), with $\beta = a$ for the lower and $\beta = b$ for the upper band. The number operators are $\hat{n}_l^\beta = \hat{\beta}_l^\dagger \hat{\beta}_l$. The dimension of the Hilbert space \mathcal{H} , expanded by the Fock states $|\vec{n}_{ab}\rangle \equiv |n_1^a, n_2^a, \dots, n_L^a\rangle \otimes |n_1^b, n_2^b, \dots, n_L^b\rangle$, is given by

$$\dim(\mathcal{H}) = \frac{(N + 2L - 1)!}{N!(2L - 1)!}, \quad (3.6)$$

where L is the number of lattice sites. Our Hamiltonian might be considered as two tilted single-band Bose-Hubbard Hamiltonians $\hat{H}(\beta = a)$ and $\hat{H}(\beta = b)$, whose coupling is set through the three following processes:

- (i) Interband one-particle exchange represented by \hat{H}_1 with transition strengths proportional to C_s . The integer $s = |l - l'|$ represents the dipole-induced tunneling between lattice sites l and l' (see Fig. 2.4). Note that the $s = 0$ is also included, which has the largest magnitude $|C_0|$. The ratios $|C_{s>0}/C_0|$ are usually smaller, because of the decreasing overlap between single-particle Wannier functions in different lattice sites. The coefficients $C_{s>0}$ drop faster to zero when increasing either V_0 or s_0 (see Table A.2). We therefore neglect transitions with $s > 2$ in most of the computed data.
- (ii) The term \hat{H}_2 introduces two-particle exchanges between the Bloch bands. This term is provided by the interparticle interaction with strength proportional to W_x .
- (iii) The Hamiltonian \hat{H}_D contains the energy separation (Δ_g) between the two Bose-Hubbard chains. Additionally, it introduces the repulsive interaction between particles occupying the same well different Bloch bands. Its energy cost is proportional to W_x and it lies on the diagonal of the Hamiltonian matrix.

We again highlight that, in the compared to previous studies of the system (see. [75, 81]), we have introduced two special modifications: first, a bichromatic potential is used for an easy control of the lattice parameters (see App. A.1 for details). Our main interest is to investigate the many-body effect induced by the variation of the energy gap Δ_g . Secondly, we consider at least

3. Many-Body Wannier-Stark System: Spectral Analysis

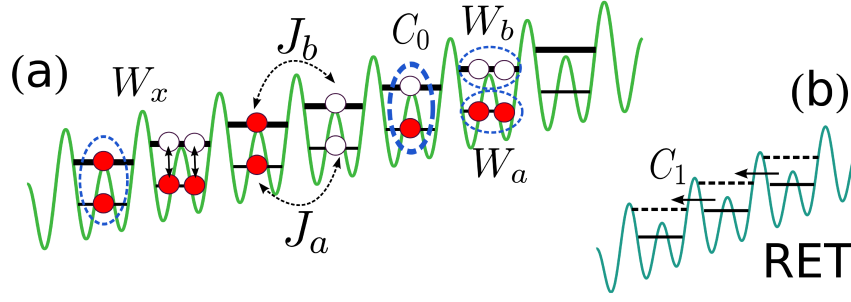


Figure 3.1: Many-Body processes of the two-band Bose-Hubbard Hamiltonian. (a) Bichromatic one-dimensional tilted optical lattice loaded with ultracold atoms. (b) Resonant enhanced tunneling (RET) condition for the nearest neighboring double wells, i.e., for a first order resonance with strength proportional to C_1 .

two extra dipole-induced tunneling terms represented by the term \hat{H}_1 . This two modifications shall help us to work with a well isolated and realistic physical system.

For the numerical implementations, as diagonalization and time evolution, it is convenient to work in the interaction picture. This is done by transforming the Hamiltonian with respect to the tilting term in \hat{H}_D as follows

$$\hat{H}' \rightarrow \exp\left(-i \sum_{l,\beta} 2\pi F l \hat{n}_l^\beta t\right) \hat{H} \exp\left(i \sum_{l,\beta} 2\pi F l \hat{n}_l^\beta t\right), \quad (3.7)$$

which removes the tilt $\sum_{l,\beta} 2\pi F l \hat{n}_l^\beta$ and transforms the hopping- and inter-band coupling terms into the time-dependent ones

$$\begin{aligned} \hat{\beta}_{l+1}^\dagger \hat{\beta}_l &\rightarrow \hat{\beta}_{l+1}^\dagger \hat{\beta}_l e^{-i\omega_B t} \\ \hat{a}_{l+s}^\dagger \hat{b}_l &\rightarrow \hat{a}_{l+s}^\dagger \hat{b}_l e^{-i\omega_B s t}, \end{aligned} \quad (3.8)$$

with $\omega_B \equiv 2\pi F$. The gauge-transformed Hamiltonian reads

$$\begin{aligned} \hat{H}'(t) &= \sum_{\beta=a,b} \sum_{l=1}^L -\frac{J_\beta}{2} \left(\hat{\beta}_{l+1}^\dagger \hat{\beta}_l e^{-i\omega_B t} + h.c. \right) + \sum_{s=0}^2 \omega_B C_s (\hat{a}_{l+s}^\dagger \hat{b}_l e^{-i\omega_B s t} + h.c.) \\ &+ \sum_{\beta=a,b} \sum_{l=1}^L \frac{W_\beta}{2} \hat{n}_l^\beta (\hat{n}_l^\beta - 1) + 2W_x \hat{n}_l^a \hat{n}_l^b + \Delta_g \hat{n}_l^b + \frac{W_x}{2} \left(\hat{b}_l^\dagger \hat{b}_l^\dagger \hat{a}_l \hat{a}_l + h.c. \right), \end{aligned} \quad (3.9)$$

and it is translationally invariant since there is no longer an explicit spatial dependence. We impose periodic boundary conditions by identifying $\hat{\beta}_{L+1}^\dagger = \hat{\beta}_1^\dagger$. The latter Hamiltonian commutes with the translation operator \hat{S} , therefore a suitable basis for numerical diagonalization and further spectral analysis is the translationally invariant Fock basis. The basis vectors are defined as

$$|s, \kappa_j\rangle = \frac{1}{\sqrt{M(s)}} \sum_{l=1}^{M(s)} e^{i2\pi\kappa_j l} \hat{S}^l |\vec{n}_{ab}\rangle, \quad (3.10)$$

with quasimomentum $\kappa_j = \frac{j}{M(s)}$, $j = 1, \dots, M(s)$, and $M(s)$ is the number of cyclic permutations of the fock state $|\vec{n}_{ab}\rangle = |n_1^a n_2^a \dots n_L^a\rangle \otimes |n_1^b n_2^b \dots n_L^b\rangle$ [59]. The dimension of the Hilbert space is then reduced to $\mathcal{N}_s \approx \dim(\mathcal{H})/L$, when working in a subspace with fixed quasimomentum κ .

In this work we restrict ourselves to the subspace with $\kappa = 0$, for which our Hamiltonian matrix is real and symmetric. This brings the advantage in the numerical calculation since there exists various sophisticated diagonalization methods as the lanczos algorithm (see App. B.2) that facilitate the analysis of the system under study. Nevertheless, some of our results can be extended to Hermitian Hamiltonian ($\kappa \neq 0$) since they do not depend explicitly on the basis as we shall see later. On the other hand, the gauge-transformed Hamiltonian is time-dependent and has a fundamental periodicity in time given by the Bloch period $T_B = 2\pi/\omega_B$. The remaining frequencies in (3.9) are multiples of ω_B ($\omega = s\omega_B$) and do not modify the periodicity of the Hamiltonian.

At this point, it is very helpful to implement the Floquet theory. This allows us to get rid off the time dependence and diagonalize the Floquet operator \hat{H}_f instead [101]

$$\hat{H}_f|\varepsilon_i\rangle = \varepsilon_i|\varepsilon_i\rangle, \quad \text{with } \hat{H}_f = \hat{H}(t) - i\partial_t. \quad (3.11)$$

We characterize the spectrum of energies $\{\varepsilon_i\}$, commonly called quasienergies, as a function of any control parameter of our system. The eigenenergies of the Floquet operator are obtained numerically by implementing a Lanczos diagonalization routine. The spectrum under study consists of those eigenenergies ε_i that lie within the so-called fundamental Floquet zone (FZ):

$$\varepsilon_i \in [\varepsilon_0 - \omega_B/2, \varepsilon_0 + \omega_B/2] \Leftrightarrow |\varepsilon_i - \varepsilon_0| \bmod \omega_B/2, \quad (3.12)$$

with ω_B the width of the FZ and ε_0 its predefined center. Throughout this work we conveniently set ε_0 as a function of F in order to enhance the performance of the algorithm and also to improve the visualization of the spectrum in different regions. The full Floquet spectrum can be reproduced by shifting the FZ, i.e. $\varepsilon_i \rightarrow \varepsilon_i + n_{fz}\omega_B$, with the index $n_{fz} \in \mathbb{Z}$ of the FZ. The latter is just another good quantum number introduced by the temporal periodicity. From (3.12) we see that the spectrum is periodic. It implies that, whenever a single eigenenergy reaches the boundary of the FZ, as any parameter is continuously changed, this energy will appear at the opposite boundary. This property makes it very difficult to follow an individual energy of the spectrum. The ordering of the quasienergy spectrum is not a simple task. However, we shall show that it is possible to avoid this problem and thus a spectral ordering becomes unnecessary for the analysis.

The procedure shortly described above is explained in detail in App. B. Furthermore, it is equivalent to diagonalize the evolution operator integrated over one Bloch period,

$$\hat{U}_{T_B} = \hat{\mathcal{T}} \exp \left[-i \int_0^{T_B} \hat{H}(t) dt \right] \quad (3.13)$$

where $\hat{\mathcal{T}}$ stands for the time ordering operator. The diagonalization of the Floquet operator (3.12) has advantages with respect to the computation times for larger systems and also allows a deep analysis of the energy spectrum, as will be shown starting in the next section.

3.2 Static Analysis of the TBMWSH

The many processes involved in our problem make it very difficult to find exact analytical solutions for eigenstates and eigenenergies. Nevertheless, we can study the system in the limit cases, where the system is expected to be nearly integrable or at least to have good quantum numbers. In fact, we shall see that in those regimes it is possible to extract useful energy scales that allows one to distinguish the onset of non-integrability and further quantum chaos [102].

3. Many-Body Wannier-Stark System: Spectral Analysis

To start with, we study the Floquet spectrum in two separate instances: first, with no interparticle interaction, sometimes referred to as the non-interacting case. Secondly, we turn on the interactions in order to describe the many-body effects. For some analytical calculations, we use the time-independent Hamiltonian, and the respective comparison is done with exact numerical calculation, based on the diagonalization of the Floquet Hamiltonian.

3.2.1 Non-interacting Many-Body Hamiltonian: The Manifold Approach

Let us then start with the non-trivial, non-interacting limit, which is described by the Hamiltonian Eq. (3.1) with $W_i = 0$. The respective Hamiltonian reads

$$\hat{H} = \sum_{\beta=a,b} \sum_{l=1}^L \left[-\frac{J_\beta}{2} (\hat{\beta}_{l+1}^\dagger \hat{\beta}_l + h.c.) + (\omega_B l + \Delta_\beta) \hat{n}_l^\beta \right] + \sum_{s=0}^{s=2} \sum_{l=1}^L \omega_B C_s (\hat{a}_{l+s}^\dagger \hat{b}_l + h.c.), \quad (3.14)$$

where the energy separation between the Bloch bands is $\Delta_{a,b} = \{0, \Delta_g\}$. As mentioned in the previous section, our Hamiltonian consists of two tilted Bose-Hubbard chains, whose energies are given by the Wannier-Stark ladder formula

$$\varepsilon_l^\beta = 2\pi l_\beta F + \Delta_\beta, \quad \text{with } l_\beta \in \mathbb{Z}. \quad (3.15)$$

These energies are obtained by diagonalizing the Hamiltonian of every chain in the coordinate space representation (see 2.2.1). Note that the energies in the latter equation can get degenerated at the positions $\varepsilon_l^b - \varepsilon_{l'}^a = (l - l') \cdot 2\pi F + \Delta_g = 0$, or equivalently $2\pi \cdot r \cdot F_r = \Delta_g$, with $r = l' - l$. The integer r represents the spatial separation between lattice sites l and l' , whose upper (lower) and lower (upper) single particle levels have the same energy at the tilt $F = F_r$. The two bands interact through the dipole terms $\hat{a}_{l+s}^\dagger \hat{b}_l$, and such a degeneracy is destroyed. Yet, instead of a crossing between the energies, an *Avoided Crossing* (AC) occurs. This is a well-known signature of interaction between the two chains, whose most interesting property is the induced transition between the Bloch bands, i.e. the resonances.

We want to study the mentioned resonances, leading to resonantly enhanced tunneling (RET). For that reason, it is possible to construct a local Hamiltonian by setting, for example, $l_a = 0$, which implies that $l_b = \pm r$. The sign depends on the direction of the tilt, thus in our case $F > 0$, the site $l_a = 0$ can be connected to the upperband lattice site $l_b = -r$. On the other hand, for $F < 0$ we have $l_b = +r$. We are interested in characteristic energy scales, therefore it turns out to be useful to rescale the Hamiltonian as $\hat{H} \rightarrow \hat{H}/\Delta_g$. The energy gap Δ_g is typically the largest parameter in our system. The ratios $|C_{s>0}|/\Delta_g$ are very small and we can treat the Hamiltonian perturbatively by neglecting $C_{s>0}$. The effective resonant Hamiltonian reads

$$\hat{H}_r = \sum_{\beta=a,b} \sum_{l=1}^L \left[-\frac{J_\beta}{2} (\hat{\beta}_{l+1}^\dagger \hat{\beta}_l + h.c.) + (\Delta_\beta - \omega_B r) \hat{n}_l^\beta \right] + \sum_{l=1}^L \omega_B C_0 (\hat{a}_l^\dagger \hat{b}_l + h.c.), \quad (3.16)$$

which is translationally invariant, and it can be diagonalized whether using the Fock or the seed basis. We highlight that the first two terms in the right-hand of this equation preserve the number of particle whether in the lower or in the upperband. Furthermore, in the flat lattice case $\omega_B = 0$, that is, without inter-band coupling, the eigenenergies of (3.35) can be classified by the number of particles in the upper band. After writing the Hamiltonian matrix in the Fock

(seed) basis, ordered by increasing upperband occupation number $M \equiv \sum_l \hat{n}_l^b$, the Hamiltonian is reduced to the block matrix

$$\hat{H}_r = \begin{pmatrix} \mathbf{H}_{0,0} & \mathbf{H}_{0,1}^\dagger & & & \\ \mathbf{H}_{0,1} & \mathbf{H}_{1,1} & \ddots & & \\ & \ddots & \ddots & \ddots & \\ & & & \mathbf{H}_{0,M-1}^\dagger & \\ & & & \mathbf{H}_{0,M-1} & \mathbf{H}_{M,M} \end{pmatrix}.$$

The $\text{diag}(\hat{H}_r) = \oplus_{M=0}^N (H_r)_M$ is a diagonal block matrix constructed by the Hamiltonian terms preserving the upperband occupation number M , that is the hopping and energy terms (see Fig. 3.2). The blocks on the diagonal are matrices with dimension

$$\begin{aligned} \text{for Fock states} & : d_M = \binom{M+L-1}{L-1} \binom{N-M+L-1}{L-1} \\ \text{for seed states} & : \tilde{d}_M \approx \frac{d_M}{L}. \end{aligned} \quad (3.17)$$

Motivated by the tight-binding-type form of the Hamiltonian matrix (3.2.1), we define:

Definition 1. Let \hat{P}_M be a projector onto the Hilbert subspace $\mathcal{H}_M \subset \mathcal{H}$ consisting of all states $|\phi\rangle$ whose upperband occupation number is M . The total number of these subspaces is $N+1$ (block matrices), and we will refer to the set of states $|\phi\rangle$ as the M -manifold with dimension d . In the particular case, when the set of states $|\phi\rangle$ maps one-to-one onto the members of a subspace of the Hilbert space expanded by Fock states, the dimension of the manifold is given by d_M , and the Hilbert space dimension is $\sum_M d_M$.

In this way, the Hamiltonian contains only coupling between those manifold states with excess of particles $\Delta M = \pm 1$, with "hopping" strength $\omega_B C_0$. We can construct a new Hamiltonian to describe the averaged one-particle exchange processes in our resonant system. To do this, we use the closure relation for the Fock basis given by

$$\sum_{i=1}^{\dim(\mathcal{H})} |\vec{n}_{ab}\rangle_{ii} \langle \vec{n}_{ab}| = \mathbf{1} \quad (3.18)$$

which can be rewritten as

$$\sum_{M=0}^N \hat{P}_M = \mathbf{1}, \quad \text{with} \quad \hat{P}_M = \sum_{i=1}^{d_M} |\vec{n}_{ab}; M\rangle_{ii} \langle \vec{n}_{ab}; M|. \quad (3.19)$$

Here $|\vec{n}_{ab}; M\rangle_i$ is a Fock state with M particles in the upperband. Using the projectors \hat{P}_M , one can rewrite the time-independent Schrödinger equation, $\hat{H}_r |\psi\rangle = E |\psi\rangle$, as

$$\sum_M \langle \psi_{M'} | \hat{H}_r | \psi_M \rangle = E \langle \psi | \psi_M \rangle \delta_{M,M'}, \quad \text{with} \quad |\psi_M\rangle = \hat{P}_M |\psi\rangle = \sum_i |\vec{n}_{ab}; M\rangle_{ii} \langle \vec{n}_{ab}; M | \psi \rangle, \quad (3.20)$$

and $\langle \psi_{M'} | \psi_M \rangle = \delta_{M,M'}$. The off-diagonal blocks are not necessary square matrices and they are computed from the single-particle exchange term

$$\hat{H}_{M,M'} \equiv \langle \psi_{M'} | \sum_{l=1}^L \omega_B C_0 \left(\hat{a}_l^\dagger \hat{b}_l + h.c. \right) | \psi_M \rangle. \quad (3.21)$$

3. Many-Body Wannier-Stark System: Spectral Analysis

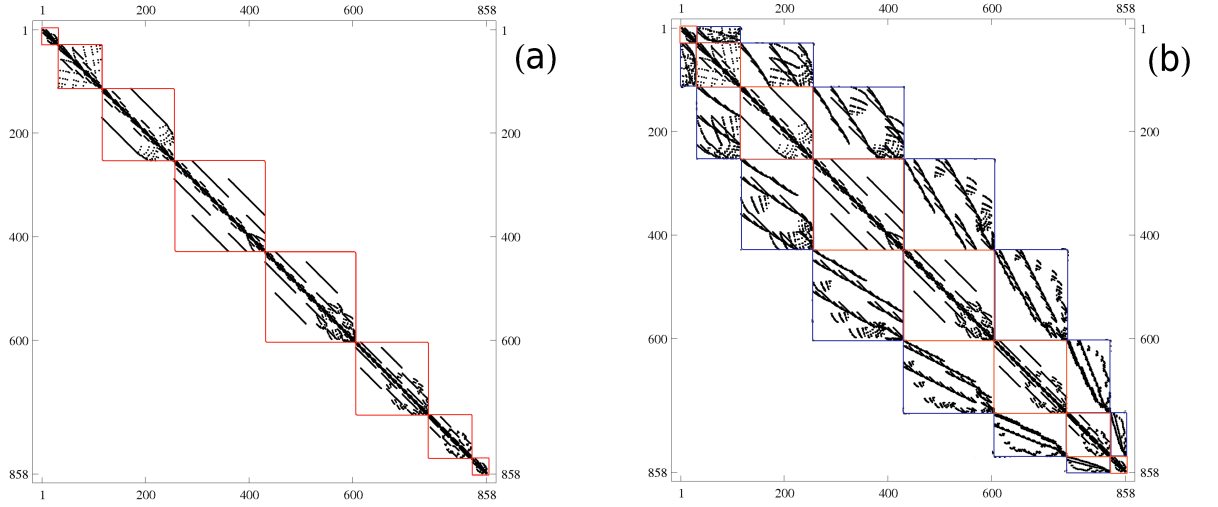


Figure 3.2: Hamiltonian matrix written in the seed basis subspace. (a) The figure shows the block structure of the Hamiltonian in the non-interacting case, for the system $N/L = 7/4$, with parameter $F_{r=1} = 0.09$, $s_0 = 3$ and $V_0 = 5$. Since $N = 7$ the matrix contains 8 blocks corresponding to the $N + 1$ manifolds. The intra-manifold off diagonal couplings are set by the hopping terms that do not couple Fock (seed) states with different manifold number. (b) Tight-binding-type many-body Hamiltonian matrix for the same parameter from panel (a). The remaining parameters are: $\Delta_g = 0.556$, $J_a = 0.059$, $J_b = -0.072$, $C_0 = -0.096$, $C_1 = 0.043$ and $C_2 = -0.0055$.

Let us for simplicity choose ${}_i \langle \vec{n}_{ab}; M | \psi \rangle = 1/\sqrt{d_M}$, i.e. we assume that the state $|\psi\rangle$ is homogeneously expanded in the subspace with manifold number M . This assumption yields to the tight-binding Hamiltonian for the manifolds, which reads

$$\hat{H}_r \simeq \sum_{M=0}^N \varepsilon_r(M) |\psi_M\rangle \langle \psi_M| + \omega_B C_0 \sum_{n=0}^N \sqrt{M+1} (|\psi_M\rangle \langle \psi_{M+1}| + h.c.), \quad (3.22)$$

where the energies on the diagonal are given by

$$\begin{aligned} \varepsilon_r(M) &= (\Delta_\beta - \omega_B r)M - J_a \langle \psi_M | \sum_l (\hat{a}_{l+1}^\dagger \hat{a}_l + h.c.) | \psi_M \rangle - J_b \langle \psi_M | \sum_l (\hat{b}_{l+1}^\dagger \hat{b}_l + h.c.) | \psi_M \rangle \\ &\simeq (\omega_B r + \Delta_g)M + (J_a - J_b)M. \end{aligned} \quad (3.23)$$

Here we used the relation $N = N_a + N_b$, with $M \equiv N_b$. Note that the latter Hamiltonian sums up all the contributions from the hopping terms and the dipole-type transitions, and the dimension of this is just $(N + 1)$. The first interesting energy scale is provided by the energy separation between contiguous manifolds (M and $M + 1$) in presence of one-particle exchange process. This can be estimated by the diagonalization of the two-state 2×2 Hamiltonian

$$H_{2 \times 2} = \begin{pmatrix} \varepsilon_r(M+1) & \omega_B C_0 \\ \omega_B C_0 & \varepsilon_r(M) \end{pmatrix}, \quad (3.24)$$

and therefore the inter-manifold energy difference Δ_r is given by the expression

$$\Delta_r = \Delta_g \sqrt{\left(1 - \frac{\omega_B r}{\Delta_g} + \frac{J_a - J_b}{\Delta_g}\right)^2 + 4 \left(\frac{\omega_B C_0}{\Delta_g}\right)^2}. \quad (3.25)$$

For typical parameters it holds $|J_a - J_b|/\Delta_g \ll 1$. The minimal width occurs at the exact resonance position $F_r \approx \Delta_g/2\pi r$ (apart from the extra corrections from Eq. (2.25)), therefore $\Delta_r(F_r) = 2\omega_B^r|C_0|$. We see that the inter-band coupling in the non-interacting regime yields to an avoided crossing of width $\Delta_r(F_r)$ around the resonance F_r . The eigenstates can be expressed as a linear combination of the manifold states $\{|\psi_M\rangle, |\psi_{M+1}\rangle\}$ as

$$|\phi^\pm\rangle = c_1|\psi_M\rangle \pm c_2|\psi_{M+1}\rangle. \quad (3.26)$$

At the exact resonance, we obtain $|c_1| = |c_2| = 1/\sqrt{2}$, i.e. the eigenstates $|\phi^\pm\rangle$ is perfect mixture of the manifold states, also called maximally hybridized states. These type of states $|\phi^\pm\rangle$ will be called *mixed states*. Here the concept of mixing might not be confused with the mixed states defined through the density operator which cannot be represented by a ket. We now study the mixing properties for the single particle case $N = 1$.

Single Particle Case

The number of M -manifolds is two, $M = \{0, 1\}$. In Fig. 3.3-(a), we show the numerically computed spectrum of the full Bose-Hubbard Hamiltonian in the single particle case with $N/L = 1/6$. The appearance of avoided crossings (black boxes) reveals the inter-band coupling, i.e. manifold mixing, as the Stark force F treated as a control parameter. The closer to resonance position F_r , the smaller the energy splitting Δ_r . This reaches its the minimal value $\Delta_r = 2\pi F|C_0|$ at $F = F_r$. We see that the inter-band coupling removes the degeneracy that appears in case $C_0 = 0$, and this effect manifests itself by the occurrence of an AC. The larger the inter-band coupling, the wider the AC. In terms of the M -manifolds, the eigenstates of $H_{2 \times 2}$ are given by

$$|\phi^\pm\rangle = \frac{1}{\sqrt{b^2 + (\lambda_+ - a)^2}}(b|\psi_M\rangle \pm (\lambda_+ - a)|\psi_{M+1}\rangle), \quad (3.27)$$

with $M = 0$, $a = \varepsilon_r(M+1)$, $b = \omega_B C_0$ and $2\lambda_\pm = \varepsilon_r(2M+1) \pm \Delta_r$. At $F = F_r$, these states are reduced to the maximally hybridized two-level state: $|\phi^\pm\rangle_r = (|\psi_M\rangle + |\psi_{M+1}\rangle)/\sqrt{2}$, for $|b| = |\lambda_+ - a|$. The manifold number of the states $|\phi^\pm\rangle_r$ is given by

$$\tilde{M}_\pm = {}_r\langle\phi^\pm|\sum_l n_l^b|\phi^\pm\rangle_r = \frac{1}{2}M + \frac{1}{2}(M+1) = M + \frac{1}{2}, \quad M + \frac{1}{2} \notin \mathbb{Z}^+, \quad (3.28)$$

where the M -character of the ϕ -states is totally lost and M is no longer a good quantum number. In general, the manifold number is given by the expression

$$\tilde{M}_\pm = \langle\phi^\pm|\sum_l n_l^b|\phi^\pm\rangle = \frac{b^2}{b^2 + (\lambda_+ - a)^2}(M) + \frac{(\lambda_+ - a)^2}{b^2 + (\lambda_+ - a)^2}(M+1). \quad (3.29)$$

We can define the manifold mixing degree as

$$\zeta = \frac{|b|}{|\lambda_+ - a|} = \frac{2y}{1 + \sqrt{1 + 4y^2}}, \quad \text{with } y = \frac{|b|}{|\varepsilon_r|} \quad (3.30)$$

with

$$\frac{|b|}{|\varepsilon_r|} = \frac{2\pi F_r}{\Delta_g} \frac{F|C_0|}{|F - F_r|} \approx \frac{1}{r} \frac{|C_0|}{|1 - F_r/F|}. \quad (3.31)$$

3. Many-Body Wannier-Stark System: Spectral Analysis

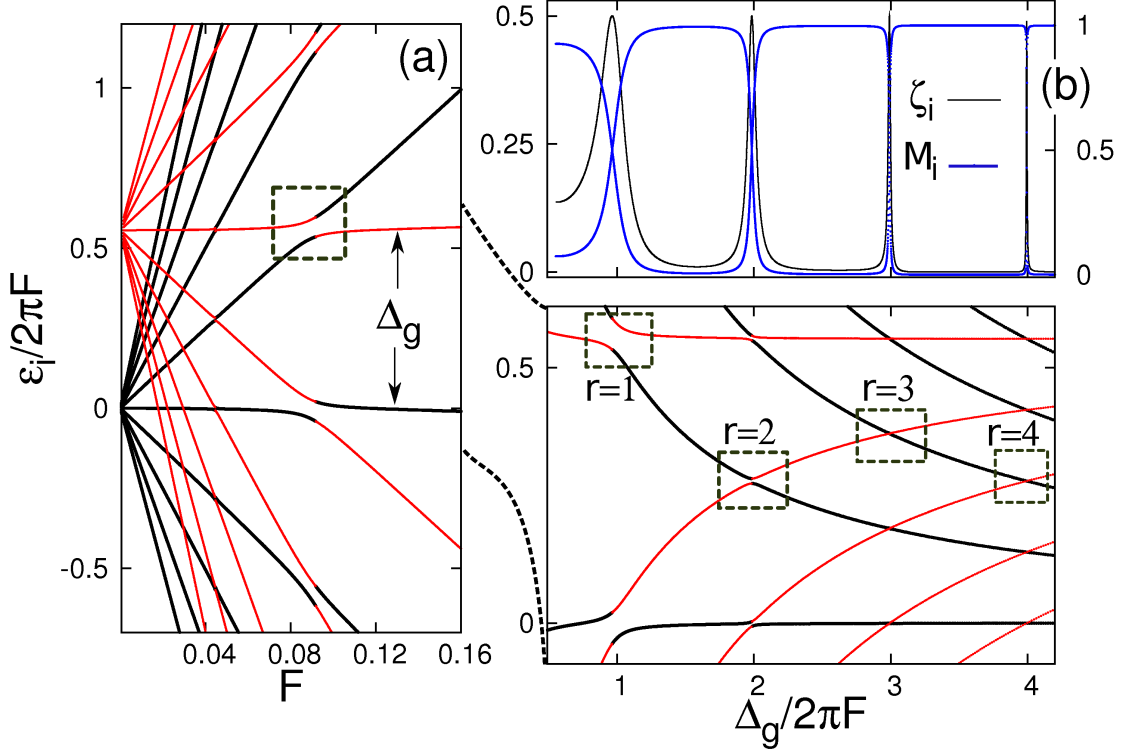


Figure 3.3: Numerically computed energy spectrum versus the Stark force in the single particle case, $N/L = 1/6$. (a) The two-band Wannier-Stark ladders can be recognized and the inter-band coupling manifest itself around the resonance position F_r through an avoided crossing. The different lines correspond to eigenstates of the type: $M = 0$ (black) and $M = 1$ (red). (b) Manifold mixing degree ζ_i and manifold numbers M_i for all Floquet eigenstates $|\varepsilon_i\rangle$. The parameters are the same as those in Fig. 3.2.

The manifold number can be rewritten as

$$\tilde{M}_{\pm} = M + \frac{\left(1 + \sqrt{1 + 4y^2}\right)^2}{4y^2 + \left(1 + \sqrt{1 + 4y^2}\right)^2}. \quad (3.32)$$

We have the following two limits:

- (i) Far enough from the resonance limits: (a) $F \gg F_r$, but $F < F_{r+1}$, the parameter $y \approx |C_0|/r$, where $|C_0| \lesssim 0.1$. This is usually the case for the typical Bose-Hubbard coefficients (see Table A.2). For resonance order $r > 2$, y is very small and therefore the manifold mixing degree $\zeta \rightarrow 0$. (b) For $F \ll F_r$, but $F > F_{r-1}$ and $y \approx |C_0|F/rF_r \ll 1$, it follows $\zeta \rightarrow 0$. In the latter regime one can increase the manifold mixing by decreasing the energy band to be comparable with the inter-band coupling strength $\omega_B|C_0|$. In this way the closeby resonances overlap. For $y \ll 1$, $\tilde{M}_{\pm} \approx M + 1$ which is an integer number. We conclude that far enough from the resonances F_r , the eigenstates $|\phi^{\pm}\rangle$ nearly belong to well defined manifolds: M and $M + 1$. Therein $|b|/|\lambda_+ - a| \ll 1$ and we can set a very accurate one-to-one mapping between the eigenstate of $H_{2 \times 2}$ and the manifold states, $|\phi^+\rangle \rightarrow |\psi_{M+1}\rangle$ and $|\phi^-\rangle \rightarrow |\psi_M\rangle$.
- (ii) Around the resonance, $F \rightarrow F_r$, the ratio $y \gg 1$ and $\tilde{M}_{\pm} \approx M + 1/2$. As seen before, this is the condition for maximal hybridization between the manifolds, and hence $\zeta \rightarrow 1$. This is represented by the black lines in Fig. 3.3-(b).

In the panel (a) of figure 3.3 we show the single particle spectrum for the two-band Wannier-Stark Hamiltonian. The black line corresponds to the ϕ -states with one particle in the lower band $|\psi_{M=0}\rangle \sim |100\dots; 000\dots\rangle$ and the red line to those states with one particle in the upper band $|\psi_{M=1}\rangle \sim |000\dots; 100\dots\rangle$. We set the color code by computing the manifold projections previously defined. A change of color occurs at the position of the resonant F_r . This implies that the lowest energy eigenstate changes its character when crossing the resonant regime, thus being transformed from $|\psi_{M=0}\rangle$ into $|\psi_{M=1}\rangle$. This effect is one of the most important characteristic of an AC. Along with the exchange of character, the manifolds get completely mixed at F_r , as shown by the black lines in the panel (b). There we plot the manifold mixing degree $\zeta_i = \zeta[|\varepsilon_i\rangle]$ and the manifold number $M_i = \langle \varepsilon_i | \sum_l \hat{n}_l^b | \varepsilon_i \rangle$ for all eigenstates of the Floquet operator $|\varepsilon_i\rangle$.

Case $N > 1$

For N non-interacting particles, any eigenstate $|\phi\rangle$ of the Hamiltonian H_r can be expanded in Fock (seed) states, hence also in manifold states, by using the projectors \hat{P}_M ; therefore the manifold number takes the form

$$\tilde{M}_\phi = \sum_{M=0}^N p_M M, \quad \text{with } p_M = \langle \phi | \hat{P}_M | \phi \rangle, \quad \text{and } \sum_{M=0}^N p_M = 1. \quad (3.33)$$

In analogy to the single particle case, the maximal hybridization should be obtained for $p_M = 1/(N+1)$ and $\tilde{M}_\phi = N/2$. Unfortunately this condition is not valid in general since for N even, any two manifolds can get equally populated since $\tilde{M}_\phi = N/2 \in \mathbb{Z}^+$. In this case, we can only say that such that two manifolds are completely mixed, but not the whole set of them. The reason lies on the fact that the single particle criterion, in the last section, sets the condition for mixing of contiguous manifolds.

A better measure of manifolds mixing is borrowed from Anderson localization theory. Owing to the tight-binding nature of the Hamiltonian H_r , a well-known localization measure is the *inverse participation ratio* [103]. This is defined by summing up the square of the probabilities p_M as

$$\xi_\phi = \sum_M p_M^2, \quad \Rightarrow \quad \zeta_\phi = 1 - \xi_\phi. \quad (3.34)$$

The inverse participation ratio ξ_ϕ is a useful way to quantify localization because it is easy to calculate (given that the probability distribution is known) and it behaves sensitively. That is, it has reasonable limits. If any state $|\phi\rangle$ is localized only one manifold, then $\xi_\phi = 1$. In contrast, if the state is evenly divided over $N+1$ manifolds with $p_M = 1/(N+1)$, then $\xi_\phi = 1/N$. Furthermore, this function decreases monotonically when probability is exchanged between two manifolds such that the distribution is more balanced, so it always falls between the limits of 1 and $1/N$.

As the number of particles is larger than one, Δ_r is still a characteristic energy scale for one-particle exchange processes. In figure 3.4, we show spectrum around the resonance $r = 1$ for the system $N/L = 5/3$, first rescaled by the width of the Floquet zone ω_B in the panel (a), which makes all the eigenenergies lie in the interval $[-1, 1]$, and second rescaled by Δ_r in the panel (b). We recognize the manifold formation before and after the resonant regime. These manifolds are characterized by bunches of levels closely degenerated and with the same manifold number M . At $F \approx F_r$ the manifold mixing appears and mostly all eigenstates belong to *mid-manifolds*, i.e. they are mixed states with $0 < M < N$. The manifold character is completely lost as shown in the

3. Many-Body Wannier-Stark System: Spectral Analysis

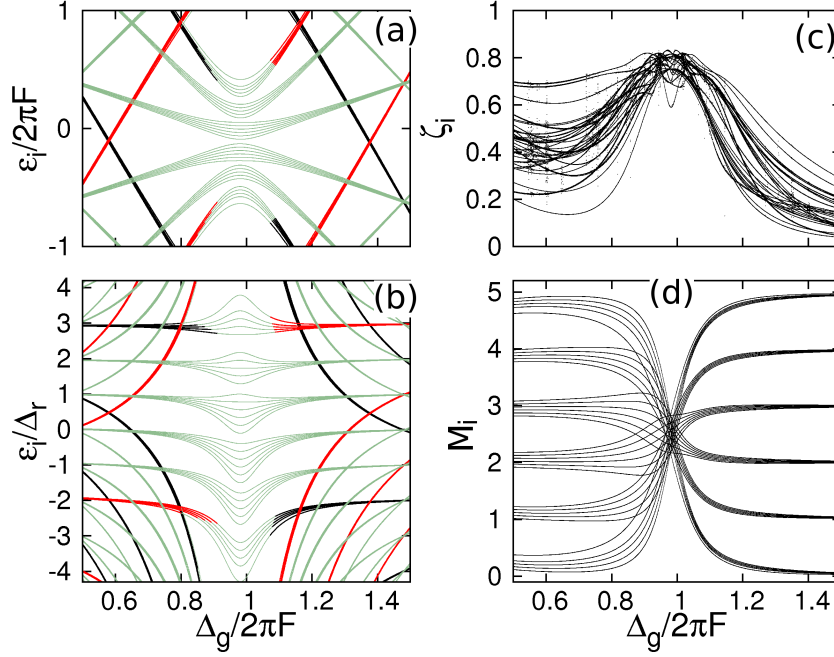


Figure 3.4: Spectrum for the non-interacting Hamiltonian around the resonant regime for $N/L = 5/3$. (a) Spectrum rescaled by the size of the Floquet zone $\omega_B = 2\pi F$. (b) Spectrum rescaled by the inter-manifold separation Δ_r . The panels (c) and (d) show the manifold mixing degree ζ_i and the manifold number M_i computed for all Floquet eigenstates as a function of the Stark force. The parameters are the same as those in Fig. 3.2.

panel (d) where mostly for all eigenstates $M \approx N/2$. Again, we must notice that by computing the manifold number is not enough to characterize the manifold mixing, since for N even the eigenstates may have $M = N/2$, which is an integer at the resonances. But there exists manifold mixing. That contradiction is washed-out by computing the manifold mixing degree ζ_i for all eigenstates, as shown in the panel (c).

Along with Δ_r , an additional energy scale appears only around $F \sim F_r$. At this position the hopping amplitudes J_β are energetically prohibited and therefore we neglect them. In addition, we must add the previously disregarded resonant term $C_{s=r}$, and thus the Hamiltonian reads

$$\hat{H}_r = \sum_{l=1}^L \omega_B C_0 (\hat{a}_l^\dagger \hat{b}_l + h.c.) + \sum_{l=1}^L \omega_B C_r (\hat{a}_{l+r}^\dagger \hat{b}_l + h.c.). \quad (3.35)$$

This is the Hamiltonian of a resonant three-level system that can be represented locally in space by the 3×3 matrix

$$H_{3 \times 3} = \begin{pmatrix} 0 & \omega_B C_0 & 0 \\ \omega_B C_0 & 0 & \omega_B C_r \\ 0 & \omega_B C_r & 0 \end{pmatrix}. \quad (3.36)$$

The new splitting is thus given by $\Delta_2 = 2\omega_B \sqrt{C_0^2 + C_r^2} > \Delta_r(F_r)$. Since the coefficients C_r drop to zero as r increases, the latter splitting becomes Δ_r . In Fig. 3.5 we show the time evolution of the upperband occupation number, which is defined by $M(t) = \langle \psi(t) | \sum_l \hat{n}_l^b | \psi(t) \rangle$. The initial evolved are of the kind $|\psi(0)\rangle = |111\dots\rangle_a \otimes |000\dots\rangle_b$. It is seen that the interplay between the two

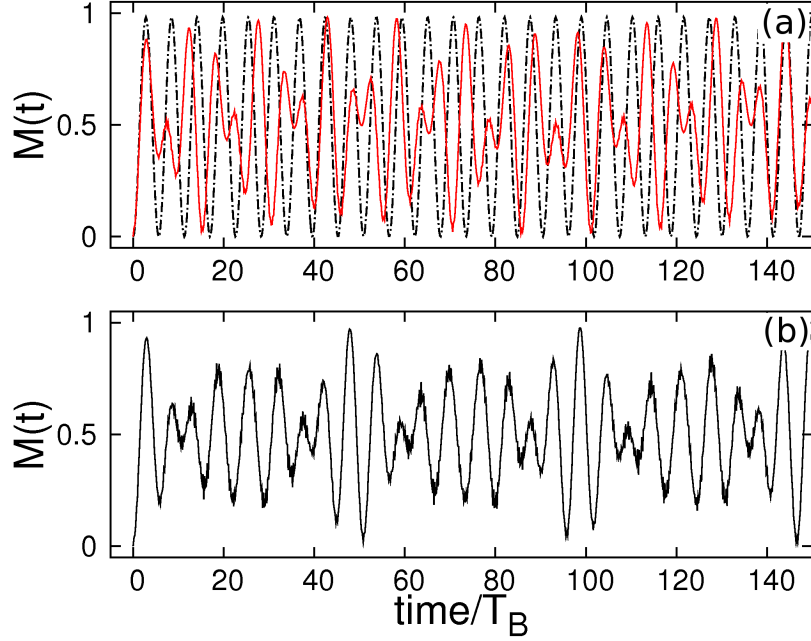


Figure 3.5: Time evolution of the upperband occupation number $M(t)$ at $F_{r=1} = 0.19$, $s_0 = 2$ and $V_0 = 5$. (a) the panel the Rabi-type oscillation (black-dashed line) for $M(t)$ in absence of the long-range dipole-induced terms ($C_{s>1} = 0$). The red line represents the evolution with $C_s \neq 0$. The system is defined by the filling factor $N/L = 4/4$. (b) $M(t)$ for the $N/L = 5/5$ and $C_{s>1} \neq 0$.

oscillator yields to smaller collapses and revivals of the signal in the course of the time. Here it is now clear the effect induced by the resonant coupling C_r , which plays an important role in the dynamics and must be always taken into account.

So far, we have obtained important information about our system, e.g. the characteristic inter-manifold splitting Δ_r as an important energy scale. Furthermore, we have introduced a natural way to interpret the Floquet spectrum in different regimes by mean of the manifold method. This approach turns out to be very useful to define observables that characterize inter-band mixing and the upperband occupation as well. In the next section we deal with the same problem but now the interparticle interaction will be taken into account. We shall show that it is still possible to characterize the system in terms of a few set of parameters.

3.2.2 Effects of the Interparticle Interaction

According to the last section, the energy separation between the manifolds $M = 0$ and $M = N$ is given by

$$\Delta E \approx N\Delta_g. \quad (3.37)$$

Yet, many other effects appear when turning the interparticle interaction, especially, in the resonant regime. Therein the manifold mixing degree is maximal. Let us first explain the changes introduced by the term \hat{H}_2 from Eq. (3.2). \hat{H}_2 induces inter-band coupling between the manifolds $|\psi_M\rangle$ and $|\psi_{M \pm 2}\rangle$. In this way, the Hamiltonian block-matrix \hat{H}_r has another diagonal, and the manifold tight-binding-type Hamiltonian is now extended to second neighboring transitions. Such a kind of Hamiltonians are usually non intergrable. The number of non-zero matrix elements in the new blocks depends on the strength W_x , which usually is small compared with the single-particle exchange transition strength $|C_0|$. In the case $N/L > 1$, the num-

3. Many-Body Wannier-Stark System: Spectral Analysis

ber of Fock (seed) states with double occupancy either in the lower or upperband increases, conversely to the case $N/L < 1$. This term can be considered as a residual effect. The remaining terms are the intra-band and inter-band on-site interparticle interactions, which lie on the diagonal of the block matrix (3.2.1). In particular, the term $W_x \sum_l \hat{n}_l^a \hat{n}_l^b$ induces strong intra- and inter-manifold splittings, whose effect is strongly enhanced in the mid-manifolds. All those terms together introduce many-level splittings and different energy scales. Degeneracies are removed and the appearance of a cluster of avoided crossings around F_r is expected, along with an enhancement of the manifold mixing. Hereafter, we refer to that cluster of avoided crossing as sea of ACs.

Despite the resulting complexity, we can still read out useful information from the spectrum. One way to proceed is by computing the commutator between the time-independent Hamiltonian (3.1) rescaled by the energy gap Δ_g and the manifold number operator $\hat{M} = \sum_l \hat{n}_l^b$. This reads

$$\frac{1}{\Delta_g} [\hat{H}, \hat{M}] = \frac{\omega_B}{\Delta_g} \sum_l \sum_s C_s (\hat{a}_{l+s}^\dagger \hat{b}_l - h.c.) - \frac{W_x}{2\Delta_g} \sum_l (\hat{b}_l^\dagger \hat{b}_l^\dagger \hat{a}_l \hat{a}_l - h.c.). \quad (3.38)$$

This expression allows us to set conditions for non-integrability and manifold mixing. We start with the easiest limit, i.e. when the gap is large enough, such that $W_x/2\Delta_g \ll 1$. That condition is always valid when $\Delta_g \gtrsim 1$. Under the last assumption and given $F \rightarrow 0$, the commutator (3.38) is negligible and the Hamiltonian get diagonalized in the Fock (seed) states basis, that is M is good quantum number. We also recognize that the labeling of the eigenstates can be done through the numbers

$$\nu_{\beta=a,b} = \frac{1}{2} \langle \psi_M | \sum_l \hat{n}_l^\beta (\hat{n}_l^\beta - 1) | \psi_M \rangle, \quad \nu_{ab} = 2 \langle \psi_M | \sum_l \hat{n}_l^a \hat{n}_l^b | \psi_M \rangle, \quad (3.39)$$

whose energy lies in the vicinity of $\varepsilon_r(M)$. These numbers are also integers. Therefore, the eigenenergies of the Hamiltonian are given by

$$\varepsilon(M; \nu_a, \nu_b, \nu_{ab}) = M\Delta_g + W_a \nu_a + W_b \nu_b + W_x \nu_{ab}, \quad (3.40)$$

and the states in the M th manifold can be written as $|M; \vec{\nu}_M\rangle \equiv |M; \nu_a, \nu_b, \nu_{ab}\rangle$. The eigenstates of \hat{H} can be written as a separable product of manifold states as

$$|\psi\rangle = |0; \vec{\nu}_0\rangle \otimes |1; \vec{\nu}_1\rangle \otimes \cdots \otimes |M; \vec{\nu}_M\rangle \otimes \cdots \otimes |N; \vec{\nu}_N\rangle. \quad (3.41)$$

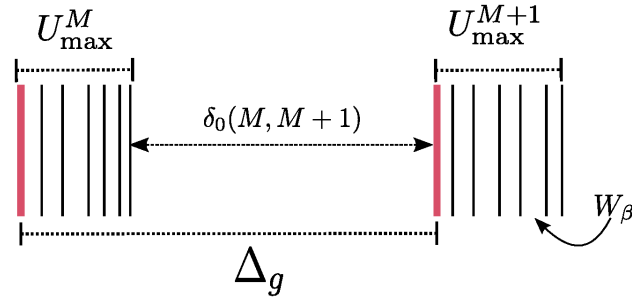


Figure 3.6: Energy scales of the interacting two-band Bose-Hubbard Hamiltonian. δ_0 represents the energy separation between contiguous manifolds. W_β represents the internal manifold splitting due to the different types of interparticle interactions in our model (see Eq. (3.40)).

It is worth to notice that now inside a single M -manifold block, there are many different off-diagonal non-zero entries due to the hopping terms. The new levels are provided by the splitting of the noninteracting eigenenergies, which makes the Hamiltonian matrix to be highly populated but banded as $|j - i| = 2d_{\lfloor M/2 \rfloor}$ (see Fig. 3.2).

Due to the on-site interparticle interaction, the maximal internal manifold splittings occur in those states with M particles sitting in the same lattice site whether in the upper- or lower band. Their values are given by

$$(U_a^M)_{\max} = \frac{W_a}{2}(N - M)(N - M - 1), \quad (3.42)$$

$$(U_b^M)_{\max} = \frac{W_b}{2}M(M - 1), \quad (3.43)$$

$$(U_{ab}^M)_{\max} = 2W_x(N - M)M, \quad (3.44)$$

where $(U_{ab}^M)_{\max}$ is different from zero only at a simultaneous occupation of M particles in the upperband and $N - M$ in the lower band, at the same lattice site. As mentioned before, this splitting gets larger in the middle of the spectrum and it becomes crucial for the understanding of local spectral correlations.

The energy scales are sketched in Fig. 3.6. We now define the maximal possible intra-manifold splitting as

$$U_{\max}^M = \max\{(U_a^M)_{\max}, (U_b^M)_{\max}, (U_{ab}^M)_{\max}\}. \quad (3.45)$$

Using U_{\max}^M , it is possible to redefine the size of energy interval ΔE (3.37). This is done by considering the maximal splitting of the highest manifold $M = N$, which occurs for those eigenstate(s), whose maximal projection in the Fock space is given by the Fock state with N particles in the same upperband level, say, the seed state

$$|N; \nu_a = 0, (\nu_b)_{\max}, \nu_{ab} = 0\rangle \sim \frac{1}{\sqrt{M^{(s)}}} \sum_{m=1}^{M^{(s)}} \hat{S}^m |000, \dots\rangle_a \otimes |N00, \dots\rangle_b. \quad (3.46)$$

We then have that maximal splitting generated by this kind of states is given by $U_{\max}^N = W_b N(N - 1)/2$. The minimal splitting U_0 corresponds to those states with the largest projection on the Fock states, with all particles uniformly distributed over the entire lattice, in the lower Bloch band. Its density is simply given by the filling factor N/L . We can recognize that the effective energy interval containing the whole set of \mathcal{N}_s eigenenergies is therefore given by the formula

$$\Delta E \approx N\Delta_g + \frac{1}{2}W_b N^2 - U_0, \quad (3.47)$$

which satisfies $\Delta E \leq \omega_B$ in the vicinity of the resonances. Far from the resonant regime, ΔE can be larger than the size of Floquet zone, which can be the case of time-independent Hamiltonian in Eq. (3.1). However, when we deal with the gauged-transformed Hamiltonian, the periodicity of the Floquet eigenenergies guarantees $\Delta E \leq \omega_B$, and the formula (3.47) is no longer valid. Yet, in order to estimate ΔE for any Floquet spectrum, we can use some properties of density of states (DOS) $\rho(\varepsilon)$: (i) the DOS is sensitive to level bunching; it means, if there exists a concentration of a large number of levels about a fixed energy, the DOS takes a Lorentzian-shaped with a very narrow width $\Delta\varepsilon$. In case of $\Delta\varepsilon \rightarrow 0$, and with a number of levels within this range larger than one, there exists degeneracies, hence a (quasi-)symmetry in the problem. The multiplicities given by the number of levels $N_\varepsilon (< \mathcal{N}_s)$ within $\Delta\varepsilon$. Two immediate examples are given

3. Many-Body Wannier-Stark System: Spectral Analysis

by inter-manifold levels when the interparticle interaction is weak (see Fig. 3.6) or with no one (see Fig. 3.4). (ii) The other is case of no degeneracies, i.e. whenever there is overlapping between different sets unperturbed energies is not negligible and the total number of states \mathcal{N}_s are spread all over within the energy interval ΔE . Its density is given by

$$\rho(\varepsilon) = \frac{\mathcal{N}_s}{\Delta E}, \quad (3.48)$$

where ΔE does not depend explicitly on the energy. The size of the energy interval depends on how the levels are distributed into the FZ, which can be quantified by the spectral second moment of the density of states $\int_{FZ} d\varepsilon \rho^2(\varepsilon) / \mathcal{N}_s^2$, whose inverse is just ΔE , i.e.

$$(\Delta E)^{-1} = \frac{1}{\mathcal{N}_s^2} \int_{FZ} d\varepsilon \rho^2(\varepsilon), \quad FZ: [-\omega_B/2, \omega_B/2]. \quad (3.49)$$

It is useful to define the filling of the Floquet zone

$$\chi^2 = \omega_B \int_{FZ} d\varepsilon \frac{1}{\mathcal{N}_s^2} \rho^2(\varepsilon), \implies \chi = \frac{\Delta E}{\omega_B}, \quad (3.50)$$

where the DOS in the case for a discrete spectrum is given by $\rho(\varepsilon) = \sum_i \delta(\varepsilon - \varepsilon_i)$. If the energy levels are uniformly distributed over the entire FZ, there exists at least one level per energy interval ω_B / \mathcal{N}_s , then

$$\rho(\varepsilon) \approx \frac{\mathcal{N}_s}{\omega_B} \implies \chi^2 \approx \omega_B \int_{FZ} d\varepsilon \frac{1}{\omega_B^2} \implies \chi \approx 1. \quad (3.51)$$

Otherwise, $\Delta E / \omega_B = 1 / \chi < 1$, since χ^2 diverges when the energies form bunches in different regions in the FZ.

As sketched in Fig 3.6, the energy gap between neighboring manifolds can be defined by $\delta_0(M) = \Delta_g - U_{\max}^M$. In the non-interacting regime we have proven that the manifold levels come close to each other in the RET regime. The minimal energy separation at the exact resonance is $\Delta_r(F_r) = 2\omega_B^r C_0$ (Eq. (3.25)). Here, since the interparticle interaction does not depend explicitly on the tilt, the reduced energy interval $\Delta E'$ is obtained by replacing $\Delta_g \rightarrow \Delta_r(F)$; this implies that the levels in the interval $[\varepsilon, \varepsilon + \Delta_r(F)]$ corresponding to the M th manifold go parallel to each other as a function of the force. As $F \rightarrow F_r$ the gap δ_0 decreases until it approaches its minimal value given by the mean level spacing

$$\delta(F) = \frac{\Delta E(F, r)}{\mathcal{N}_s} = \frac{N\Delta_r(F) + 0.5W_b N^2 - U_0}{\mathcal{N}_s}, \quad (3.52)$$

keeping in mind that \mathcal{N}_s is the dimension of the Hilbert space. By using the Stirling formula $\ln(m!) \approx m \ln(m) - m$ and the Eq. (3.6), we find that number of levels inside ΔE grows exponentially either with N or L , that is $\mathcal{N}_s \approx \frac{1}{L} 2^N (N/2)^{2L} = \frac{1}{L} (N/2)^{2L-N} N^N$, where we also used $(1 + x/m)^m \approx x^m$. The mean level spacing reads

$$\delta_r(F) = \Delta E(F, r) \cdot \left(\frac{N}{2}\right)^{N-2L} N^{-N} L, \quad (3.53)$$

and the density of states

$$\rho_r(F) = \frac{1}{\delta_r(F)} = \frac{1}{\Delta E(F, r) L} \left(\frac{N}{2}\right)^{2L-N} N^N. \quad (3.54)$$

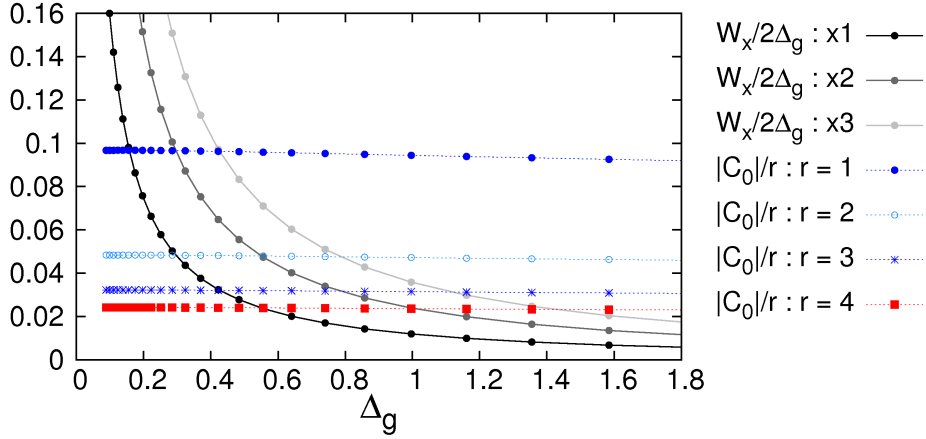


Figure 3.7: Ratios $\frac{|C_0|}{r}$ ($r = 1, 2, 3$ and 4) and $\frac{W_x}{2\Delta_g}$ as a function of the energy gap Δ_g .

Note that the number of states within ΔE grows faster with $N/L > 1$ than with $N/L < 1$, therefore the manifolds mix faster with $N/L > 1$ when crossing any order of resonance. In that case, the level repulsion creates the sea of ACs within an interval ΔF in the vicinity of F_r . Conversely, for $N/L < 1$ the level repulsion is weak and the levels tend to remain parallel to each other right before and after the resonant regime. The width of the ACs are very small within the interval $\Delta\tilde{F} < \Delta F$. For a filling factor $N/L = 1$, the dimension of the Hilbert space is $\mathcal{N}_s \approx N^{N+1}$. In analogy with the N -qubit system reported in [104], the system may be considered to have an effective spin $S = N/2$ with projections

$$m = \frac{1}{2}(N_b - N_a) = -\frac{N}{2}, -\frac{N-1}{2}, \dots, \frac{N-1}{2}, \frac{N}{2}, \quad (3.55)$$

where the interqubit interaction is in our case the Stark force and the Hamiltonian can effectively be treated as a one-dimensional quantum Ising Hamiltonian.

Into the Resonant Regime

In the resonant regime we have: $\omega_B |\sum_s C_s| / \Delta_g \approx |\sum_s C_s| / r \approx |C_0| / r$. That is, the larger the order of the resonance, the smaller the manifold mixing and the commutator (3.38) drops to zero for Δ_g large enough. Therefore, the manifold number M is still a good quantum number. Such a property is destroyed as Δ_g decreases and thus the effect of the two-particle exchange becomes important. In figure 3.7 we show the ratios $|C_0|/r$ and $W_x/2\Delta_g$ as a function of the energy gap Δ_g . Note that the mixing is expected to be overwhelmingly strong around the first order resonance when the following condition is reached

$$|C_0| \approx \frac{W_x}{2\Delta_g} \approx 0.1. \quad (3.56)$$

Of course, to fulfil Eq. (3.56), the energy gap Δ_g must be very small. From the experimental point of view, that condition can be induced for non necessarily smaller gaps, by increasing the interparticle interaction. For example, by driving the system close to a Feshbach resonance [7]. Another way is to increase the number of particles in the system with L fixed, since the mean level spacing decreases exponentially with N ; then strong band mixing may occur for $\Delta_g \gtrsim 0.5$ with $W_{a,b,x} \rightarrow 2(3) \times W_{a,b,x}$.

3. Many-Body Wannier-Stark System: Spectral Analysis

We illustrate the differences in the spectral properties when considering $N/L > 1$, $N/L < 1$ and $N/L = 1$ in Figs. 3.8 and 3.9. There we plot the manifold number $\{M_i, \zeta_i\}$ for all eigenstates as a function of the ratio $\mu = \Delta_g/2\pi F$, for different filling factors and decreasing Δ_g (from (a) to (c)). Notice that the resonance positions still remain close to interger values of μ . In the figure 3.8, we see clearly the manifold formation for larger gaps and their respective destruction when crossing the resonances or likewise when $W_x/2\Delta_g$ increases. Note that in the panels of the column (c), the manifolds only manifest themselves for smaller filling factors even if Δ_g is small and these practically disappear over the entire spectrum for filling factors larger than one. This is a signature of a fully mixed spectrum, and neither M_i , ν_β nor ν_{ab} are good quantum numbers of the Hamiltonian (3.1).

The values of the tilt at which two contiguous manifolds start overlapping can be estimated using the inter-manifold gaps δ_0 (see Fig. 3.6). For instance, between the manifolds $M = 0$ and $M = 1$ we have

$$\begin{aligned} \delta_0[|0\rangle \rightarrow |1\rangle] &= \Delta_r - U_{\max}^0 \\ &= \Delta_g \sqrt{\left(1 - \frac{F}{F_r}\right)^2 + 4\left(\frac{\omega_B C_0}{\Delta_g}\right)^2} - \frac{W_a}{2} N(N-1). \end{aligned} \quad (3.57)$$

Then, when $\delta_0 \rightarrow 0$ the mixing starts, whether from the left ($F < F_r$) or from the right ($F > F_r$), the position can be found by solving the second order equation

$$\left(\left(1 + \frac{2C_0}{\mu_r}\right)^2\right)\theta^2 - 2\theta + 1 - \tilde{U}^2 = 0, \quad (3.58)$$

with

$$\theta = \frac{\mu_r}{\mu}, \quad \tilde{U} = \frac{W_a}{2\Delta_g} N(N-1), \quad \mu = \frac{\Delta_g}{2\pi F} \quad \text{and} \quad \mu_r = \mu(F_r). \quad (3.59)$$

The solutions are given by the inverse tilts

$$\mu^+ = \frac{1}{1 + \alpha_r} \mu_r = (1 + \alpha_r + \alpha_r^2 + \alpha_r^3 + \dots) \mu_r, \quad (3.60)$$

$$\mu^- = \frac{1}{1 - \alpha_r} \mu_r = (1 - \alpha_r + \alpha_r^2 - \alpha_r^3 + \dots) \mu_r, \quad (3.61)$$

for $\alpha_r < 1$ and we can define effectively the width of the resonance $\Delta F = |F_+ - F_-| \approx 2\alpha_r F_r$, with

$$\alpha_r = \sqrt{1 - (1 - \tilde{U}^2) \left(1 + \left(\frac{2C_0}{\mu_r}\right)^2\right)}, \quad \text{if: } (1 - \tilde{U}^2) \left(1 + \left(\frac{2C_0}{\mu_r}\right)^2\right) < 1. \quad (3.62)$$

The range ΔF that contains the sea of ACs grows with the parameter α_r . For instance, as $\alpha_r \rightarrow 1$, which happens when Δ_g decreases, neighboring resonances overlap each other since $\mu_+ \rightarrow 2\mu_r = \mu_{r+1}$, or equivalently $\Delta_g \approx W_a N(N-1)$. Therefore, the energy spectrum becomes more and more mixed for any Stark force F . Furthermore, the parameter α_r depends sensitively on the ratio between the interparticle interaction and the gap, which means that we can engineer our system in order to enhance or reduce the manifold mixing, at will (see Fig. 3.8). In general, the starting tilt for mixing can be defined as the average tilt of the set $\{F_M^\pm\}$, which is a better estimation since the manifolds with $0 < M < N$ start mixing way before and after F_r .

It is also observed that close to the full manifold mixing condition, the lowest and highest manifold are almost unoccupied, because of the large state population of the manifolds with

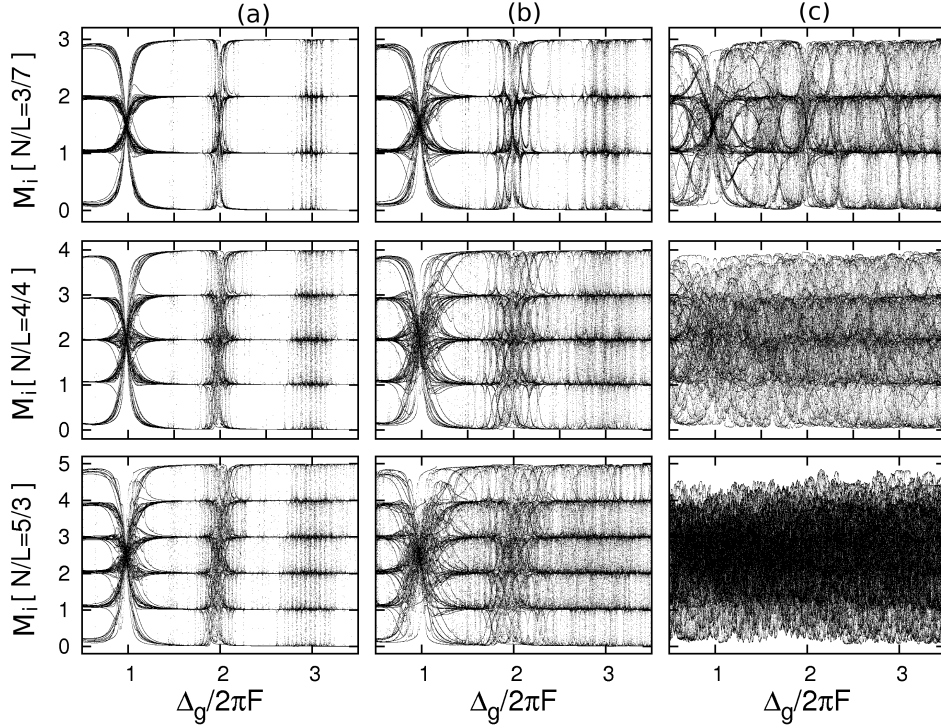


Figure 3.8: Manifold numbers $\{M_i\}$ as function of the ratio $\mu = \Delta_g/\omega_B$. The filling factors are $N/L = 3/7, 4/4$ and $5/3$ and the energy gap Δ_g corresponding to $V_0 = 5$. The panels in the column (a) show the results $W_x/2\Delta_g = 0.01$ with $s_0 = 2$. In the column (b) for parameters $W_x/2\Delta_g = 0.023$ with $s_0 = 3$ and (c) for $W_x/2\Delta_g = 0.097$ with $s_0 = 5$.

$0 < M < N$. The number of accesible states can be very large but not excess \mathcal{N}_s . In fact, for N odd there exists two contiguous central manifolds with the same size (see Fig. 3.2) with manifold numbers

$$M = \left\lfloor \frac{N}{2} \right\rfloor \quad \text{and} \quad M = \left\lfloor \frac{N}{2} \right\rfloor + 1, \quad (3.63)$$

and for N even there is only one with $M = N/2$. In the first case it is expected high degree of mixing and the properties of the sea of ACs to be slightly different in comparison with the second case. We can claim that for $W_x/2\Delta_g \sim 0.1$, the eigenstates living in the manifolds $M = \{0, N\}$ are weakly coupled to the remaining. The Hilbert space may be thus effectively reduced to a subspace expanded by the states with $0 < M < N$; this means, there are always particles in both Bloch bands with mean upperband occupation $M \approx N/2$. We will referred to this effect as: *manifold balance*, which is expected when the system relaxes to its minimal energy state in presence of inter-band coupling, i.e. it reaches the equilibrium (see the sketch in Fig. 3.10). This prediction will be confirmed in the time-domain, where we can study the relaxation properties of non-equilibrium initial state lying in any M -manifold. We expect high sensitivity on the spectral properties described up until now, especially for those initial state from mid-manifolds $M = \lfloor N/2 \rfloor$.

So far we have studied the properties of the spectrum, e.g. energy scales and some characteristics of the eigenstates (manifold number M_i and degree of manifold mixing ζ_i) in the different regimes defined by the Stark force, i.e. the off resonant and resonant regime characterized by tilts in the vicinity of F_r . Secondly, the non-interacting ($W_i = 0$) and the respective interact-

3. Many-Body Wannier-Stark System: Spectral Analysis

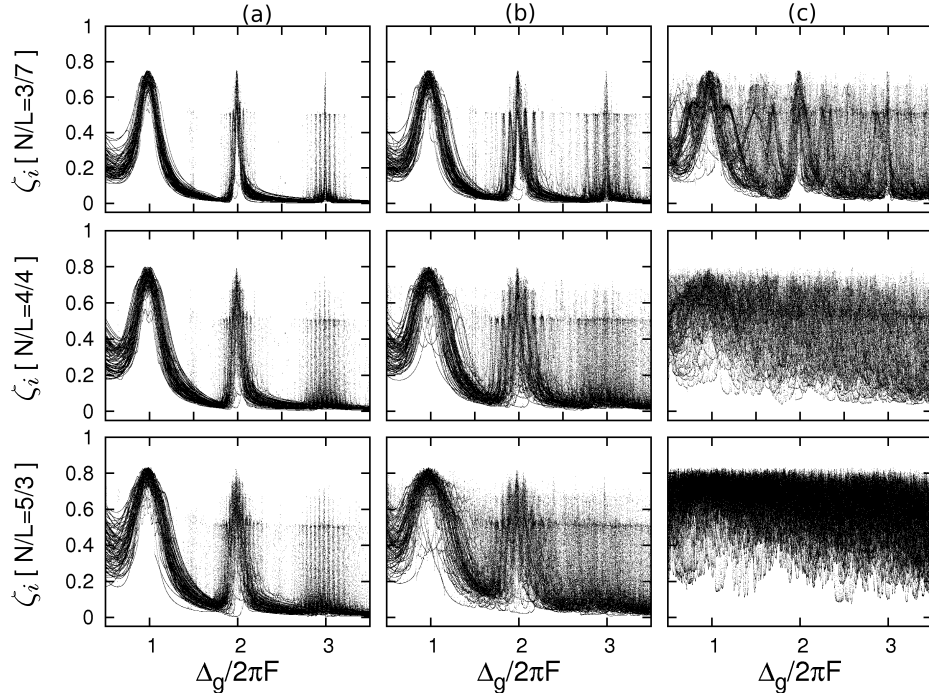


Figure 3.9: Manifold mixing degrees $\{\zeta_i\}$ as function of the ratio $\mu = \Delta_g/\omega_B$. The filling factors are $N/L = 3/7, 4/4$ and $5/3$ and the energy gap Δ_g corresponding to $V_0 = 5$. The panels in the column (a) show the results $W_x/2\Delta_g = 0.01$ with $s_0 = 2$. In the column (b) for parameters $W_x/2\Delta_g = 0.023$ with $s_0 = 3$ and (c) for $W_x/2\Delta_g = 0.097$ with $s_0 = 5$.

ing regime, which can be described by the manifold approach. We also defined useful measures that allow a better understanding of the spectral characteristics of the system, especially when and why the sea of ACs appears.

In the following, we will further characterize ACs clustering. To do this, we first have to detect the position where the single ACs occur as a function of the force and its respective width. In most of the proposed methods the idea is to follow the trajectory $\varepsilon_i(F)$ of a single eigenstate as a function of a tuning parameter, what requires an ordering of the energy spectrum. That procedure, in case of Floquet eigenenergies, is not straight forward due to its periodicity. Here, we present an alternative method based on the concept of probability vectors, which does not rely on ordering and brings additional advantages, directly connected with the properties of our system.

ACs Detection: Projector Approach

In quantum mechanics, the time evolution of an initial condition $|\psi(0)\rangle$ is obtained by applying the evolution operator \hat{U}_t as follows

$$|\psi(t)\rangle = \hat{U}_t|\psi(0)\rangle = \sum_j c_{j,0} e^{-i\varepsilon_j t} |\varepsilon_j\rangle, \quad \text{with } c_{j,0} = \langle \varepsilon_j | \psi(0) \rangle. \quad (3.64)$$

If the Hamiltonian \hat{H} has a free parameter λ , the energy spectrum ε_i depends on this parameter. Assuming no degeneracies as changing λ , two neighboring eigenenergies come close to each other for certain values λ_i . Due to the repulsion between them an avoided crossing appears,

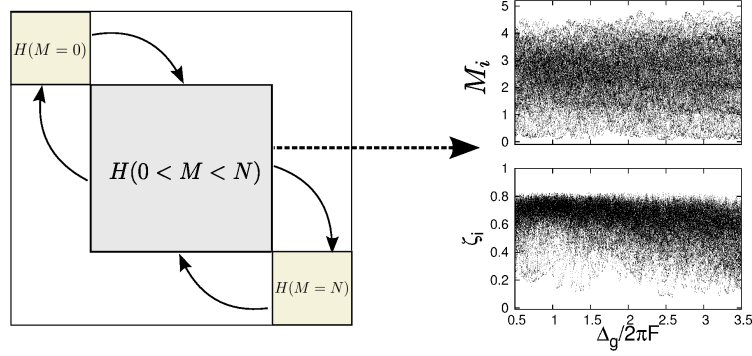


Figure 3.10: Manifold mixing process. This mostly appearing at the center of the spectrum by heavily coupling between manifolds with $0 < M < N$. The figures in the right panel are the same as in Fig. 3.8 and 3.9 for the system $N/L = 5/3$, $V_0 = 5$, $s_0 = 3$ and $\Delta_g = 0.16$.

with width δ_c .¹ The coupling strength between these states is thus given by $\delta_c/2$. At the values λ_i , the eigenstates hybridize and we can find locally in the spectrum the state

$$|\theta\rangle = a_1|\varepsilon_1\rangle + a_2|\varepsilon_2\rangle, \text{ with } |a_1| = |a_2| = \frac{1}{\sqrt{2}}. \quad (3.65)$$

Therefore, the time evolution of $|\psi(0)\rangle = |\theta\rangle$ is constrained to these local eigenstates and $c_{j,0} = \langle\theta|\varepsilon_j\rangle = 1/\sqrt{2}$, with $j = 1, 2$. Far away from the AC position $c_{1,0} \gg c_{2,0}$, then the system lives either in $|\varepsilon_1\rangle$ or $|\varepsilon_2\rangle$ and no dynamical transitions will occur. We see that only by following the absolute square of the projections $c_{j,0}$, the AC can be detected at the positions λ_i . If we now consider the expansion of the eigenstates in the original basis $|\varepsilon_j\rangle = \sum_{\alpha} A_{\alpha}|\alpha\rangle$. By choosing the initial condition to be one of the states $|\alpha\rangle$, then at λ_c the coefficients $|c_{j,0}|^2 = |\langle\alpha|\varepsilon_j\rangle|^2$ are only equal if the character of the local eigenstates is nearly the same and the hybridization is reached, i.e.

$$|\alpha\rangle = \frac{1}{\sqrt{2}}(|\varepsilon_1\rangle + |\varepsilon_2\rangle), \quad (3.66)$$

This is equivalently written as

$$|\langle\alpha|\varepsilon_1\rangle|^2 = |\langle\alpha|\varepsilon_2\rangle|^2 \text{ and } |\langle\alpha|\varepsilon_j\rangle|^2 = \langle\varepsilon_j|(|\alpha\rangle\langle\alpha|)|\varepsilon_j\rangle = \langle\varepsilon_j|\hat{P}_{\alpha}|\varepsilon_j\rangle. \quad (3.67)$$

The latter shows that, when detecting ACs we only have to use the projector that represents an initial state $\hat{P}_{\alpha} = |\alpha\rangle\langle\alpha|$, and compare the probabilities as the parameter λ changes. This does not require ordering of the eigenstates.

Let us now generalize the method. Consider the seed states projectors defined by

$$\hat{P}_{\alpha} = |s_{\alpha}, \kappa_j\rangle\langle s_{\alpha}, \kappa_j|, \text{ with } \sum_{\alpha} \hat{P}_{\alpha} = \hat{\mathbf{1}}. \quad (3.68)$$

In the following, we use the short notation $|s_{\alpha}\rangle \equiv |s_{\alpha}, \kappa_j\rangle$. The eigenstates of the Floquet operator can be expanded in this basis using the normalization condition in Eq. (3.68), and it looks like

$$\begin{pmatrix} \vdots \\ |\varepsilon_j\rangle \\ \vdots \end{pmatrix} = \begin{pmatrix} \langle s_1|\varepsilon_1\rangle & \langle s_2|\varepsilon_1\rangle & \dots \\ \langle s_1|\varepsilon_2\rangle & \langle s_2|\varepsilon_2\rangle & \dots \\ \vdots & \vdots & \ddots \end{pmatrix} \begin{pmatrix} \vdots \\ |s_i\rangle \\ \vdots \end{pmatrix},$$

¹Two eigenenergies will repel in case of no symmetries additional in the system, whenever they get close to each other as certain parameter is changed. See discussion of the single particle case in sec. 3.2.1

3. Many-Body Wannier-Stark System: Spectral Analysis

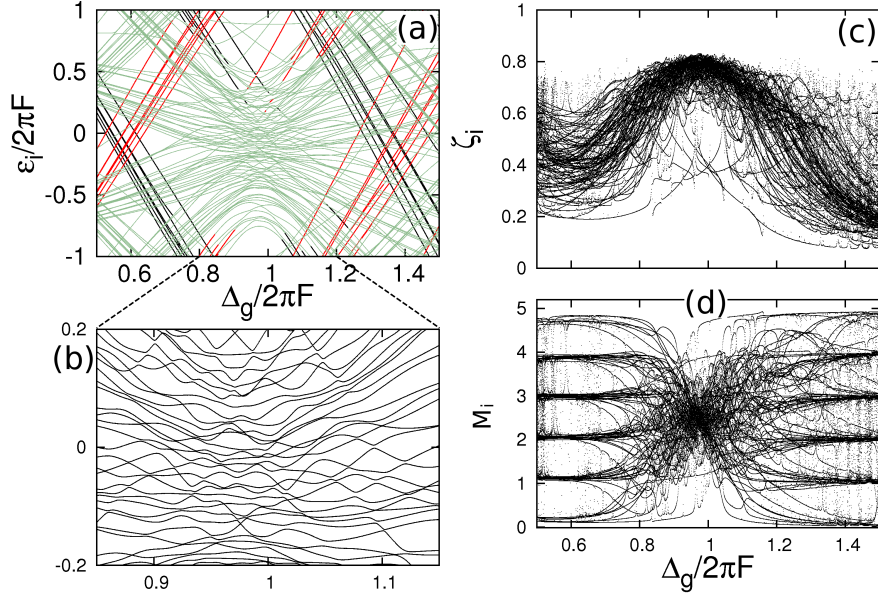


Figure 3.11: (a) Eigenenergy spectrum for the system $N/L = 5/3$, with $V_0 = 5$ and $s_0 = 3$ around the first order resonance. The black dots represent the energy state living in the manifold $M = 0$, the red ones the corresponding states from the manifold $M = N$ and the green dots correspond to mixed states with $0 < M < N$. (b) Zoom of the spectrum around the resonance position that evidences the sea of ACs predicted by the manifold mixing. The panels (c) and (d) show the individual manifold mixing degree ζ_i and the manifold number M_i for the eigenstates around the resonance.

where the matrix of probability amplitudes $(\mathbf{M})_{ij} = \langle s_i | \varepsilon_j \rangle$ is unitary. By following the discussion above, it is useful to define the vector of probabilities

$$\vec{\sigma}^{(\alpha)} = \begin{pmatrix} \vdots \\ |\langle s_\alpha | \varepsilon_j \rangle|^2 \\ \vdots \end{pmatrix}, \text{ with } \vec{\sigma}^{(\alpha)} = \vec{\sigma}^{(\alpha)}(\lambda).$$

We now set $\lambda = F$, and look for the positions in the energy spectrum where the local exchange of character between neighboring eigenstates $|\varepsilon_n\rangle \leftrightarrow |\varepsilon_{n\pm 1}\rangle$ will take place. To do this, we only need the information extracted from the diagonalization procedure and not from the dynamics, since we are only interested in the coefficients constructed from the initial state $c_{j,0}$ in Eq. (3.64). The components of the vector $\vec{\sigma}^{(i)}$ start changing in the vicinity of the AC and thus the largest one jumps between contiguous components rightafter the avoided crossing as shown for the single particle spectrum in Fig. 3.3. For not very sharp ACs, this component permutation is smooth function of F . To quantify the changes of the vector $\vec{\sigma}^{(i)}$ we can use the fidelity defined in ref. [30]

$$f_{\text{id}}(F, \delta F) \equiv |\langle \varepsilon_i(F) | \varepsilon_i(F + \delta F) \rangle|. \quad (3.69)$$

This is a very efficient way to detect avoided crossings as shown by the authors (see also App. D). We can redefine the latter equation for fidelity by using the projector \hat{P}_α and the closure relation

of the seed basis, $\sum_{\alpha} \hat{P}_{\alpha} = \mathbf{1}$. we thus obtain

$$\begin{aligned} G^{(\alpha)}(F, \delta F) &= \sum_{j=1}^{\mathcal{N}_s} |\langle \varepsilon_j(F) | \hat{P}_{\alpha} | \varepsilon_j(F + dF) \rangle|^2 \\ &= \sum_{j=1}^{\mathcal{N}_s} |\langle s_{\alpha} | \varepsilon_j(F) \rangle|^2 |\langle s_{\alpha} | \varepsilon_j(F + dF) \rangle|^2 \end{aligned} \quad (3.70)$$

which reduces the problem to the calculation of the fidelity of the probability vector $\vec{\sigma}^{(\alpha)}$. Let us define $f_{\alpha,j}(F) \equiv |\langle s_{\alpha} | \varepsilon_j(F) \rangle|^2$, and use the Taylor expansion up to the first order as

$$f_{\alpha,j}(F + \delta F) \simeq f_{\alpha,j}(F) + \delta F \frac{\partial}{\partial F} f_{\alpha,j}(F) + O(\delta F^{(n \geq 2)}). \quad (3.71)$$

We can rewrite the Eq. (3.70) as

$$G^{(\alpha)}(F, \delta F) = \sum_i f_{\alpha,j}^2(F) + \frac{\delta F}{2} \frac{\partial}{\partial F} f_{\alpha,j}^2(F), \quad (3.72)$$

where we can immediately recognize that the first term is nothing else than the inverse participation ratio

$$\xi_{\alpha}(F) = \sum_j |\langle s_{\alpha} | \varepsilon_j(F) \rangle|^4, \quad (3.73)$$

and the second its derivative. Numerically by considering a very fine step δF the second term can be neglected, and thus the fidelity of the vector $\vec{\sigma}^{(\alpha)}$ is reduced to calculate ξ_{α} , i.e.

$$\lim_{\delta F \rightarrow 0} G^{(\alpha)}(F, \delta F) = \xi_{\alpha}(F), \quad (3.74)$$

which has minima at the AC positions, i.e. $\partial \xi_{\alpha} / \partial F = 0$. Then we see that before and after the AC, the state represented by \hat{P}_{α} is recovered, but the maxima permutes along of the vector $\vec{\sigma}^{(\alpha)}$, i. e. from $j = k$ to $j = k \pm 1$. Due to the many different processes, not only one state participates in the AC event, but two, three or more eigenstates. This happens for example when three states are nearly resonant and there is coupling between pairs of states, for instance, in a resonantly three level system of the section 3.2. In our case, we have many different energy scales, and hence it is not a surprise to observe more than two states participating on a transition process. It means, an AC in our system can be created by the tilt

$$|1111\dots\rangle \otimes |0000\dots\rangle \xleftrightarrow{FC_0} |1011\rangle \otimes |0100\rangle,$$

as well as by transitions between energy levels coupled by the hopping terms

$$|1111\dots\rangle \otimes |0000\dots\rangle \xleftrightarrow{J_a} |1021\dots\rangle \otimes |0000\dots\rangle,$$

$$|1000\dots\rangle \otimes |2100\dots\rangle \xleftrightarrow{J_b} |1000\dots\rangle \otimes |1200\dots\rangle,$$

or by two-particle exchange W_x

$$|1211\dots\rangle \otimes |0000\dots\rangle \xleftrightarrow{W_x} |1011\dots\rangle \otimes |0200\dots\rangle,$$

which are auxiliary processes. In figure 3.12 we show the participation ratio $1/\xi_{\alpha}$ as a function of μ in the vicinity of the RET. One can see that whenever a peak appears an AC occurs and then

3. Many-Body Wannier-Stark System: Spectral Analysis

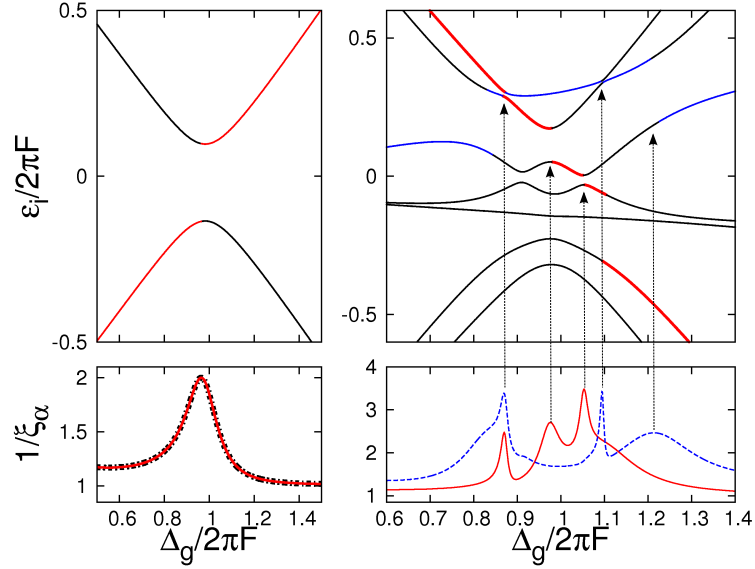


Figure 3.12: AC detection. (Left) single particle avoided crossing and the exchange of character as crossing the resonance. The lower panel shows the participation ratio $1/\xi_\alpha$ for the two eigenstates. (Right) Spectrum for $N/L = 3/2$ and the colors show the exchange of character of an initial state when crossing the sea of ACs. The lower panel shows the respective participation ratio, with maxima where the ACs occur.

the number of eigenstates involved is sometimes more than two. Additionally, the exchange of character is represented by the color change at the AC. After detecting ACs F_0 , the respective width is computed as

$$\Delta_n^{ac} = \min\{\varepsilon_{n+1}(F_0) - \varepsilon_n(F_0), \varepsilon_n(F_0) - \varepsilon_{n-1}(F_0)\}. \quad (3.75)$$

The above method offers various advantages: (i) since we can define from the beginning the character of the states before the AC detection, then one can identify the class of states and study the statistics of the respective sea of ACs. The average inverse participation ratio over the spectrum can be written as

$$\langle \xi_\alpha \rangle = \frac{1}{\mathcal{N}_s} \sum_\alpha \xi_\alpha, \quad (3.76)$$

or equivalently written in the terms of the manifolds by

$$\langle \xi_\alpha \rangle = \frac{1}{\mathcal{N}_s} \left[\sum_M d_M \langle \xi_\alpha \rangle_M \right], \quad \text{with} \quad \langle \xi_\alpha \rangle_M = \frac{1}{d_M} \sum_{\alpha=1}^{d_M} \xi_{\alpha,M}. \quad (3.77)$$

Therefore we can separately study every manifold and its respective sea of ACs. (ii) Previously, we have seen that, a maximally mixed spectra contains a large number of states in the middle of the spectrum with manifold number $0 < M < N$. Therefore, the number of ACs is expected to get larger than for the manifolds $M = 0, N$ (see Fig. 3.13). This figure shows the manifold-averaged participation ratio $1/\langle \xi_\alpha \rangle_M$, normalized to the corresponding dimension of the Hilbert space \mathcal{N}_s . The states from mid-manifold are then most susceptible to undergo changes within the RET regime, thus very good candidates to study dynamical relaxation. We shall show later the role of those states the time domain. (iii) We avoid the non-trivial of ordering the Floquet eigenenergies.

In the next section, we apply the method exposed here to study the properties of the sea of ACs.

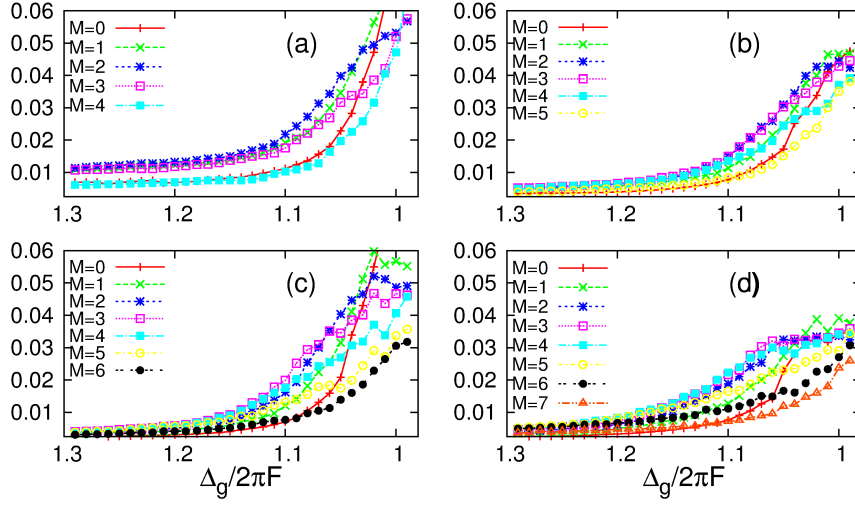


Figure 3.13: manifold-averaged participation ratio $1/\langle\xi_\alpha\rangle_M$ normalized to \mathcal{N}_s , for (a) $N/L = 4/11$ ($\mathcal{N}_s = 1150$), (b) (c) $N/L = 5/6$ ($\mathcal{N}_s = 728$), (c) $N/L = 6/5$ ($\mathcal{N}_s = 1001$) and (d) $N/L = 7/4$ ($\mathcal{N}_s = 858$). M indicates the manifold over the which the average was computed. Note that mid-manifolds mix faster when entering the RET regime, and at the exact single particle position F_r in both cases the number of eigenstates participating in the mixing grows algebraically with $\mu = \Delta_g/2\pi F$. The remaining parameters are: $V_0 = 5$ and $s_0 = 2.5$.

Density of Avoided Crossings

The term *Avoided Crossing* is connected to the concept of *coupling* between different states. It is also strongly linked to the problem of non-integrability of Hamiltonian systems, therefore to the concept *quantum chaos*. Classically, Chaos can be defined by the loss of integrals of motion due to the presence of interaction or processes which remove symmetries. In quantum mechanics, the latter is equivalent to the loss of good quantum numbers, which happens as long as ACs appear. The study of cluster of ACs becomes then an important hint to understand strongly correlated systems as our Wannier-Stark problem. Yet, the presence of ACs does not guarantee at all the transition from the regular regime to a quantum chaotic one. A couple of examples are exposed in ref. [81].

Following ref. [30], we define the density of AC, ρ_{ac} as

$$\rho_{ac}(F) = \frac{1}{\mathcal{N}_s} \frac{N_{ac}}{\Delta F}. \quad (3.78)$$

where N_{ac} is the number of ACs in the interval $[F, F + \Delta F]$. This quantity identifies the cross over between regions with any, a few and many ACs. The figure 3.14 shows $\rho_{ac}(F)$ for the system $N/L = 4/4$. Note that, around the resonance order $\mu_r = \Delta_g/2\pi F_r$, the density follows closely a gaussian profile. The peaks appearing between the resonances order are a consequence the periodicity of the Floquet eigenstates and the lack of symmetries on the spectrum. We discriminate the spectrum by colors depending on the manifold number M_i : (black) states with $M_i \rightarrow 0$, (red) $M_i \rightarrow N$ and (green) for the rest of the spectrum. One can notice again the bunches of levels, beforehand forming the manifolds, behave quite similar to the single particle eigenstates around since they totally undergo exchange of character after the RET position. Nevertheless, their properties are not that trivial.

The peaks about the resonances get embedded into the sea of ACs due to the onset of global mixing as the filling factor increases. In Fig. 3.15 we see clearly the latter phenomenon.

3. Many-Body Wannier-Stark System: Spectral Analysis

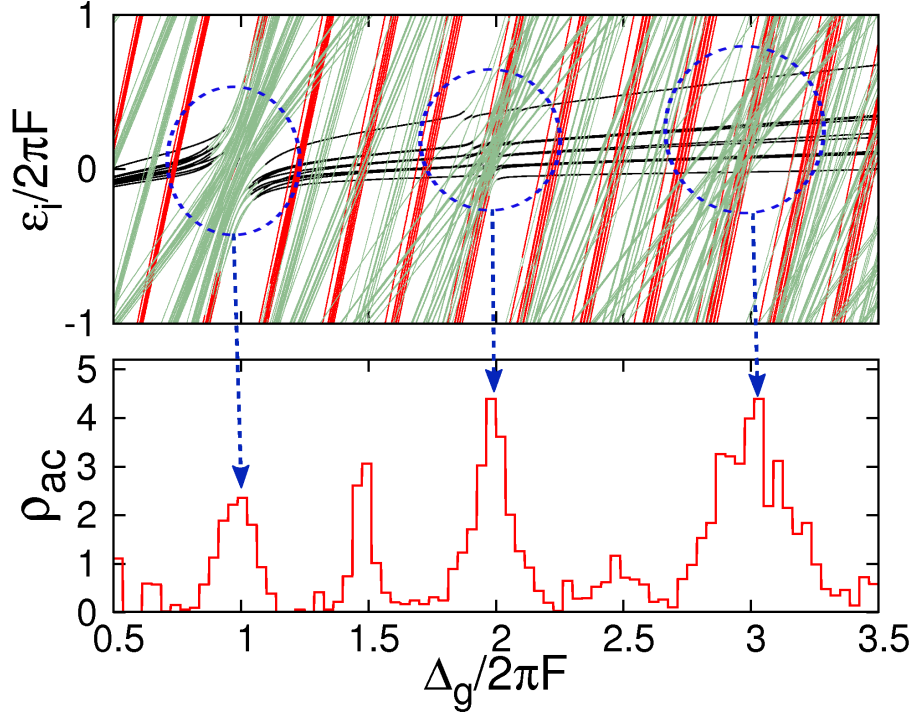


Figure 3.14: Spectrum for $N/L = 4/4$, $V_0 = 5$ and $s_0 = 2$. The colors discriminate the lowest (black: $M = 0$), highest (red: $M = N$) and the remaining manifolds (green: $0 < N < M$).

The density of ACs around the resonances becomes flatter with μ , what occurs when neighboring resonance orders overlap, as shown in Fig. 3.8. Here the density $\rho_{ac}(F)$ was computed using the whole set of seed states. The dimension of the systems used in this figure is: $\mathcal{N}_s(3/11) = 184$, $\mathcal{N}_s(4/5) = 143$, $\mathcal{N}_s(5/4) = 198$ and $\mathcal{N}_s(264) = 264$, with the step $\delta F = 1/2000$. For these small systems the number of ACs is about 10^4 , and in almost all cases when $N/L \sim 1$ the density is close to constant about the resonance with a value $\rho_{ac} \sim N/L$. This relation is important, since any localized state shall spread over the local energy domain, by dynamically tuning the force F . This spreading is the faster, the larger the sea of ACs or equivalently, as the local ρ_{ac} increases. Nevertheless, since a large number of ACs does not guarantee the presence of chaos in the system, a complete delocalization (spreading) of the initial state does not necessarily take place. We shall be back to this important issue, because of its connection with the expected spectral localization.

In our two-band Hamiltonian system there exist many different energy scales. Therefore, it is not expected to have characteristic energy scales that would control the dynamics. However, we know that, by controlling the parameters $(N/L, \Delta_g, r)$, we can induce a transition from a nearly integrable system, i.e. that one with good quantum numbers and weak manifold mixing, to the non-integrable one, for which strongly mixed spectrum was already predicted. We now want to see how the transition to quantum chaos can be established.

3.2.3 Emergence of Quantum Chaos

So far, we have studied the conditions for system to undergo either weak or strong band mixing. In addition, we have seen that the mixing properties can be well understood in terms of manifold formalism, despite the many parameters considered. That is: hopping strengths J_β ,

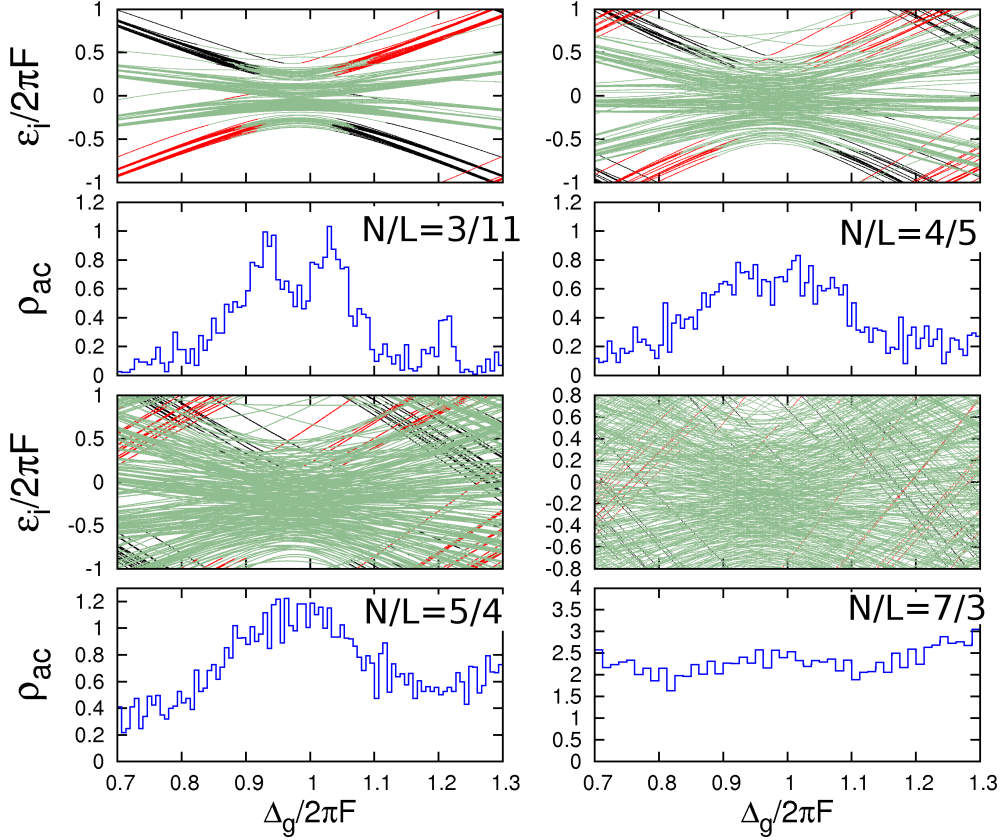


Figure 3.15: Spectrum and the corresponding density of avoided crossings ρ_{ac} for increasing filling factor: $N/L = 3/11$, $N/L = 4/5$, $N/L = 5/4$ and $N/L = 7/3$. As in the previous figures, the colors discriminate the lowest (black), highest (red) and the remaining manifolds (green).

intra- and inter-band in-situ interparticle interaction W_β and W_x , band gap Δ_g , dipole-type transitions $\{C_s\}$ and filling factor N/L . We have also showed that the spectral properties of our TBMWSH are highly sensitive to changes on any of the following parameter triplet:

$$\left(\frac{N}{L}, \Delta_g, r \right) \quad \text{with } r = 1, 2, \dots, L-1, \quad (3.79)$$

where r is the order of resonance. For typical parameters, very strong manifold mixing is reached as the ratio between the characteristic strength for one-particle exchange is comparable to the energy gap, i.e. $C_0 \sim W_x/2\Delta_g \sim 0.1$. The mixing can be enhanced in the resonant regime since the one-particle exchange is maximized by the Stark coupling (RET condition), or by decreasing the Δ_g . Both processes depend sensitively on the filling factor. We want now to establish the conditions for quantum chaos, for which spectral mixing is already one of the requirements, although not sufficient. We now use RMT tools to statistically characterize the spectrum within the resonant regime.

To compute distribution $P(s)$, keeping in mind that $s = (\varepsilon_{i+1} - \varepsilon_i)/\langle s \rangle$, the theory assumes complete randomness of the Hamiltonian matrix, then its matrix elements must be necessarily Gaussian-distributed. When working with Floquet eigenenergies, the ensemble is referred to as Circular Orthogonal Ensemble (COE), due to its periodicity. In order to compare our spectral statistics with the RMT measures, we have to find good parameter to quantify deviations between both, RMT and our numerical results. A good parameter is the *rms* deviation between

3. Many-Body Wannier-Stark System: Spectral Analysis

the cumulative distribution $I(s) = \int_0^s P(s') ds'$ and the predicted by RMT [19, 21]. This is defined as

$$rms \equiv \int_0^\infty ds [I(s) - I_W(s)]^2, \quad \text{with} \quad I_W(s) = 1 - \exp(-\pi s^2/4). \quad (3.80)$$

This quantity is better statistically analysed in the practice, when only a finite number of levels is available [19, 21, 75], $\mathcal{N}_s \sim 10^3$. An additional unfolding procedure of the TBMWSH spectrum must be done because, as seen in Fig. 3.15, the levels are not necessarily extended over the entire Floquet zone (i.e. randomization within the zone is not guaranteed). The unfolding is not necessary when $\Delta E \approx \omega_b$ and $\mathcal{N}_s \gg 1$.

To see the transition to the quantum chaotic regime, a standard measure is the parameter η defined by

$$\eta = \frac{\int_0^{g_0} (P(s) - P_W(s)) ds}{\int_0^{g_0} (P_P(s) - P_W(s)) ds}, \quad (3.81)$$

where $g_0 = 0.4729\dots$ is the intersection point between the distributions $P_P(s)$ and $P_W(s)$. This function takes the value $\eta = 1$ if $P(s)$ is Poissonian-distributed (for regular spectra) and $\eta = 0$ in the case $P(s)$ follows the Wigner surmise $P_W(s)$.

It is convenient to rescale the gauged-transformed Hamiltonian as $\hat{H}' \rightarrow \hat{H}/2\Delta_g$. Thus we obtain

$$\begin{aligned} \hat{H}' &= \frac{y}{2} \sum_{l,\beta} \left[-(\hat{\beta}_{l+1}^\dagger \hat{\beta}_l \exp(-i\omega_B t) + h.c.) + \hat{n}_l^\beta (\hat{n}_l^\beta - 1) \right] \\ &+ u \sum_l \left[2\hat{n}_l^a \hat{n}_l^b + \frac{1}{2} (\hat{b}_l^\dagger \hat{b}_l^\dagger \hat{a}_l \hat{a}_l + h.c.) \right] \\ &+ \tilde{\omega}_B \sum_{l,s} C_s \left[\hat{a}_{l+s}^\dagger \hat{b}_l \exp(-i\omega_B t) + h.c. \right] + \frac{1}{2} \sum_l \hat{n}_l^b, \end{aligned} \quad (3.82)$$

where we set

$$y = \frac{J_\alpha}{2\Delta_g} \approx \frac{W_\alpha}{2\Delta_g} \quad \text{and} \quad u = \frac{W_x}{2\Delta_g}.$$

Here, we use the known fact that, by setting $J_\beta \approx W_\beta$, the independent single-band Bose-Hubbard chains (manifolds $M = 0, N$) exhibit a quantum chaotic regime for filling factor $N/L \sim 1$ and finite Stark force [59]. The parameter u is the same plotted in Fig. 3.7. Very strong band mixing is predicted to occur when $u \sim |C_0|/r$. Note that both, u and y are proportional to Δ_g^{-1} . For typical parameters, we have $\Delta_g^{-1} \in [1/3, 10]$ if $s_0 \in [1, 6]$. In the same interval, $J_\beta \in [0.01, 0.08]$ and $W_{\beta,x} \in [0.02, 0.03]$ (see Table A.3). Therefore, without loss of generality we can set a typical values for $J_\beta, W_{\beta,x}$ and C_0 , and consider u and y only as a function of the bandgap. This also brings computational advantages when diagonalizing the Floquet operator. After the latter rescaling procedure, the onset to quantum chaos may be characterized by the interplay between single- and two-particle exchange, i.e. nothing else than the analysis of a three-diagonal block matrix that define the manifold mixing explained in Sec. 3.2.1 (see also Fig. 3.2).

For this analysis we choose systems with different filling factor and similar size of the Hilbert space. This allows one to establish a good comparison of our results for final size system, where the filling factor is the important parameter along of this work.

These systems are given in Tab. 3.1 and the results are summarized in Fig. 3.16. We compute the *rms* deviation along with the parameter η , which sets the critical values for the onset of chaos. The latter parameter falls continuously and smoother than the *rms*. Both parameters

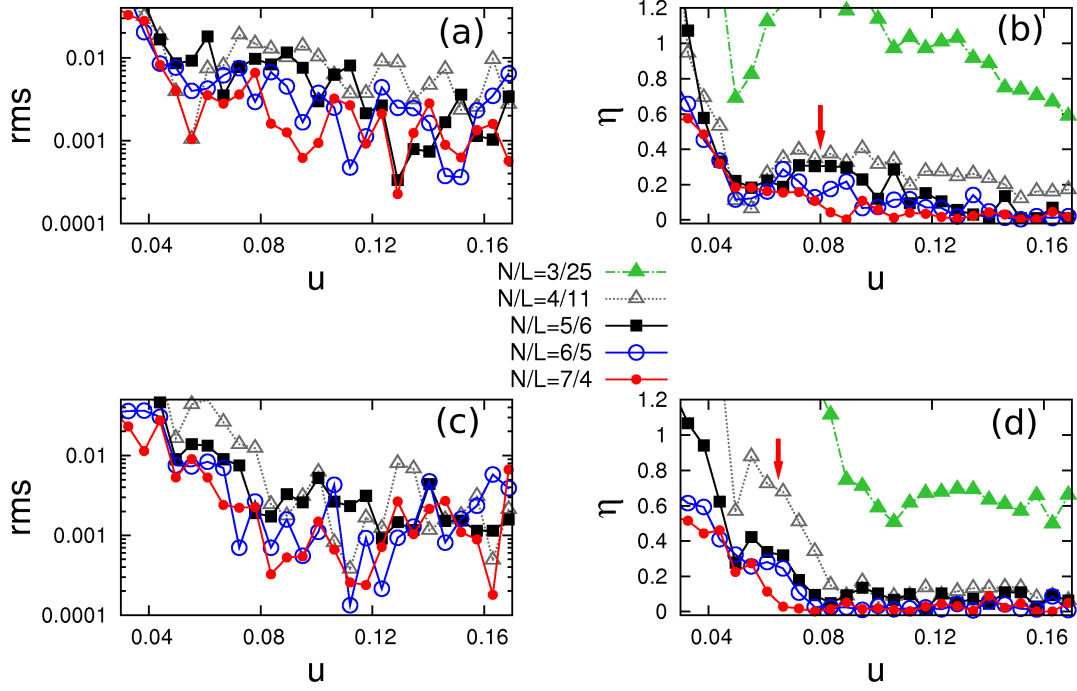


Figure 3.16: (a) and (b) show the *rms* deviation and the parameter η as a function of the ratio $u = W_x/2\Delta_g$ for different filling factors N/L , at the first order resonance. The arrow indicates the critical value at which the onset to chaos take place for systems with filling factor close to one. (c) and (d) depict the same as in the upper panels but for the second order resonance $r = 2$. Note that in both cases the onset of chaos for $N/L \sim 1$ follows the prediction stated in figure 3.7. The parameters for the rescaled gauge-transformed Hamiltonian are: $W_x = J_\beta = W_\beta = 0.05$ and $C_0 = -0.1$.

N/L	3/25	4/11	5/6	6/5	7/4
\mathcal{N}_s	884	1150	728	1001	858

Table 3.1: Filling factor N/L of the typical systems and their respective dimension.

show how good is the comparison with RTM predictions. We can see that for filling factors close to one, our prediction for strong mixing transition in Fig. 3.7 is valid. The red arrows in Fig. 3.16 indicate the critical values $|C_0|/r \sim u$. Despite the variety of used parameters used in Figs. 3.16 and 3.17, the comparison between the rescaled and non-rescaled Hamiltonian show similarities respect to the chaos onset; yet, the rescaling makes it more clear. It is also seen that for $N/L = 6/5$ and $N/L = 7/4$, the transition to full chaos is reached faster than for filling factors close to but smaller than one. Finally, figure 3.17 allows one to confirm the prediction of transition to fully quantum chaotic regime, i.e. $|C_0| \approx W_x/2\Delta_g$.

We therefore conclude that quantum chaos is always presented for filling factors close to one, similar to the condition states in ref. [59]. The statistics of the spectrum is also sensitive the bandgap. Consistent with this, when $N/L \ll 1$, the distribution $P(s)$ shows deviation to the Poissonian distribution. We show this effect in Fig. 3.18, where the distribution $P(s)$ is plotted along with their cummulative distribution. Deviation from the complete regular regime are typical in our system, where Poissonian distributions are only obtained for very large values of the gap, i.e. u must be small. The latter condition has been already explored in Eq. 3.38, where we showed that for $u \ll 1$, the dominant transition processes are given by the single particle ones.

3. Many-Body Wannier-Stark System: Spectral Analysis

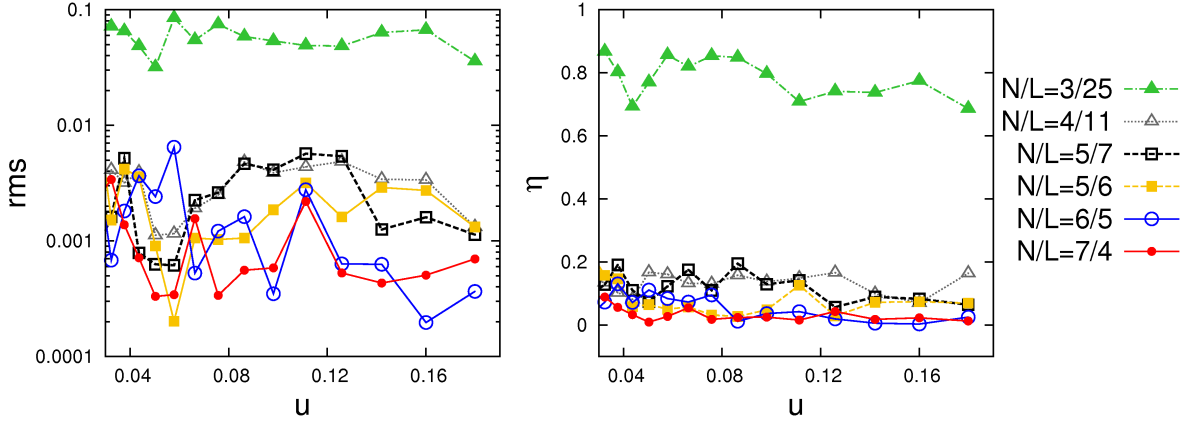


Figure 3.17: Transition to quantum chaos for the unrescaled Hamiltonian, for the several filling factors N/L at the first order of resonance. For the limit case $N/L \ll 1$, the system does not show quantum chaotic behavior. The parameters are those from table A.3.

Usually, under this effect the Bose-Hubbard chains are weakly coupled by the Stark, hence weak manifold coupling. This is the limit where M is a good quantum number.

So far, we have studied the transition to chaos at the exact value of the single particle resonance $F = F_r$. However, we must remember that mixing is present overall the entire RET domain. To study the statistics of the RET regime, it is useful to study the distribution of AC widths, for which RMT predicts full chaos if such a distribution follows the GOE prediction [105]:

$$P(c) = (1 - \gamma)\delta(c) + \gamma \left(\frac{4D}{\pi}\right)^{1/2} \exp(-Dc^2), \quad \text{with } D = \frac{\gamma}{\langle c \rangle^2 \pi}. \quad (3.83)$$

where $\gamma = 1$ implies a full chaos (strongly mixed Bloch bands), and $\gamma \rightarrow 0$ for a regular spectrum within ΔF (weakly mixed spectrum). We now use the method developed in sec. 3.2.2 to compute $P(c)$, within the interval ΔF centered at F_r . In Fig. 3.19 we show the resulting distributions for $N/L = 3/11$, $N/L = 4/5$ and $N/L = 5/4$. Those results show that, the quantum chaos onset within ΔF depends on: the filling factor and s_0 . For $s_0 = 2.5$ (upper panels), deviations from the chaotic regime are expected for all values of N/L , because the parameter $u = W_x/2\Delta_g \approx 0.017$, which is below the critical parameter $W_x/2\Delta_g \approx 0.1$. Yet, for filling factors $N/L \sim 1$, the spectra follow nearly the chaotic distribution ($\gamma \rightarrow 1$), due to the enhancement of the number of ACs within ΔF . There exists no dominant energy scale in this region. The case for $s_0 = 4$ shows clearly the transition to chaos for $N/L \sim 1$ ($u = W_x/2\Delta_g \approx 0.1$), and deviations for filling much smaller than one. The latter is expected because of the single-particle limit. Note that, the resulting distribution for $P(c)$ is in a good agreement with the corresponding $P(c)$ despite the size of the filling factor. This quantity thus is very useful to detect the onset of chaos for system with few degrees of freedom.

At this point, we can conclude:

- The critical values for quantum chaos are: $N/L \sim 1$, $|C_0|/r \sim W_x/2\Delta_g$.
- For high orders resonance, i.e. $r > 1$, the ratio $|C_0|/r$ decreases. In this way, the condition $|C_0| \sim r W_x/2\Delta_g$ only makes the system to enter in a chaotic regime when the interparticle interaction increases, i.e. if we replace $W_x \rightarrow g W_x$ with $g > 1$ (see Fig. 3.7).

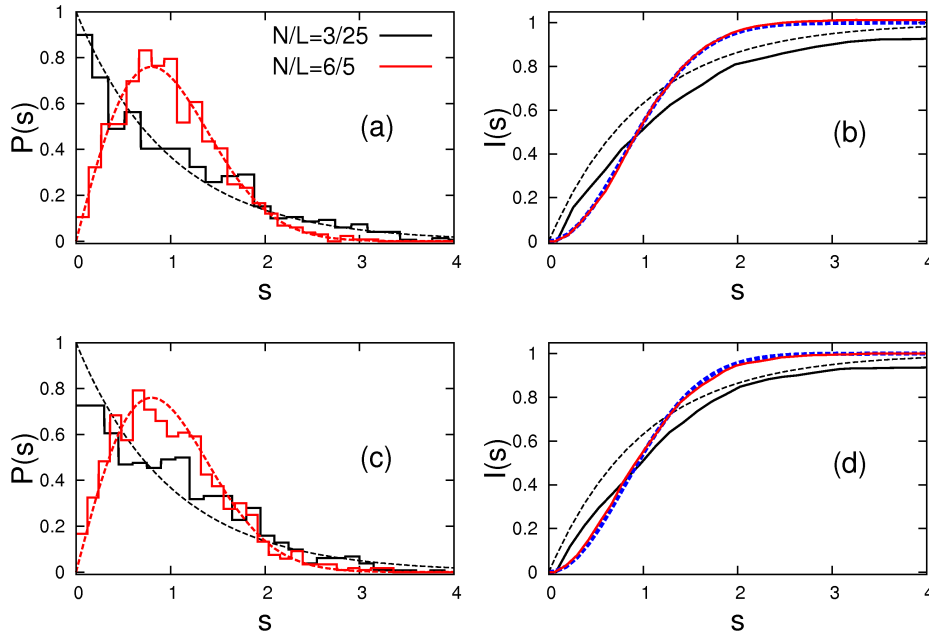


Figure 3.18: The figure shows the NNLS distribution for the systems $N/L = 3/25$ and $N/L = 6/5$ (a,b), along with the cumulative distribution $I(s)$ (c,d). Panels (a) and (b) for $V_0 = 5$ and $s_0 = 2.5$ and panels (c) and (d) for $V_0 = 5$ and $s_0 = 4.0$. The quantum chaotic distribution does not change for those system, but the Poisson one is modified as s_0 increases. For all parameters studied there is no clear signal of complete regularity in the spectrum, i.e. a correspondence with the Poissonian distribution.

- The spectrum in the limit $N/L \ll 1$ is nearly regular. To see complete transition to chaos, one must set very small values for the energy gap Δ_g , which is not possible at all with experimentally motivated parameters in Tab. A.3.
- Quantum chaos is very sensitive on the filling factor as shown by the distributions $P(s)$ and $P(c)$.

We have seen that, the occurrence of ACs is connected to the spectral mixing and chaos, especially around the resonant regime. This effect can be seen also when studying the eigenvectors of the Floquet Hamiltonian. A more precise analysis of the eigenvectors is left for the next chapter, where the connection to the dynamics is established. Yet, it is well-known fact that whenever chaos appears the eigenvector $|\varepsilon_i\rangle$ also undergoes changes in its structure [70, 74]. This can be seen by the study of the expansion coefficients, A_β , in the Fock (seed) basis, which are nearly uncorrelated in the fully chaotic regime. That is, all Fock (seed) states contribute such that A_β fluctuates about the equipartition condition $|A_\beta| = 1/\sqrt{\mathcal{N}_s}$. This is the condition for maximal hybridization, hence the Floquet eigenstates are strongly mixed states. However, we can have situations where the mixing is large, but not enough to connected the entire set of Fock (seed) states, and therefore there is no full hybridization. Under that circumstances the system does not undergo a transition to chaos, and it shall not equilibrate. In the next chapter, we show that this effect can be detected dynamically when tuning the Stark force across the RET regime.

3. Many-Body Wannier-Stark System: Spectral Analysis

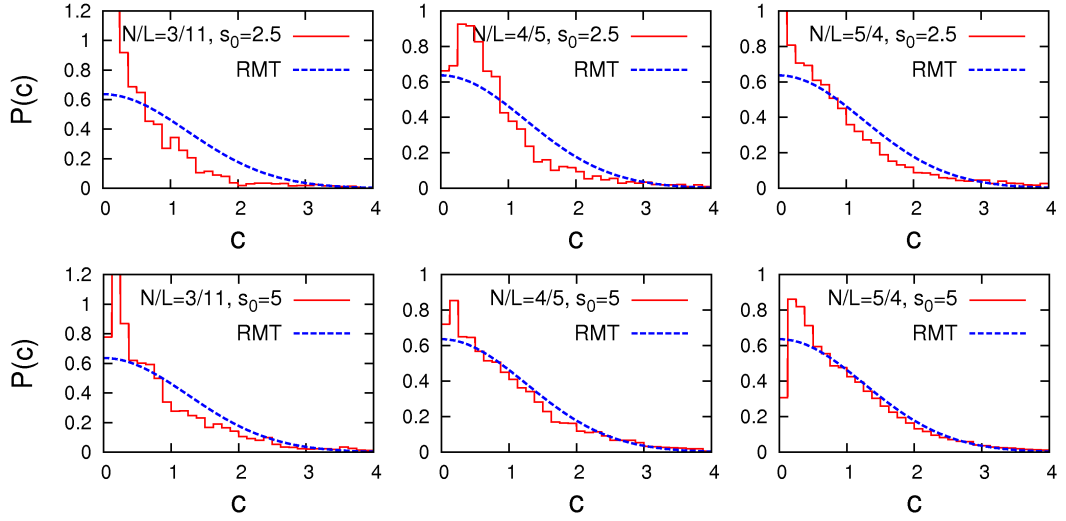


Figure 3.19: Avoided crossing widths distribution $P(c)$ for increasing filling factor N/L and $s_0 = 2.5, 5$, and $V_0 = 5$. The distributions in the upper panels correspond to the region where the ratio $W_x/2\Delta_g \approx 0.017$, where not fully chaotic behavior is expected as predicted in Fig. 3.16. For the distributions in the lower panels the value $W_x/2\pi \approx 0.14$. This regime is fully chaotic for $N/L \sim 1$. Deviations from the RMT prediction are found for chaos for filling factors $N/L \ll 1$, i.e. the single particle limit, and $N/L > 1$, where the dominant energy scale is the interparticle interaction. The set of widths $\{c_i\}$ was obtained with the method presented in sec. 3.2.2. The number of points is larger than 20000 ACs in the RET domain defined by $\frac{\Delta_g}{2\pi F} \in [0.7, 1.3]$, i.e. about the first order resonance.

3.3 Summary

Let us summarize what has been exposed until this point:

- (1) We presented our isolated many-body model: The two-band Bose-Hubbard Hamiltonian. This model was constructed starting from the miniband approximation based on an engineered bichromatic optical potential. The properties of the latter potential can be easily modified as a function of the relative amplitudes V_0 and V_1 . In fact, when decreasing the values of the energy separation between the Bloch bands, we can engineer a very well isolated system.
- (2) We have studied the emerging effects when the properties of the lattice are changed. The mixing between the Bloch bands manifests itself either local or globally in the energy spectrum, as the Stark force is changed. We have established conditions for weak and strong mixing as a function of the parameter triplet $(N/L, \Delta_g, r)$. The phenomenology can be understood by defining the M -manifolds, associated to the upperband occupation number M . We introduced the manifold mixing degree ζ , as a complementary measure to distinguish actual strong manifold mixing.
- (3) In the last section, we showed the connection between the emergence of quantum chaos and the inter-band mixing (manifold mixing). The transition occurs by the exchange of at most one or two particle between the M -manifolds. This model allows one to recognize the tight-binding nature of the our Hamiltonian, which implies a kind of spectral localization. We have shown that in spite of the large number of process considered, chaos can be activated by changing the filling factor. In the limit $N/L \ll 1$, the behavior of the system is

nearly the single-particle one, where the Hamiltonian is nearly integrable. All these regimes can be by computing the NNLS and the AC widths distributions.

Many-Body Wannier-Stark System: Dynamical Analysis

So far, we have made a detailed study of the Floquet spectrum of our many-body Wannier-Stark system. We have shown that global mixing properties are mainly controlled by the energy separation between the Bloch bands, and local mixing by the order of resonance. However, all that analysis was static, that is, neither the Stark force nor any other parameter had an explicit dependence on the time. Unfortunately, in the experiment the energy spectrum of a system as ours is not easily accessible and alternative (indirect) measurements must be employed to extract relevant information. In this way, many-body effects predicted by the static analysis can be investigated by sweeping the Stark force. Following that reasoning, we define a pulse $F = F(t)$ to study the dynamical properties by evolving various specific initial conditions across the RET regime. In this manner, we can probe the spectral properties in different dynamical regimes: adiabatic, non-adiabatic and diabatic. Relaxation towards equilibrium, controlled quantum transport and others dynamical features will be exposed, along with their connection with static properties of the spectrum.

To begin with our dynamical study, we first revisit some important dynamical aspects, whose connection with the static characteristic of the spectra can be straightforwardly established.

4.1 Adiabatic Theorem and Landau-Zener Transitions

Adiabaticity plays an important role, because this is the condition, at which any system can transform its properties during the long-time passage across an avoided crossing. The other limit is the diabatic condition, for which the initial state essentially remains unchanged [106]. This limit is usually referred to as a sudden sweep. Paradigmatically, non-adiabatic transitions also occur with a probability given by the celebrated Landau-Zener formula [65, 66, 68]

$$P_{LZ} = e^{-\pi/\gamma}, \quad \text{with } \gamma = \frac{4\alpha}{(\Delta E)^2}, \quad (4.1)$$

which is valid only for a two-level AC. ΔE is the width of the AC and α is the sweeping rate.

In our problem, a Landau-Zener scenario is easily set by the single particle limit around the resonant regime. There an isolated avoided crossing occurs due to the interaction between the Wannier-Stark ladders (see Fig. 3.3). Furthermore, one defines the initial conditions to be the state with one particle occupying the l th lattice site in the lowest Bloch band. In this way, it is possible to promote the particle to the upperband. In order to do this we define the linear

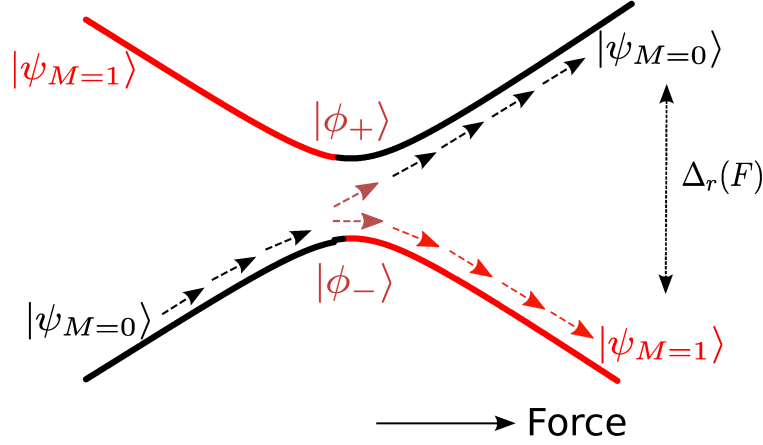


Figure 4.1: Landau-Zener scenario for the single-particle spectrum. The manifold states $|\psi_{M=0}\rangle$ and $|\psi_{M=1}\rangle$ represent the diabatic states far apart from the resonance F_r . $|\phi_{\pm}\rangle$ represents the maximally hybridized state created by the passing across the AC. $\Delta_r(F(t))$ is the energy separation, in our case corresponding to the various the manifold states with $\Delta M = \pm 1$.

pulse $F(t) = \alpha t + F_0$ and sweep the system across any resonant position F_r . The particle can tunnel r lattice sites until it occupies an upperband state at the exact resonance. In terms of M -manifolds, the latter setup is the one-particle exchange process between the manifolds $M = 0$ and $M = 1$. The respective manifold states, $|\psi_{M=0}\rangle$ and $|\psi_{M=1}\rangle$, far apart from the resonant regime can be considered as the diabatic states sketched in Fig. 4.1. The exchange of character expected to occur at F_r and it is represented by the change of color of the eigenenergy "path" (see also the arrows) at the exact resonance. At this point, the diabatic states get completely hybridized, which is represented by the states $|\phi_{\pm}\rangle$. The latter allows one to conclude that the static spectrum, studied in the previous chapter, is nothing else than the time-domain representation of the adiabatic limit, i.e. $\alpha \rightarrow 0$. Let ΔT be the time expended to drive the system from a starting tilt $F_0 < F_r$ to a final one $F_f > F_r$. We shall referred to ΔT as the sweeping time. In the practice, ΔT is finite.

The survival probability $P_{M,0}$ of an initial state $|\psi(0)\rangle = |\psi_{M=0}\rangle$ is plotted as a function of the parameter $F(t)$. An estimate for the sweeping time can be set by the Heissenberg relation

$$\Delta T \Delta E \approx \hbar, \quad \text{with } \hbar = 1. \quad (4.2)$$

The sweeping rate is then given by

$$\alpha = \frac{\Delta F}{\Delta T} \simeq \lambda \Delta F \Delta E, \quad (4.3)$$

where ΔF is the effective interval of tilts F at which the coupling between the diabatic states effectively starts. λ is a parameter controlling the type of dynamics expected when crossing the resonance: Diabatic ($\lambda \gg 1$), non-adiabatic ($\lambda \sim 1$) and adiabatic ($\lambda \ll 1$) passage (see Fig. 4.2).

The extended version of the Landau-Zener problem, i.e. the multi-state problem, is naturally obtained by increasing the particle number, hence the number of manifolds. In the non-interacting case ($W_i = 0$), the tight-binding-type Hamiltonian (3.22) has an energy spectrum, whose shape resembles a bow tie-like shown Fig. 4.3-(left). The time-dependent energies $\varepsilon_r(F(t))$ define the energy gap between two contiguous manifolds as

$$\Delta_r(F(t)) \simeq \Delta_g \sqrt{\left(1 - \frac{F(t)}{F_r}\right)^2 + 4 \left(\frac{F(t)C_0}{\Delta_g}\right)^2}. \quad (4.4)$$

4. Many-Body Wannier-Stark System: Dynamical Analysis

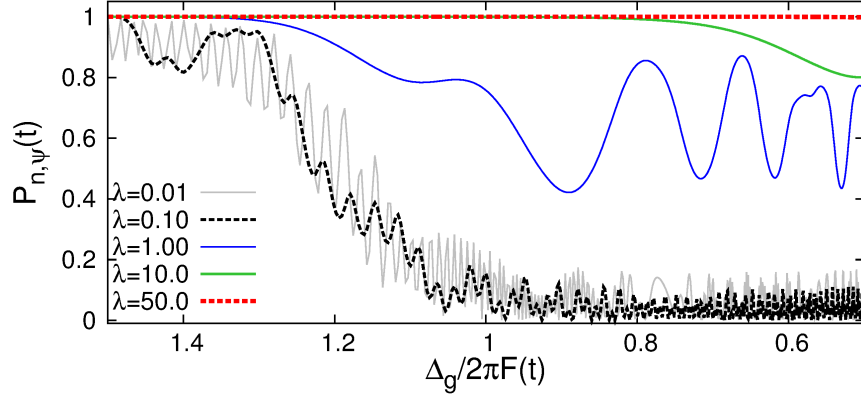


Figure 4.2: Landau-Zener transition: The figure shows the time-dependent survival probability $P_{M,0}$ for the initial state $|\psi(0)\rangle = |\psi_{M=0}\rangle$. Its behavior is plotted for different regimes of the time evolution set by the parameter λ , where $F(t) = \alpha t + F_0$. The position of the avoided crossing is given by $\frac{\Delta_g}{2\pi F(t)} = 1$. The remaining parameters are $V_0 = 5$, $s_0 = 1$, $F_r = 0.4224$ and $N/L = 1/6$.

We now define the Bloch period $T_B = 1/F_r$. Our non-interacting many-body system is usually referred to as the bow-tie problem for multi-state Landau-Zener scenario [107–109], for which there exists exact solutions. That is, analytically solutions for the transition probabilities between the different M -sets. In figure 4.3 we show manifold excitation probability $P_{M,0}(F(t))$ as a function of the time. It is important to see that all probabilities start oscillating in time right after the full depletion of the lower channel probability takes place $t = 5 T_B$. This happens right before the resonance position $F_r = 0.422$. The oscillations reduce as long as the system is swept across the RET regime, and after the AC, the higher manifold is more populated than the rest. This calculation was done considering $\lambda = 1$ and it takes less than hundred Bloch periods to excite the higher manifold with an occupation probability larger than 50% for the manifold $M = N$. Of course, this simple evolution process becomes more complex when turning on the interactions. In that limit, the calculation of the analytically the probabilities P_M is a way more complicated. We have already discussed this complexity in the static analysis (see sec. 3.2).

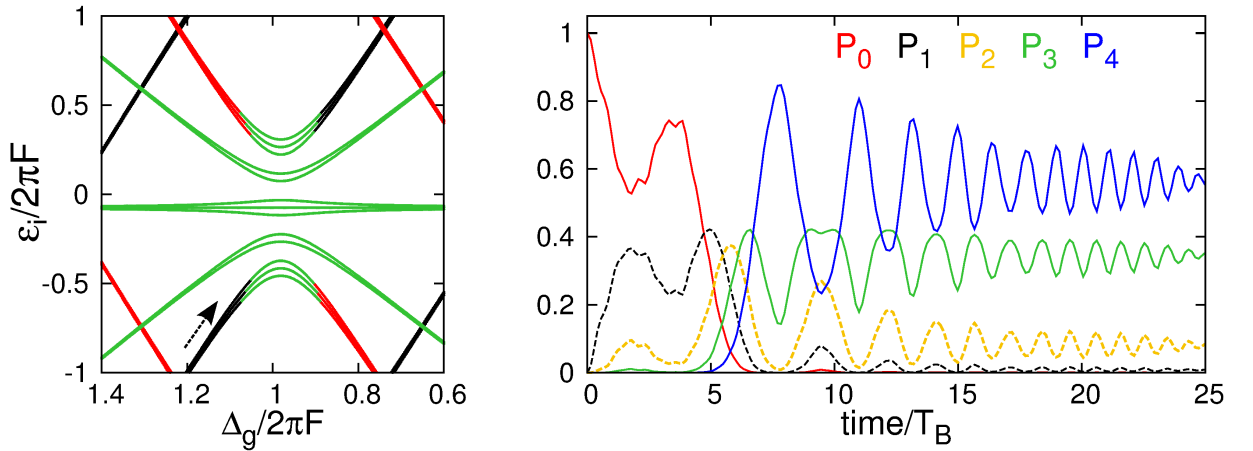


Figure 4.3: (Right) Bow-tie-shaped static energy spectrum for the system $N/L = 4/4$. The arrow indicates the starting manifold $M = 0$. (Left) Time evolution of the manifold occupation probabilities $P_{M,0}(F(t))$ with $\lambda = 1$ and initial state $|\psi(0)\rangle = |1111\rangle_a \otimes |0000\rangle_b$.

In the following, we study the evolution across the many-body spectrum, again, by considering the experimentally motivated linear pulse $F(t)$. We will see that all knowledge of the static problem is very useful to understand, e.g. dynamical manifold mixing, relaxation and other interesting many-body effects, along with their dependence on the different system parameters.

4.2 Ergodicity and Mixing

Let us do the following experiment. A system initially prepared in the state $|\psi(0)\rangle_{F_0}$ is suddenly swept from F_0 to F_r and then it is left to evolve in time such that $F = F_r$ is fixed. This implies that the evolution is generated by the time evolution operator \hat{U}_{TB} (3.13). For fixed Stark force, the dynamics is governed by the gauge-transformed Hamiltonian (3.9), then we can use the Floquet formalism B.6 to compute the evolution of $|\psi(0)\rangle_{F_r}$. When the evolution starts, so does mixing. In this way, the inter-band coupling can be investigated through the upperband occupation number $M(t)$ [64, 81]. Here, we are interested in long-time behavior of the time average of the projectors \hat{P}_α , which reads

$$\begin{aligned} \langle \psi(t) | \hat{P}_\alpha | \psi(t) \rangle &= \sum_n |c_{n,0}|^2 \langle \varepsilon_n(t) | \hat{P}_\alpha | \varepsilon_n(t) \rangle \\ &+ \sum_{n \neq m} c_{n,0}^* c_{m,0} e^{-i(\varepsilon_n - \varepsilon_m)t} \langle \varepsilon_n(t) | \hat{P}_\alpha | \varepsilon_m(t) \rangle, \end{aligned} \quad (4.5)$$

where $c_{n,0} = \sum_k \langle \phi_n^k | \psi(0) \rangle$ and $|\varepsilon_n(t)\rangle = \sum_k e^{-i\omega_B k t} |\phi_n^k\rangle$. The long-time average of the first term in the right-hand side is computed as follows

$$\begin{aligned} \overline{\langle \varepsilon_n(t) | \hat{P}_\alpha | \varepsilon_n(t) \rangle} &= \lim_{\tau \rightarrow \infty} \frac{1}{\tau} \int_0^\tau dt \langle \varepsilon_n(t) | \hat{P}_\alpha | \varepsilon_n(t) \rangle \\ &= \sum_{k,k'} \left(\lim_{\tau \rightarrow \infty} \frac{1}{\tau} \int_0^\tau dt e^{-i\Delta_{k,k'} \omega_B t} \right) \langle \phi_n^{k'} | \hat{P}_\alpha | \phi_n^k \rangle \\ &= \sum_{k,k'} \delta_{k,k'} \langle \phi_n^k | \hat{P}_\alpha | \phi_n^k \rangle \end{aligned} \quad (4.6)$$

$$= \sum_k \langle \phi_n^k | \hat{P}_\alpha | \phi_n^k \rangle, \quad (4.7)$$

where we have expanded $|\phi_n^k\rangle$ in the seed basis, $|\phi_n^k\rangle = \sum_\beta c_{n,\beta}^k |s_\beta\rangle$. By using $\hat{P}_\alpha = |s_\alpha\rangle\langle s_\alpha|$, we obtain

$$\overline{\langle \varepsilon_n(t) | \hat{P}_\alpha | \varepsilon_n(t) \rangle} = \sum_k |c_{n,\alpha}^k|^2 |c_{n,\alpha}|^2. \quad (4.8)$$

For the second term of (4.5) we have:

$$\sum_{n \neq m} c_{n,0}^* c_{m,0} \overline{\langle \varepsilon_n(t) | \hat{P}_\alpha | \varepsilon_m(t) \rangle} = \sum_{n \neq m} c_{n,0}^* c_{m,0} \sum_{k,k'} (c_{n,\alpha}^{k'})^* c_{m,\alpha}^k \Lambda_{k,k'}(t), \quad (4.9)$$

with $\Lambda_{k,k'} \equiv \overline{e^{-i(\omega_{n,m} - \Delta_{k',k} \omega_B)t}}$, $\omega_{n,m} = \varepsilon_n - \varepsilon_m$ and $\Delta_{k',k} = k' - k$. By choosing the initial condition to be a seed state, for instance $|\psi(0)\rangle = |s_\nu\rangle$ we get

$$\begin{aligned} \bar{P}_\alpha(F; |s_\nu\rangle) &\equiv \overline{\langle \psi(t) | \hat{P}_\alpha(t) | \psi(t) \rangle} \\ &= \sum_n |c_{n,0}|^2 |c_{n,\alpha}|^2 \\ &+ \sum_{n \neq m} c_{n,0}^* c_{m,0} \sum_{k,k'} (c_{n,\alpha}^{k'})^* c_{m,\alpha}^k \Lambda_{k,k'}(t), \end{aligned} \quad (4.10)$$

4. Many-Body Wannier-Stark System: Dynamical Analysis

which is the average occupation probability of the state $|s_\alpha\rangle$ given initial state $|\psi(0)\rangle = |s_\nu\rangle$. In particular, when $\nu = \alpha$, it is possible to rewrite the Eq. (4.10) in terms of the inverse participation ratio

$$\bar{P}_\alpha(F; |s_\alpha\rangle) = \xi_\alpha + \sum_{n \neq m} c_{n,0}^* c_{m,0} \sum_{k,k'} (c_{n,\alpha}^{k'})^* c_{m,\alpha}^k \Lambda_{k,k'}(t) \quad (4.11)$$

with $\xi_\alpha = \sum_n |c_{n,\alpha}|^4$ and $c_{n,\alpha} = \langle \varepsilon_n | s_\alpha \rangle$ (see (B.5)). The expression of the inverse participation ratio can be written as mean value over the energy spectrum, i.e.

$$\xi_\alpha = \sum_j |\langle \varepsilon_j | s_\alpha \rangle|^2 |\langle \varepsilon_j | s_\alpha \rangle|^2 = \sum_j p_j^\alpha \langle \varepsilon_j | s_\alpha \rangle \langle s_\alpha | \varepsilon_j \rangle = \sum_j p_j^\alpha \langle \varepsilon_j | \hat{P}_\alpha | \varepsilon_j \rangle, \quad (4.12)$$

where p_j^α is the occupation probability of the eigenstate $|\varepsilon_j\rangle$ and satisfies the normalization condition $\sum_j p_j^\alpha = 1$. Therefore, we recognize that the equation (4.12) is the spectral average for the projector P_α . We conclude that for any initial condition $|s_\alpha\rangle$ the system becomes ergodic if

$$\bar{P}_\alpha(F; |s_\nu\rangle) \approx \xi_\alpha = \sum_j p_j^\alpha \langle \varepsilon_j | \hat{P}_\alpha | \varepsilon_j \rangle, \quad (4.13)$$

which is satisfied if the function $\Lambda_{k,k'}$ drops faster to zero. In fact, this is satisfied whenever the system has no additional symmetries, i.e. if there are no degeneracies, and therefore the presence of ACs. We can prove that $\Lambda_{k,k'}$ always goes to zero under the latter conditions. Suppose that the function $\Lambda_{k,k'}$ is different from zero. This implies that the condition $\omega_{n,m} = \Delta_{k,k'} \omega_B$ must be fulfilled with $\omega_{n,m} \neq 0$. Thus the integer $|k - k'| > 0$. Because of the periodicity of the Floquet eigenenergies, we know that any integer $|k - k'|$ maps a single energy from the fundamental Floquet zone onto the $|k - k'|$ -zone, and it is exactly the same eigenenergy. Therefore, we have $\varepsilon_n = \varepsilon_m + \Delta_{k,k'} \omega_B \equiv \varepsilon_m$, and the difference $\Delta_{k,k'} \omega_B = 0$. This is just a contradiction, therefore $\Lambda_{k,k'}$ has to be equal to zero.

As an example of this underlying ergodicity of our system, in Fig. 4.4 we show a comparison between the inverse participation ratio and the spectral average of the projector representing the initial state $|\psi(0)\rangle \equiv |s_\alpha\rangle = |1111\rangle_a \otimes |0000\rangle_b$. The closer to the resonant regime, the better the comparison, which is the region where the sea of ACs appears, hence a high degree of mixing. The projector \hat{P}_α can thus mix with the entire Hilbert space. Other observables, for instance occupation number operator $\hat{M} \equiv \hat{N}_b$, cannot be written in terms of only one Fock (seed) state projector but as a linear combination of all of them. Therefore, when computing its long-time average, they contain more information from the entire spectrum. This is the reason for the almost perfect matching between its time and spectral average, i.e. $\bar{N}_b(F; |s_\nu\rangle) \approx \sum_j |c_{j,0}|^2 \langle \varepsilon_j | \hat{N}_b | \varepsilon_j \rangle$ (see Fig. 4.4-upper panel). This result is very important because it claims itself that the spectral properties of the Hamiltonian system with fixed Stark force are determined by the long-time averages of its dynamical properties (mixing and occupation numbers), whenever the system is restricted to a specific class of symmetry. An important consequence of the above analysis comes into the play. Let us suppose that the spectrum at $F = F_r$ is chaotic, i.e. if the local eigenenergies yield to GOE-distributed $P(s)$. In this case, the Floquet eigenstates are also chaotic, the coefficients $\{c_{j,\alpha}\}$ randomize such that they are gaussian-distributed. In this way, the variable $y \equiv |c_{j,\alpha}|^2 / \langle c^2 \rangle$, with $\langle c^2 \rangle \equiv \langle |c_{j,\alpha}|^2 \rangle$, must follow the GOE Porter-Thomas distribution [73] (see App. C). Using this distribution and following ref. [110], the spectral average for the projector \hat{P}_α (4.13) can be computed as

$$\xi_\alpha = \mathcal{N}_s \langle c^2 \rangle^2 \int_0^\infty dy P(y) y^2, \quad P(y) = \frac{1}{\sqrt{2\pi y}} \exp(-y/2), \quad (4.14)$$

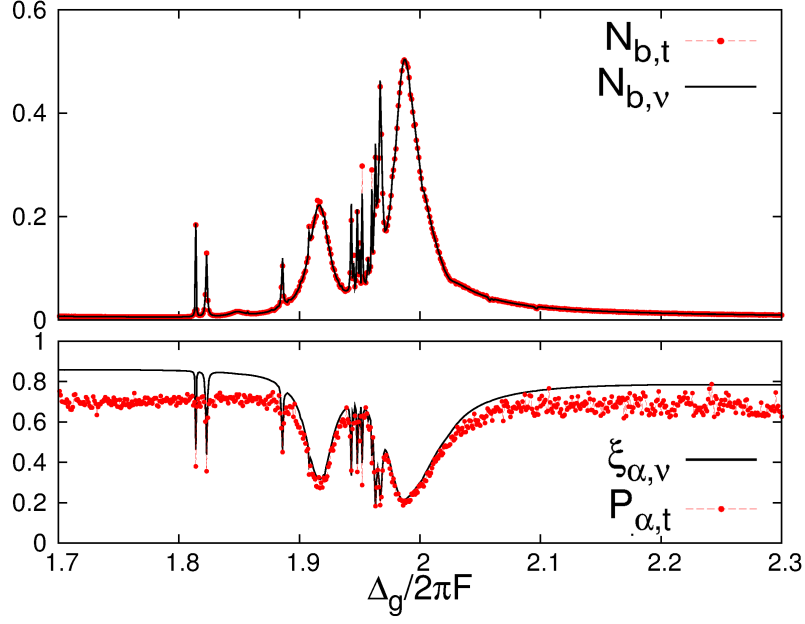


Figure 4.4: Comparison between spectral and long-time averaged for the upperband occupation N_b (upper panel), and the projector \bar{P}_α representing the initial state $|\psi(0)\rangle = |1111\rangle_a \otimes |0000\rangle_b$ (lower panel), corresponding to the system $N/L = 4/4$.

This integral is accessible, therefore we obtain

$$\xi_\alpha^{\text{goe}} = 3/\mathcal{N}_s, \quad (4.15)$$

which is the GOE limit for strong mixing condition, and the minimal value for relaxation reached for the initial state $|\psi(0)\rangle$ after the quench. This is the condition for equilibrium usually defined in the context of the energy shell approximation [110, 111].

The results obtained in this section will be very important to understand the rest of this chapter. We highlight that the ergodic nature of our system is not enough to obtain the GOE limit for equilibrium. A second component is very important: quantum chaos.

From the latter analysis we can see that our system becomes ergodic if there is spectral mixing (manifold mixing). However, the presence of mixing, for instance in the non-adiabatic regime, does not guarantee ergodicity since there is not necessarily mixing of the initial state with the entire Hilbert space. This is a well-known fact in the statistical mechanics. We shall come back to this discussion when we study the dynamical relaxation process in our system, which will be described in the next sections.

4.3 Spectral Diffusion in the Many-body Interacting Regime

In section 4.1 we have shown the simplest cases for evolution across the RET regime, say, the case $N = 1$ and the many-body non-interacting system. Such a kind of time-evolution is more complicated when turning on the interactions between the particle ($W_i \neq 0$), because the evolved state has to cross the entire RET regime where many ACs cluster. Furthermore, when high degree of mixing is present, for instance in a case $N/L > 1$, there is no characteristic energy scale which would permit an easy driving of a many-body initial condition. We have then a very

4. Many-Body Wannier-Stark System: Dynamical Analysis

complex setup provided by the sea of ACs and several interesting dynamical processes will take place due to the cascade of single Landau-Zener (LZ) events.

Before studying how the system diffuses, we have to consider the effects of the parametric-time evolution on the Hamiltonian properties and also establishing useful definitions for the rest of our analysis. First, we note that the properties of the pulse $F(t)$ can change symmetry properties of the gauged-transformed Hamiltonian in Eq. (3.9). Let us rewrite the time-dependent Hamiltonian as

$$\hat{H}(t) = \hat{H}_0 + \hat{J}^\dagger e^{-i2\pi F(t)t} + \sum_s \hat{C}_s^\dagger e^{-i2\pi s F(t)t} + h.c., \quad (4.16)$$

where \hat{H}_0 contains all time-independent terms, \hat{J} is the hopping term and \hat{C}_s the dipole-induced interband coupling. In the previous chapter the force has been considered a time-independent parameter $F(t) = F$, which implies that the Hamiltonian has a well defined time periodicity given by the Bloch period $T_B = 2\pi/\omega_B$. The time evolution of any initial state is then computed by the stroboscopic quantum map

$$|\psi((m+1)T_B)\rangle = \hat{U}_{T_B} |\psi(mT_B)\rangle, \quad \text{with} \quad \hat{U}_{T_B} = \hat{\mathcal{T}} \exp \left[-i \int_0^{T_B} \hat{H}(t) dt \right]. \quad (4.17)$$

Additionally, the system is time-reversal invariant because it fullfills the conventional reversal operation

$$t \rightarrow -t, \quad \hat{H}(t) = T \hat{H}(-t) T^{-1}, \quad (4.18)$$

where one must additionally change $i \rightarrow -i$, in order to preserve the antiunitary character of T . By definition the time-dependent pulse is given $F(t) = \alpha t + F_0$. The immediate consequences of this choice are:

- (a) The Hamiltonian $H(F(t))$ is no longer periodic in time. In consequence, we must compute the temporal evolution explicitly by integrating the Schrödinger equation

$$i \frac{\partial}{\partial t} \hat{U}_t |\psi(0)\rangle = \hat{H}(t) \hat{U}_t |\psi(0)\rangle, \quad (4.19)$$

e.g. by using a fourth-order Runge-Kutta method. The initial state $|\psi(0)\rangle$ can be chosen to be an eigenstate of the Floquet operator at any position of the spectrum. In order to integrate the equation (4.19), we use the closure relation for seed states $\sum_v |s_v\rangle \langle s_v| = \mathbf{1}$, which allows to rewrite the Schrödinger equation as a system of first order differential equations for the coefficients $A_v(t) \equiv \langle s_v | \hat{U}_t |\psi(0)\rangle$. The instantaneous wavefunction $|\psi_t\rangle$ can be thus expanded in the seed basis as

$$|\psi(t)\rangle = \sum_{v=1}^{\mathcal{N}_s} A_v(t) |s_v\rangle. \quad (4.20)$$

- (b) $F(t)$ breaks the time-reversal symmetry even by setting $F_0 = 0$, for which the function $F(t)$ is odd.

Both, (a) and (b) also imply that the coefficients $A_v(t)$ are complex numbers and their properties are different from those followed for the coefficients $c_{n,v}$ which are real numbers. We shall come back later to this crucial difference.

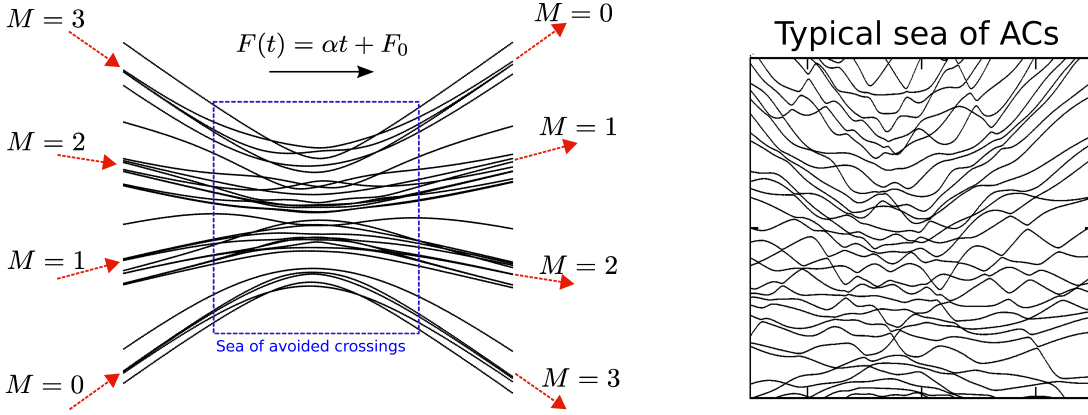


Figure 4.5: (Left) Many-body avoided crossing for $N/L = 4/4$. The label M indicates the set of levels corresponding to the specific manifold. (Right) Typical sea of ACs occurring in the resonant regime for filling factor $N/L = 5/3$ (see also Fig. 3.10).

The Setup

In figure 4.5, we present a typical many-body avoided crossing around one of its resonances F_r . In the left part of the spectrum we label the different manifolds, which are formed by bunches of energy levels entering nearly parallel to each other and emerging after the resonance with the same slope. If the system is initially prepared in the manifold $M = 0$, and it is adiabatically driven across the RET, we expect a final state living in a different manifold, or in general, in a superposition of them.¹ For the diabatic passage, the system must preserve with its manifold character high probability. Yet, in the practice, long-time processes are not useful in the different applications, therefore non-adiabatic dynamics is the most common case.

The choice of the initial state for the evolution plays also an important role. In our system, we have basically two natural sets: the seed basis $\{|s_\nu\rangle\}$ and the eigenstates of the static problem. We must remember that for large enough energy gaps Δ_g , one of the most interesting properties of the static spectrum is that, its eigenstates can be classified by manifolds since they have a high probability of being completely mapped one-to-one onto the members of the seed basis. Other additional initial conditions can be constructed from those two subsets, if necessary.

Measures

To quantify the diffusion in energy space, we compute the instantaneous projections

$$C_i(t) \equiv \langle \varepsilon_i(F_k) | \psi(F(t)) \rangle, \quad \text{with} \quad |\psi(F(t))\rangle = U_t |\psi(F_0)\rangle. \quad (4.21)$$

where $|\varepsilon_i(F_k)\rangle$ is the local adiabatic eigenstate at the instantaneous tilt $F(t) = F_k$. One can think the local eigenbasis as a set of detectors, for which $|C_i(t)|^2$ represents the detection probability of the instantaneous state $|\psi(t)\rangle$, with $\sum_i |C_i|^2 = 1$.

In order to visualize the transit of the instantaneous eigenstate, it is very useful to introduce the *local density of states* (LDOS) [103, 110], also called strength function. This is defined by

$$P_\psi(\varepsilon, F(t)) = \sum_i |C_i(t)|^2 \delta(\varepsilon - \varepsilon_i). \quad (4.22)$$

¹See for instance right panel in Fig. 4.3

4. Many-Body Wannier-Stark System: Dynamical Analysis

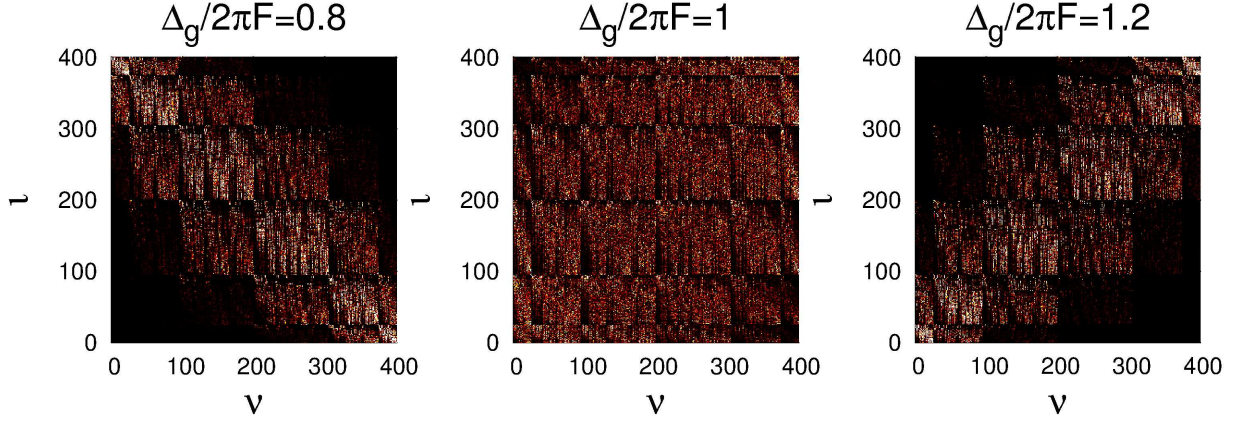


Figure 4.6: Matrix of probabilities $|\langle \varepsilon_i | s_v \rangle|^2$ for the system $N/L = 5/5$, $V_0 = 5$ and $s_0 = 2$, and three different positions in the spectrum around the first order resonance $r = 1$: (left) for $F > F_r$, (middle) $F = F_r$ and (right) $F < F_r$.

At F_0 , $P_\psi(\varepsilon, 0)$ is δ -shaped, when the initial state is chosen as a Floquet eigenstate. But if we consider a seed state $|\psi(F_0)\rangle = |s_v\rangle$, its representation in the local energy basis contains contributions from the neighboring eigenenergies: $|\psi\rangle$ in the eigenenergy basis as

$$|\psi(F_0)\rangle \equiv |s_v\rangle = \sum_i |\varepsilon_i(F_0)\rangle \langle \varepsilon_i(F_0) | s_v \rangle. \quad (4.23)$$

In this case P_ψ takes a shape given by the *Breit-Wigner* formula [112, 113]

$$P_\psi(\varepsilon, F_0) \sim \frac{1}{\pi} \frac{\Gamma^2}{(\varepsilon - \varepsilon_0)^2 + \Gamma^2}, \quad (4.24)$$

with ε_0 the center of the distribution. The width Γ of this distribution determines how generic our initial condition is and it is computed by the energy deviation

$$\Gamma = \left(\sum_i |\langle \varepsilon_i(F_0) | s_v \rangle|^2 (\varepsilon_i - \varepsilon_0)^2 \right)^{1/2}. \quad (4.25)$$

An initial state is called generic if $\Gamma \ll \varepsilon_0$ [22, 24]. An example of this is shown in Fig. 4.6 for the system $N/L = 5/5$. There it is possible to recognize the manifold formation and the exchange of character of the eigenstates represented by the rotation of the probability matrix, when crossing the resonance (from right to the left or vice versa). At the exact resonance an initial condition is not generic as expected, since a lot of manifold mixing is present.

The delocalization of the instantaneous state $|\psi(t)\rangle$ can be studied by computing its second moment of $P_\psi(\varepsilon, t)$ given by

$$\int d\varepsilon \rho(\varepsilon) P_\psi^2(t) = \sum_i |C_i(t)|^4 \equiv \xi_\psi(t), \quad (4.26)$$

where ξ_ψ is the inverse participation ratio (3.34). This relation is valid when integrating over large number of Floquet zones. Now we quantitatively characterize the spreading over the spec-

4.3. Spectral Diffusion in the Many-body Interacting Regime

trum by the average inverse participation ratio and the Shannon entropy, both defined as

$$\xi(F(t)) \equiv \left\langle \sum_{i=1}^{\mathcal{N}_s} |C_i(t)|^4 \right\rangle_{\psi} \quad (4.27)$$

$$S_{\text{sh}}(F(t)) \equiv \left\langle -\frac{1}{\log_{10} \mathcal{N}_s} \sum_{i=1}^{\mathcal{N}_s} |C_i(t)|^2 \log_{10} |C_i(t)|^2 \right\rangle_{\psi}, \quad (4.28)$$

respectively. The averages $\langle \dots \rangle_{\psi}$ are taken over a large set of similar initial conditions $\{|\psi(F_0)\rangle\}$, for instance, those states from a M -manifold. The same measures can be implemented for coefficients A_v that expand the state $|\psi(F(t))\rangle$ in the seed basis (4.20), and it will be shown that the information extracted from the instantaneous coefficients A_v is also very useful for predictions on the evolution.

Due to the local sea of ACs and the strong mixing generated in RET, complete delocalization of the initial condition is expected. The coefficients $|C_i|$ and $|A_v|$ fluctuate about the equipartition condition $1/\sqrt{\mathcal{N}_s}$. The localization measures slowly converge to their respective values, which can be computed under the assumption of complete randomness, i.e. no correlations between the coefficients. The problem here is that any of these sets of coefficients satisfies a normalization condition due to the probability conservation of the evolved eigenstate

$$\sum_{i=1}^{\mathcal{N}_s} |C_i(t)|^2 = 1, \quad \text{and} \quad \sum_{v=1}^{\mathcal{N}_s} |A_v(t)|^2 = 1, \quad (4.29)$$

and therefore we have $\mathcal{N}_s - 1$ independent contributions. When Chaos is present, the randomness of the above sets is guaranteed. Then RMT predicts a Porter-Thomas distribution [73, 74] for the normalized absolute square of the coefficient C_i and A_v (as in the case of $c_{n,\alpha}$ in sec. 4.2). This allows one to compute the mean values of the localization measures as

$$\xi = \mathcal{N}_s \langle c^2 \rangle^2 \int_0^{\infty} dy f(y) y^2 \quad (4.30)$$

$$S_{\text{sh}} = \mathcal{N}_s \int_0^{\infty} dy f(y) y \langle c^2 \rangle \ln(y \langle c^2 \rangle), \quad (4.31)$$

with

$$y \equiv \left\{ \frac{|C_i|^2}{\langle c^2 \rangle}, \frac{|A_v|^2}{\langle c^2 \rangle} \right\}, \quad \langle c^2 \rangle \equiv \{ \langle |C_i|^2 \rangle, \langle |A_v|^2 \rangle \}. \quad (4.32)$$

and the distribution $f(y) = e^{-y}$ (see App. C). The values obtained from Eqs. (4.30) are a very accurate if the size Hilbert space is large enough, $\mathcal{N}_s \gg 1$. The mean values are given by

$$\xi_{\text{gue}} = \frac{2}{\mathcal{N}_s}, \quad S_{\text{sh}}^{\text{gue}} = \left(1 - \frac{\gamma_c}{\ln(\mathcal{N}_s)} \right), \quad \text{with } \gamma_c = 0.422784... \quad (4.33)$$

In addition, in the time-domain, we can compute the manifold mixing degree and upperband number

$$\zeta_{\psi}(F(t)) = 1 - \sum_M (p_M(t))^2, \quad \text{with } p_M(t) = \langle \psi(F(t)) | \hat{P}_M | \psi(F(t)) \rangle \quad (4.34)$$

$$M_{\psi}(F(t)) = \langle \psi(F(t)) | \sum_l \hat{n}_l^b | \psi(F(t)) \rangle, \quad (4.35)$$

4. Many-Body Wannier-Stark System: Dynamical Analysis

where the limits are given by $\zeta \rightarrow 1 - 1/N$ and $M \rightarrow N/2$.

At this point, we have enough methods to probe the spectral properties studied in the previous chapter. We shall see that the system can undergo relaxation towards equilibrium, which needs necessarily strong mixing, hence manifold balance. This latter concept was previously introduced in section 3.2.2 when discussing the conditions for maximal hybridization. The conditions for manifold balance are exactly the same as for the onset of chaos, i.e. $N/L \sim 1$, $W_x/2\Delta_g \sim 0.1$. In addition, strong manifold mixing implies a large occupation of the mid-manifolds $0 < M < N$, for which the upperband occupation number converge to $M \approx N/2$ and $\zeta \rightarrow 1 - 1/N$. Finally, when studying the ergodicity properties of the spectrum, we showed that, up to degeneracies, the system is expected to equilibrate about the GOE limits.

Now we want to study the relaxation dynamics, via quantum sweeps. Our results show that via chaotic resonant tunneling we create quantum states that have the same properties expected for an equilibrium state, i.e. those which satisfy *the principle of maximum entropy*. In our case, the Shannon entropy maximizes in the presence of chaos with with maximal value given by $S_{\text{sh}}^{\text{gue}}$. Let us now investigate the RET regime, which can done in different ways:

- (1) **Local sweeps:** here the system is prepared in different initial conditions and then swept across the local resonant regime, i.e. around the resonant position F_r within the interval $F \in [F_r - \Delta F/2, F_r + \Delta F/2]$.
- (2) **Global sweeps:** starting initially from the flat lattice condition, different initial conditions are evolved across the entire spectra. Here, the system must cross the whole set of resonances F_r non-adiabatically.
- (3) One can set our sweeping function $F(t)$ at will. In the first two steps for simplicity we always consider the sweep function $F(t) = \alpha t + F_0$.

In the rest of this chapter we study the two first scenarios, which might be of particular interest for experimental realizations. Yet, the local sweeps are more practical since they allow us to study a particular domain of the many-body spectrum. In this case, whenever the spectrum is fully mixed, the character of the eigenstates is not even close to the seed states before F_r . Therefore to speak about generic initial condition does not make sense at all. Nevertheless, by sudden quench, one can easily prepared the initial state in the flat lattice, and then drive it across the resonance. Such a kind of states undergo fast mixing. The second method has an enhanced complexity since the evolved states start mixing very early across the entire spectrum. This naturally implies that the outcoming state is expected to be fully hybridized. However, we shall see that in absence of (weakly) global mixing the system preserves partially the spectral localization features at final time, whose signature is the manifold formation. In the following, we compare the results of the two first types of sweeps and the last one is left to future works.

4.3.1 Local Sweeps

To study the system locally around one resonance position, we use a simple protocol. Let us choose the many-body avoided crossing in the vicinity of the resonance F_r , i.e. $F \in [F_r - \Delta F/2, F_r + \Delta F/2]$. Here ΔF is defined by

$$\Delta F = F_f - F_0 = \frac{\Delta_g}{2\pi} \left(\frac{1}{\mu_-} - \frac{1}{\mu_+} \right), \quad \text{with } \mu_- = 0.75, \mu_+ = 1.25, \quad (4.36)$$

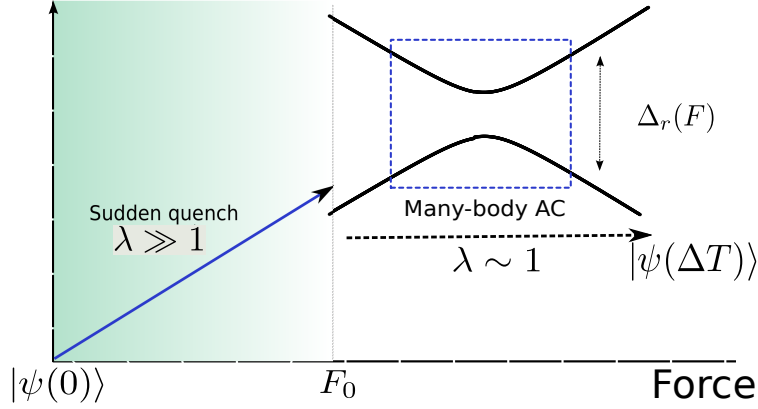


Figure 4.7: Sketch of the local sweep process. λ is the parameter that controls the type of dynamics (see Sec. 4.1). This process is done in two instances: first, the system is prepared in a Fock (seed) state at $F = 0$, i.e. the flat lattice. A sudden quench ($\lambda \gg 1$) is applied to quench the system from $F(0) = 0 \rightarrow F(T_0) = F_0$. Secondly the starting from F_0 , the system is evolved across the many-body AC non-adiabatically ($\lambda \sim 1$) during a time $\Delta T_k = T_k - T_0$, with $T_k \in [T_0, T_f]$ and $\Delta T = T_f - T_0$.

where μ_- and μ_+ are fixed here, but they can be obtained using Eq. (3.60). The width ΔE of the many-body AC is given by

$$\Delta E \simeq \frac{1}{\mathcal{N}_s} [N\Delta_r(F_r) + 0.5W_b N(N-1)], \quad (4.37)$$

and therefore according to Eq. (4.3), the value of the sweeping rate is given by $\alpha = \lambda \cdot \Delta E(F_r) \cdot \Delta F$. By fixing this spectral domain, one can sweep any initial condition starting from $F = 0$, i.e. the flat lattice, to a tilt $F_0 < F_r$, through a sudden quench ($\lambda \gg 1$). This process does not modify considerably the characteristics of the state when passing by resonances of higher order. The reason lies on the fact that, in order to see significant changes in the state, the sweeping rate must be defined respect to the properties of the local resonance. It means, if we fix our spectral domain to be the vicinity of F_r , whose $\Delta_r(F)$ is given by Eq. (4.37), the value of the sweeping rate for higher orders of resonance is smaller compared to the local one, i.e. $\alpha(F_r) > \alpha(F_{r+1})$. The latter relation implies that by sudden sweep the system remains unchanged after crossing the F_{r+1} , F_{r+2} and so on. In this manner, before F_r the dynamics is nearly diabatic. We leave for the next section the discussion about the effects that the initial state undergoes when crossing non-adiabatically the entire spectrum.

To visualize the transit across a resonance, we use the LDOS $P_\psi(\varepsilon, t)$ defined in Eq. (4.23). We can choose the initial state according to its manifold number $M_i = \langle \varepsilon_i | \sum_l \hat{n}_l^b | \varepsilon_i \rangle$. Typically, $|\langle s_\beta | \varepsilon_i \rangle|^2 \gtrsim 0.8$ in case of weak mixing (see Fig. 4.6). The spectral navigation with this initial state is numerically computed by solving the Schrödinger equation as explained in the section 4.3.

Then the LDOS function can be constructed through the projections of the instantaneous state $|\psi(t = T_k)\rangle$ with the local eigenstates $\{|\varepsilon_i(F = F_k)\rangle\}$, $F_k \in [F_0, F_f]$, i.e. the coefficients $C_i(t_k) \equiv \langle \varepsilon_i(F_k) | \psi(t = T_k) \rangle$. The whole evolution process is sketched in Fig. 4.7.

The transit of the instantaneous state $|\psi(t)\rangle$ is shown in Fig. 4.8, for two different systems $N/L = 5/4$ and $N/L = 6/3$, and for the three different types of dynamics: $\lambda \ll 1$ (left panels), $\lambda = 1$ (central panels), $\lambda \gg 1$ (right panels). Note, that the sudden sweep tends to preserve the state $|\psi(t)\rangle$ well localized in the spectrum before and after the sea of ACs, centered at the $\frac{\Delta_g}{2\pi F(t)} = 1$.

In the manifold language, if the LDOS emerges well localized from the many-body AC and parallel to the incoming one, it means that the manifold number is preserved after the passage.

4. Many-Body Wannier-Stark System: Dynamical Analysis

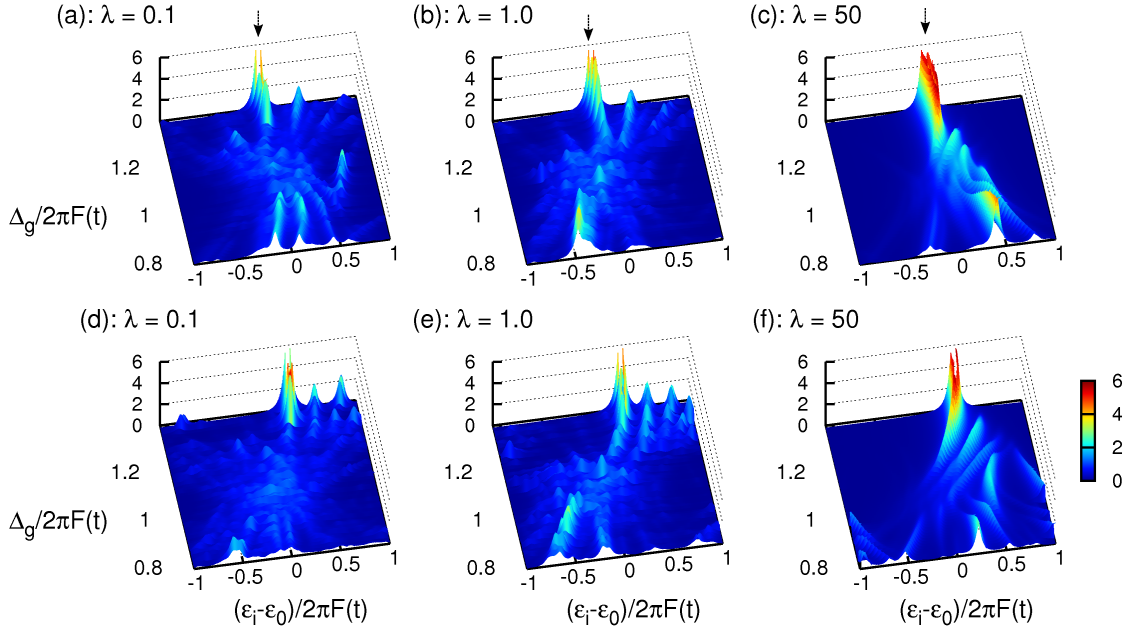


Figure 4.8: Evolution of the local density of states $P_\psi(\varepsilon, t)$ for the system: (a,b,c) $N/L = 5/4$ and (d,e,f) $N/L = 6/3$. The initial condition is the eigenstate $|\varepsilon_i\rangle$ at F_0 , whose manifold number corresponds to $M \approx 2$ for both systems. The parameters are $V_0 = 5$, $s_0 = 2.5$ with $\Delta_g = 0.8$, and $W_x/2\Delta_g = 0.027$. Both systems spectra present deviations from the regularity, but they are not fully chaotic (see sec. 3.2.3). Each panel shows the three different time regimes: adiabatic $\lambda = 0.1$, non-adiabatic $\lambda = 1.0$ and diabatic $\lambda = 50$.

This is exactly what we have called localization in the spectrum. Yet, this is not the only way to see such a localization. As seen in the central panels of the figure 4.8, the outgoing state may emerge with a different slope but well localized. Such a process clearly does not preserve the manifold number and change the properties of the instantaneous state. That is, the system undergoes an exchange of character across the AC. When sweeping adiabatically across the RET domain, several processes, principally diffusion, take place. This brings the system to become delocalized in both basis, the local one $|\varepsilon_i\rangle$ and also in the unperturbed one, i.e. the seed basis. This effect destroys completely the initial state and the outgoing one has large contributions of many seed states, hence from all M -manifolds.

An engineering of the dynamics across the RET domain does not rely only on the latter concepts of localization (delocalization and further mixing) but also on the properties of the spectrum. This means, if whether the cluster of ACs follows quantum chaotic statistics or nearly ones.

After the quench, the initial state may drastically change (see in Fig. 4.9). There, we evolve an initial state across the corresponding spectra of systems with filling factors $N/L = 5/6$ and $N/L = 6/5$. For those, it is already seen that around the resonance the respective NNLS distributions are GOE-distributed in the case $N/L = 6/5$ and present deviations to the regularity for $N/L = 5/6$ for smaller gaps (see Fig. 3.16).

We have seen in chapter 3 that the size of the sea of ACs depends sensitively on the value of the gap Δ_g and filling factors (see Figs. 3.8 and 3.14). We can see that for $s_0 = 2.5$ ($\Delta_g = 0.8$) the instantaneous state remains practically localized across the resonance in comparison with its passage across the spectrum of $s_0 = 4$ ($\Delta_g = 0.285$). The same effect can be seen by com-

4.3. Spectral Diffusion in the Many-body Interacting Regime

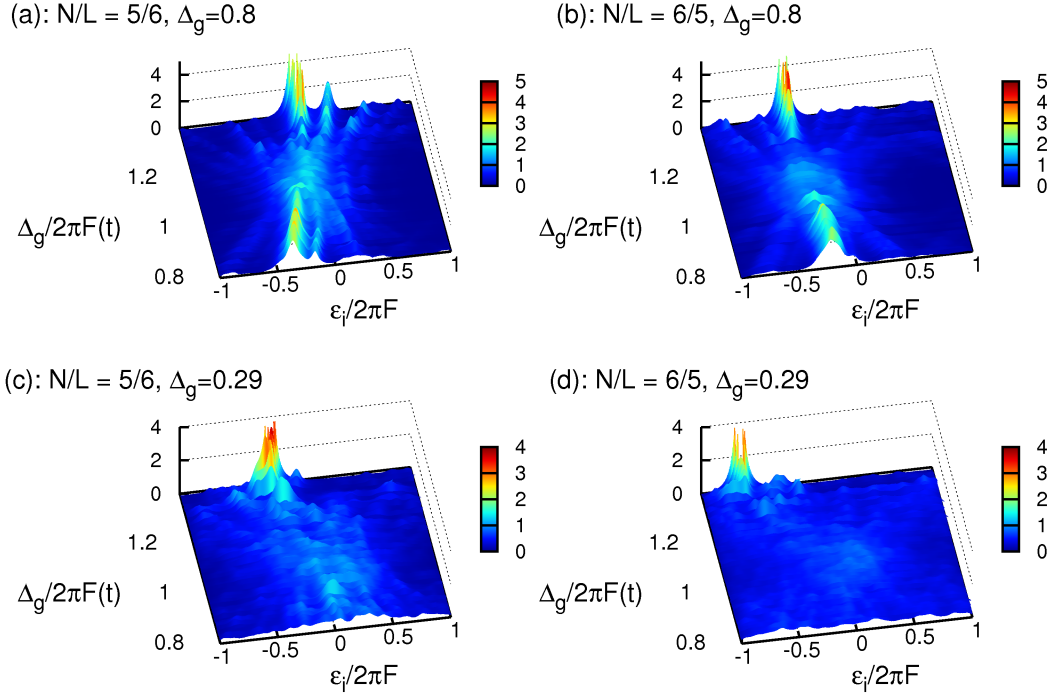


Figure 4.9: Evolution of the local density of states $P_\psi(\varepsilon, t)$ for $V_0 = 5$ and the systems: (a,b) $N/L = 5/6, 6/5$ with $s_0 = 2.5$ and (c,d) with $s_0 = 4$. $\lambda = 1$, i.e. non-adiabatic passage is considered. The initial condition is the eigenstate $|\varepsilon_i\rangle$, whose manifold number corresponds to $M \approx [N/2]$ for both systems. Both system spectra around the F_r follows quantum chaotic NNLS distribution. (a,b) show the evolution of a region with small ACs size and for (c,d) is larger.

paring the evolution for $N/L > 1$ and $N/L < 1$. For $N/L = 6/5$, we can observe the spreading of the instantaneous state $|\psi(t)\rangle$ at $\Delta_g/2\pi F(t) \sim 1$. The instantaneous LDOS becomes uniformly distributed over the entire FZ, which implies that coefficients C_i 's fluctuate about the equipartition condition $|C_i(t)|^2 \approx 1/\mathcal{N}_s$. The latter happens the strongest, the more chaotic the spectra is, and no further localization is seen. In the case $N/L = 5/6$ (Fig. 4.9(c)) the respective spectrum presents deviations from the GOE. One can see that the LDOS at final time is not fully spread over the FZ. This is one first difference when sweeping across RET domains with different statistical energy spectra.

To quantify the difference mentioned in the previous paragraph, we can use the delocalization measures from Eq. (4.27). The results are shown in figure 4.10. One clearly notice that the delocalization is sensitive to the filling factor. For instance, in the case $s_0 = 2.5$ there is no complete delocalization of the instantaneous state $|\psi(t)\rangle$, but more than 50% of its initial properties (for example M) are lost around $\Delta_g/2\pi F(t) \sim 1$. As an immediate consequence, the outcoming state starts relocalizing (see Fig. 4.10-(a,b)). Yet, if the filling factor much less than one the relocalization effect is stronger. The horizontal lines correspond to the GUE limits given in Eqs. (4.33), whose values depend on the size of the Hilbert space. In the current case we have $\mathcal{N}_s(4/11) = 1150$, $\mathcal{N}_s(5/6) = 728$, $\mathcal{N}_s(6/5) = 1001$ and $\mathcal{N}_s(7/4) = 858$.

The other case ($s_0 = 4$) is shown in Fig. 4.10. The panels (c,d) show that in the case of fully chaotic spectra ($N/L = 6/5, 7/4$), the instantaneous state delocalizes completely after F_r . Conversely, for $N/L = 4/11$ and $N/L = 5/6$, one does not see full delocalization. Other way to see such a deviations consists in studying the distribution of the coefficients $\{C_i\}$ at final time, because they give us information of how delocalized the final state $|\psi(\Delta T)\rangle$ is.

4. Many-Body Wannier-Stark System: Dynamical Analysis

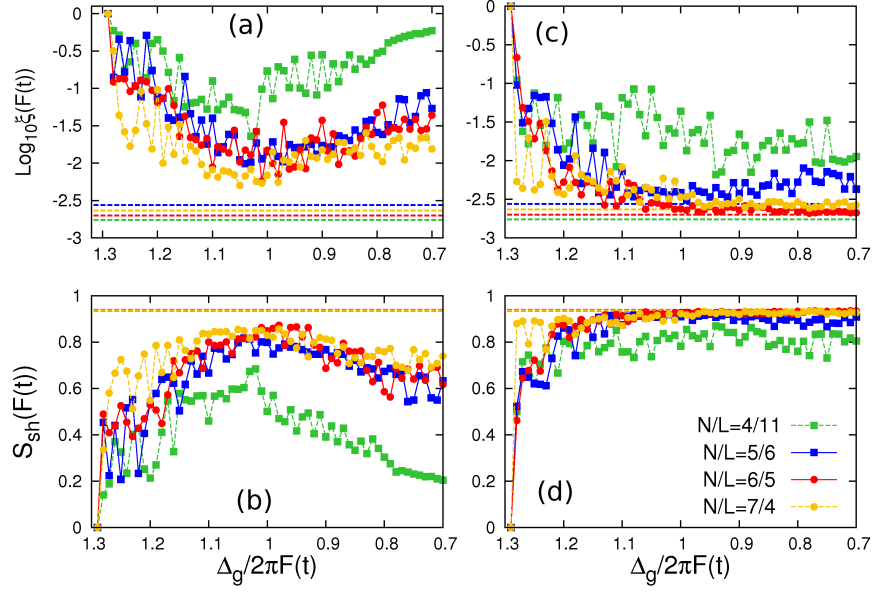


Figure 4.10: Delocalization measures for the non-adiabatic dynamics $\lambda = 1$ for the systems $N/L = 4/11, 5/6, 6/5$ and $7/4$. The horizontal lines represent the corresponding GUE limit. (a,b) for $s_0 = 2.5$ ($\Delta_g = 0.8$), and (c,d) for $s_0 = 4$ ($\Delta_g = 0.285$). The initial states are taken from the manifold $M = [N/2]$.

We compare the numerically computed distribution $P(y)$ with the RMT prediction $P_{PT}(y) = \exp(-y)$ in Fig. 4.11, with $y = |C_i|^2 / \langle c^2 \rangle$. Here $\langle c^2 \rangle$ stands for the mean detection (occupation) probability. By simple view, it is possible to recognize the deviation for filling factors smaller than one. In the case $N/L > 1$ the histograms fit much better to the theoretical Porter-Thomas distribution (dashed-red line). We then conclude that full delocalization around the resonance of order one is always expected for filling factor larger than one, and partial delocalization with plausible relocalization for the not fully chaotic case. At this point, it is worth pointing out that the relocalization effect does not imply a partial recovery of the information of the initial state properties, but it certainly tells us about the exchanging character of the evolved state in the long-time process. If any relocalization takes place, as in the chaotic case, the delocalization measures have to decay faster across the RET domain. To study the decay of the inverse participation ratio, it is convenient to define the time-averaged function

$$\text{Time-averaged } h(t) = \frac{1}{\Delta T_k} \sum_{t_k=T_0}^{\Delta T_k} h(t_k), \quad (4.38)$$

which decays smoother than the original one $h(t)$. ΔT_k is defined as the time expended to sweep from $F_0 \rightarrow F_k$, with $F_k \in [F_0, F_f]$ (see Fig. 4.7). By defining $h(t) = \xi(t)$ or $h(t) = 1 - S_{sh}(t)$, one can study its long-time decay.

Figure 4.12 shows the decay of the time-averaged inverse participation ratio $\xi(F(t))$. Note that in both cases, $s_0 = 2.5$ and $s_0 = 4$, there exists an algebraic (power law) decay $t^{-\nu}$ with exponent $0.6 < \nu < 0.8$. This surprising result takes place right after the position of the local single particle resonance $\Delta_g/2\pi F_r = 1$. In the case $s_0 = 2.5$, none system presents full decay. The latter is expected since for larger gaps the spectrum is not fully quantum chaotic. This can be appreciated in the long-time limit where the decay is no longer a power law. This implies the relocalization phenomenon takes place, and we can have whether character exchanging or the recovery of the initial state properties. Yet, for $s_0 = 4$ the decay for long times is always power law

4.3. Spectral Diffusion in the Many-body Interacting Regime

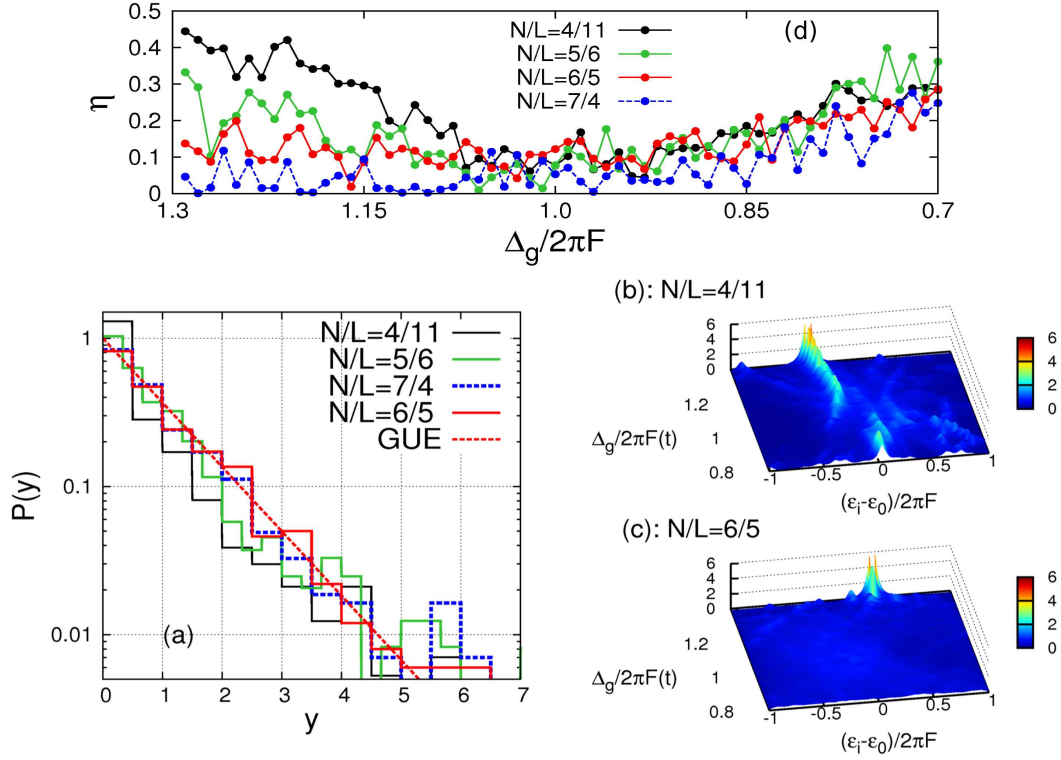


Figure 4.11: (a) Comparison of the theoretical Porter-Thomas distribution with the numerically computed histogram of the normalized coefficient $\{|C_i|^2\}$ at final time. Panels (b) and (c) show examples of the evolution for initial state lying on the mid-manifold $M = [N/2]$. Note that the spectral navigation is sensitive to the extension of the sea of ACs, which is the smaller the smaller the filling factor as clearly shown in panel (d), where η is the chaos quantifier defined in Eq. 3.81.

and therefore there is total loss of memory of the initial state properties, since any relocation take place, even if the spectrum start deviating from the quantum chaotic regime as shown in the panel (d) in Fig. 4.10.

In order to study the loss of memory of the initial state properties, let us define survival probability or the autocorrelation function

$$P_{\text{su}}(t) = \langle |\langle \psi(0) | \hat{U}_t | \psi(0) \rangle|^2 \rangle_{\psi}. \quad (4.39)$$

The average is taken over the entire set of initial conditions $\{|\psi(0)\rangle\}$ defined by all eigenstates $|\epsilon_i(F_0)\rangle$, with manifold number $M \approx [N/2]$. As the evolution starts, the survival probability collapses but also some revivals can be seen before F_r . This occurs due to the intra-manifold transitions essentially induced by the hopping terms (see 3.2). In the course of the evolution, when the inter-manifold mixing appears, $P_{\text{su}}(t)$ delocalizes and the system starts to loose the memory of its initial properties. This effect is enhanced across the sea of ACs. In the case of fully chaotic RET domain, no revivals are observed when studying the behavior of the time-averaged $P_{\text{su}}(t)$:

$$\text{Time - averaged } P_{\text{su}}(t) = \frac{1}{\Delta T_k} \sum_{t=0}^{\Delta T_k} P_{\text{surv}}(t). \quad (4.40)$$

The decaying in time of this function is shown in Fig. 4.13 for $s_0 = 4$. Note that for all systems the decay follows a power law in the long-time. This is a signature of loss of memory

4. Many-Body Wannier-Stark System: Dynamical Analysis

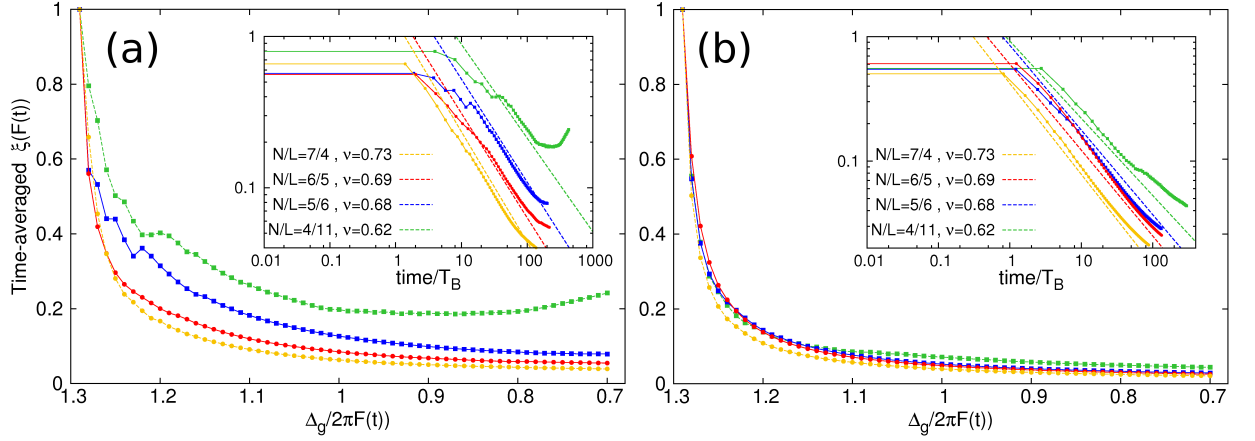


Figure 4.12: Long-time decay of the inverse participation ratio ξ for the non-adiabatic dynamics $\lambda = 1$. The panel (a) shows the time-averaged $\xi(t)$, for $s_0 = 2.5$, with the set of initial conditions lying in the manifold $M = [N/2]$. The systems are defined by the filling factors $N/L = 4/11, 5/6, 6/5$ and $7/4$. The inset shows the log-log plot of the main panel, where the straight lines represent the fittings to the power law function $t^{-\nu}$. The respective exponents are shown in the legend. In panel (b) shows the same as in panel (a) but for $s_0 = 4$. In this case the straight lines do not represent the fitting but show that the exponents are nearly the same, which implies a sort of universality when crossing the RET domain.

of the initial state and the system undergoes the predicted relaxation towards equilibrium with exponents $\nu \approx 0.7$. Therefore, we see that chaos apart of generating strong band mixing, it also induces fast decay of the localization measures to the equilibrium values set by the GUE limits (see Eq. (4.27)). Yet, in Fig. 4.13 one can also notice that the system loses its memory the slower, the smaller the filling factor is. In our case, the equilibrium was defined in the same way context of the energy shell approach reported in ref. [110, 111]. However, the connection is not straight forward, since in our case the distribution of coefficients C_i as a function of the energies within the Floquet zone is nearly flat function, with the same period of the Floquet eigenenergies. Therefore, the LDOS is an extended function over the entire spectrum. In the energy shell approach, the distribution of the coefficients has a gaussian profile presented, but it is not periodic [110]. To solve such a discrepancy, one must do an unfolding of the distribution in the Floquet energy space, or equivalently one can fold the gaussian profile. The latter method is straight forward since the function resulting after folding of a gaussian function is well-known as the *normal wrapped distribution* [114], which is a periodic function in the energy domain, it means, in the Floquet energy space.

As expected, there exists dependence on the sort of initial state evolved, i.e. the manifold character of the state. For local sweeps, the system relaxes faster if the set of initial states is taken from the mid-manifold $M \approx N/2$. The reason lies on the fact that in the center of the spectrum the number AC clustering is enhanced, especially, by effects of the diagonal inter-manifold coupling induced by the interaction term $2W_x \sum_i \hat{n}_i^a n_i^b$ and by the two-particle exchange (sec. 3.2.3). This effect is shown in Fig. 4.14 for the system defined by the filling factors $N/L = 5/6, 6/5$. The initial states are taken from the lowest manifold $M = 0, 1$ and from $M = 0, 2$ respectively. It is seen that the instantaneous state does not delocalizes completely for $s_0 = 2.5$ (upper panels), but it loses memory across the RET domain. This effect is possible through the exchange of character despite the incomplete spreading over the FZ. The system

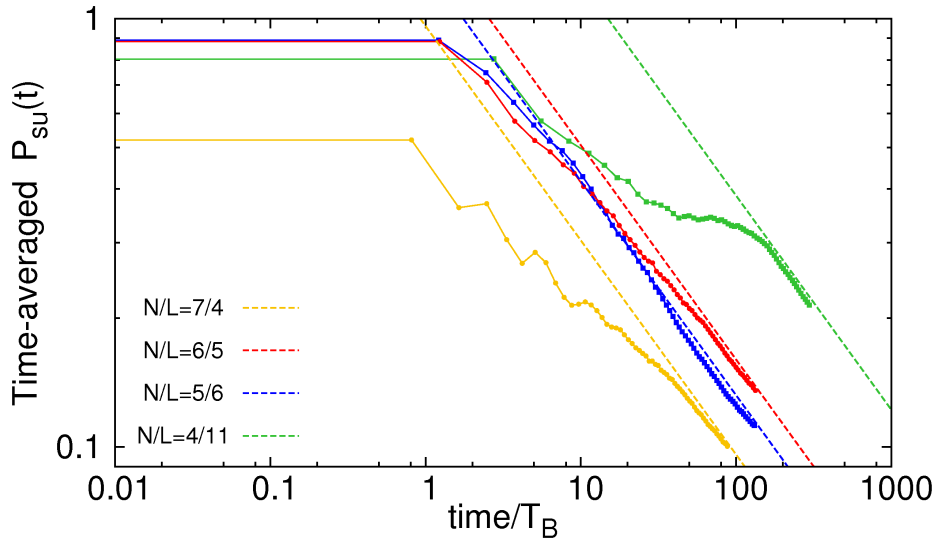


Figure 4.13: Decay of the time-averaged survival probability for the non-adiabatic dynamic ($\lambda = 1$). log-log scale for a set of initial conditions lying in the manifold $M = [N/2]$, for the systems $N/L = 4/11, 5/6, 6/5$ and $7/4$. The straight lines show the power law decay $t^{-\nu}$ for the long-time after the single particle position F_r . In most of the cases studied until now the coefficients $\nu \in [0.5, 0.8]$.

tends to equilibrate across the resonant regime but the relocalization effect appears. We have already shown that re-localization can take place in the memory loss of the initial properties scenario. The situation for $s_0 = 4$ is different. Here, despite the incomplete delocalization, in the long-time behavior the system undergoes a partial equilibration whose is above the full statistical equilibrium condition. Note that for these low-lying manifold state, the decay of the autocorrelation function follow a power law $\sim t^{-1/2}$, which is expected for diffusive transit across the RET regime. Such a behavior was already seen the previous chapter in Fig. 3.13, when studying the manifold-averaged inverse participation ratio.

The results in this section show that our system undergoes the already predicted equilibrium, when it is driven locally across the energy spectrum. Towards the possible experimental realization, one can implement a simple protocol consisting in the following of two steps:

- The system is prepared in any feasible initial state $|\psi(t)\rangle$ at $F = 0$. A sudden sweep ($\alpha \gg 1$) is applied to bring the system until the proximity of the chosen RET domain. This dynamical procedure is diabatic, which implies a preservation of the initial state with high fidelity, due to the spectra localization.
- Now the system is evolved non-adiabatically across the resonant regime, with $\alpha(\lambda \sim 1)$ defined as in the beginning of this section. At final time we can read out the properties of the evolved system, which contains very precise information of the class of spectral statistics followed by the local set of energies, i.e. those studied in the first part (see sec. 3.2). Furthermore, it is possible to predict relaxation properties, e.g. the power law or scale-free decay expected for the transit across a chaotic sea of ACs. In our case, across the many-body avoided crossing.

As final remarks of this section, we highlight the equilibrium reached for the system, essentially when the initial states belong to the mid-manifolds. In general, states with particles

4. Many-Body Wannier-Stark System: Dynamical Analysis

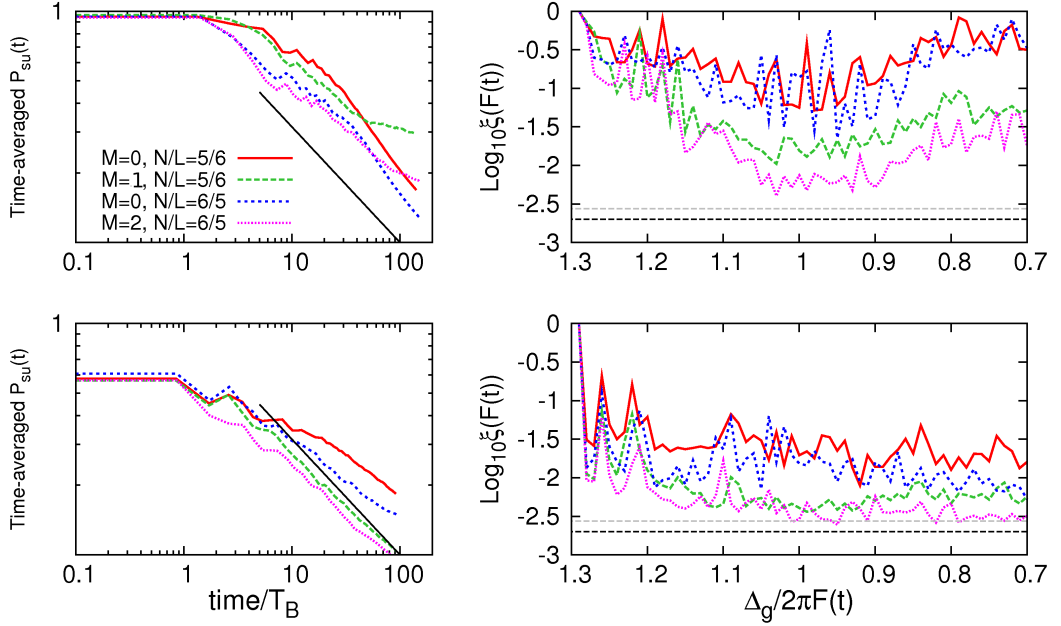


Figure 4.14: Survival probability and delocalization measures for different sets on the initial conditions. (a) Relaxation across the RET regime for the states initially prepared in $M = 0, 2$, for $s_0 = 2.5$ ($\Delta_g = 0.8$) and $N/L = 5/6, 6/5$. The black line corresponds to the power law decay const/\sqrt{t} . (b) The same information as in (a) but for smaller gap $s_0 = 4$ ($\Delta_g = 0.285$). Note that in any of these cases considered full delocalization does not happens, but the system undergoes in some cases fast decay of the survival probability in the long-time domain.

in both Bloch bands are non-equilibrium systems, which delocalize faster through the many Landau-Zener events. Nevertheless, in most of the set of initial states studied in this chapter, partial equilibration always occurs for initial conditions from low-lying manifolds. With this analysis, we have shown that the equilibrium is reached independent of the basis, i.e. when the coefficients A_v and C_i are equivalent, but only possible in the chaotic case.

4.3.2 Global Sweeps

In the previous section we have dealt with the local evolution across the spectrum. We now want to study the whole process by evolving many different initial conditions starting from the flat lattice $F = 0$. The motivation of this section is to see how relevant are the changes due to the evolution across the entire spectrum, by using the properties of a local AC many-body around the first order resonance, i.e. $\Delta_{r=1}$. In this context, the system is non-adiabatically evolved across the entire spectrum with sweeping rate $\lambda = 1$. The initial states to evolve are the seed states, which are the nearly the eigenstates of the Hamiltonian (3.1) with $F = 0$ for our parameter choices (see discussion in Sec. 3.2.2). We choose those seed states from the manifolds $M = 0$ and $M = [N/2]$, with the lattice parameters $V_0 = 5$, $s_0 = 3$ and $s_0 = 5$. Under the first condition ($s_0 = 3$), the energy spectrum presents local strong band mixing around the resonant regimes. Between order of resonances, the degree of manifold mixing is weaker and the instantaneous state preserves its manifold number with high probability. In the second scenario, we have already seen that the entire spectrum is strongly mixed overall. We are interested in the two next dynamical aspects:

- Long-time relaxation processes generated by the navigation across the entire spectrum.

4.3. Spectral Diffusion in the Many-body Interacting Regime

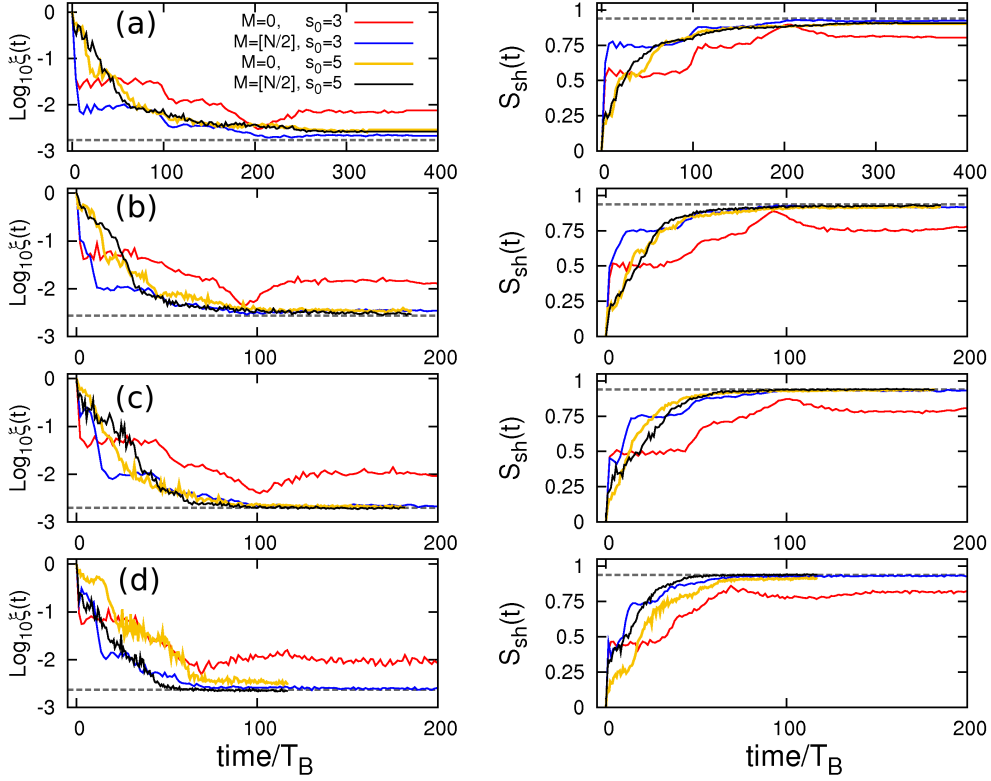


Figure 4.15: Delocalization across the entire spectrum for different filling factor with initial states prepared in the manifold $M = 0, [N/2]$. The results shown were obtained for $s_0 = 3$ and $s_0 = 5$, with $V_0 = 5$. (a,b) Delocalization measures for $N/L = 4/11$, (c,d) for $N/L = 5/6$. (e,f) for $N/L = 6/5$ and (g,h) for $N/L = 7/4$. The dashed line represent the GUE limit for the delocalization measures.

- Final time effects for manifold occupation number, mixing and delocalization. We set the sweeping rate as explained in the last section, i.e. using the properties of the RET domain at the first order of resonance: $\alpha(F_{r=1}) = \Delta E(F_{r=1})\Delta F$. This analysis is done by studying the coefficients $\{A_\nu\}$, i.e. we study the delocalization in the seed basis. In the chaotic case the information obtained from the latter coefficients is equivalent to the analysis done by using the projections onto the local spectrum. Yet, due to the localization properties of the spectrum and the M -quasisymmetry of the Floquet spectrum, we do not expect crucial differences at final time when we use A_ν or C_i . When deviations from chaos case appear, conservation of the certain manifold properties is clearly understood as spectral (re)localization. We summarize our findings in the following figures.

Starting with the figure 4.15, we see similarities in the time behavior of the delocalization measures compared to the findings in the previous section. The plot shows the evolution for the systems: (a,b) $N/L = 4/11$, (c,d) $N/L = 5/6$, (e,f) $N/L = 6/5$ and (g,h) $N/L = 7/4$. We find:

- *Case $s_0 = 3$* : There is no full relaxation for initial states living in the manifold $M = 0$. Nevertheless, the system equilibrates the GUE limits. The latter occurs due to the deviation from the fully chaotic regime. Conversely, for initial states with $M = [N/2]$, full delocalization is always seen in the long-time behavior after the passage across the first order resonance. Such a full delocalization is expected because the instantaneous state starts hybridizing before crossing the local RET domain. This occurs in two instances: a first

4. Many-Body Wannier-Stark System: Dynamical Analysis

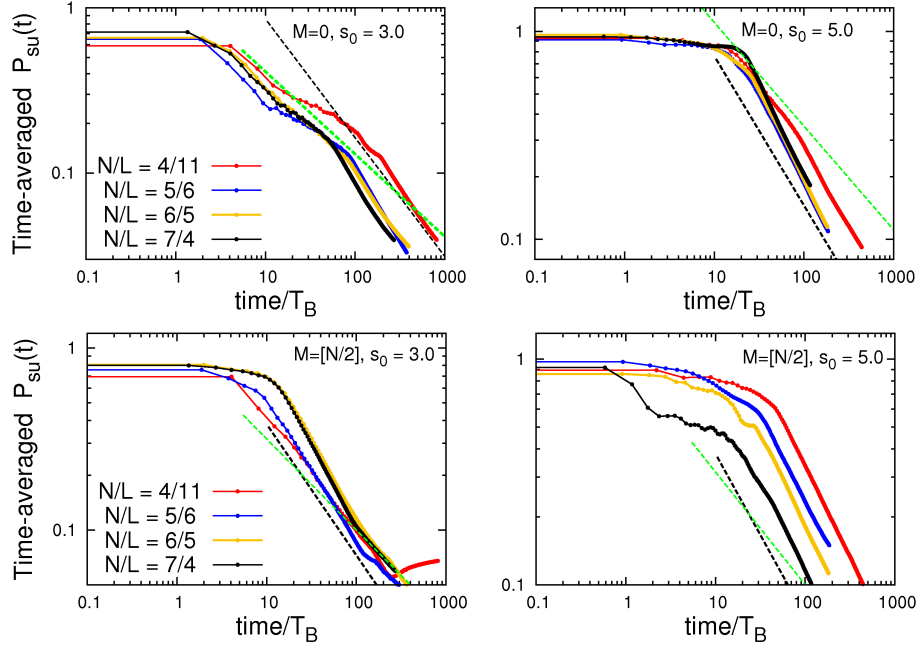


Figure 4.16: Time-averaged survival probability in log-log plot. (left) for $s_0 = 3$ and (right) $s_0 = 5$. This figures show the difference in the relaxation process for the cases exposed in the main text. Note that still in the single-particle limit the system takes longer to relax compared with the systems with a filling factor close to one.

equilibration occurs before the fourth resonance order. Then a further relaxation process takes place. Note that the larger the filling factor, the smaller the range of time for the first equilibration process. This effect has its origin in the spectral (manifold) localization, since the one-particle exchange energy increases as a function of the Stark force. Therefore, for the first order resonances, the sweeping rate $\alpha(F_r)$ becomes comparable to the sweeping rates of $r = 1, 2$, and 3 . The inter-manifold coupling is enhanced, hence also the delocalization. Additionally, we can see that complete relaxation takes place in a time scale of hundred Bloch periods ($F_r \in [0.01 : 0.5]$), which may be good for experimental realizations.

- Case $s_0 = 5$: For this case, equilibrium is reached faster, especially for filling factors close to one, and there are no longer first equilibration processes. Note that in the transit to the equilibrium the inverse participation ratio decays exponentially in a first instance up until its maximal value for delocalization. At final time, any relocalization process is seen for this set of lattice parameter.

The relaxation towards equilibrium depends on the filling factor. This is shown in Fig. 4.16, where the time-averaged survival probability is plotted as a function of time, for the different filling factors. Note that in case $s_0 = 3$ (Fig. 4.16(left panels)) the system loses its memory of the initial state properties and any revivals were seen for the systems studied in this section. This effect was already seen in figure 4.16, where the system does not delocalize completely but it equilibrates in the long-time evolution.

As final result, we compute the different measures used in this chapter at final time, i.e. the manifold mixing degree $\zeta_i(\Delta T)$ and the number $M(\Delta T)$, the participation ratio $\xi(\Delta T)$ and the Shannon entropy $S(\Delta T)$, respectively. The results are shown in Figs. 4.17 and 4.18. For this

4.3. Spectral Diffusion in the Many-body Interacting Regime

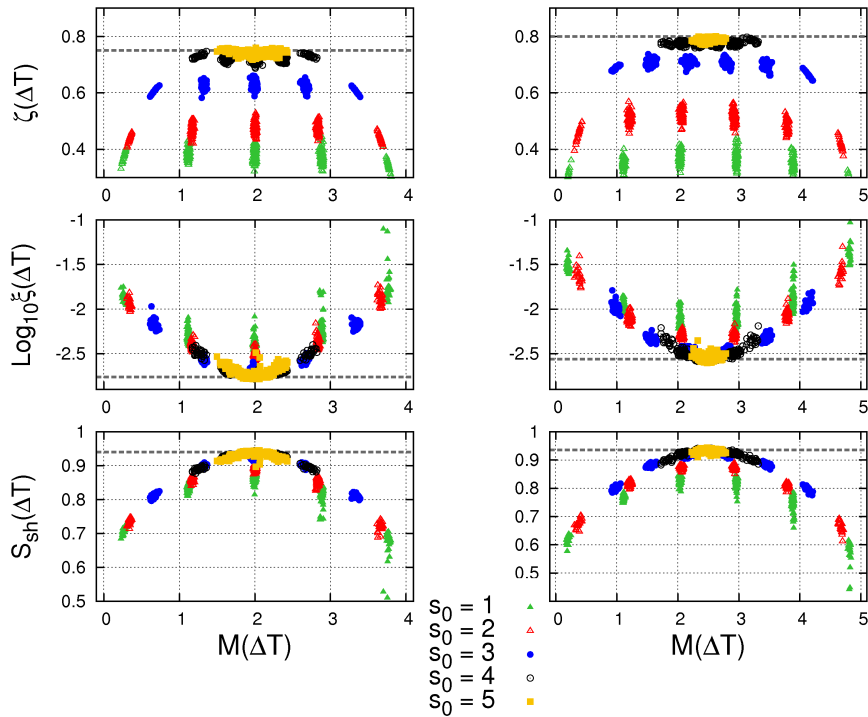


Figure 4.17: Final time relaxation measures or various lattice parameters s_0 , i.e. for different band gaps. (Right) the panels show all measures defined along this chapter to study diffusion and mixing, for the $N/L = 4/11$. The manifold formation for $s_0 \leq 3$ is represented by the bunches of states with manifold number M close to integers. The dashed lines represent the GUE limits for the delocalization measures and the upper bound values for the manifold mixing degree parameter. (Left) here we plotted the same quantities for $N/L = 5/6$.

calculation we have evolved more than 400 different initial conditions belonging to all possible sets of manifolds. We must keep in mind that the number of manifold is $N + 1$, where N is the total particle number. Taking the final time as a parameter, the figures show destruction of the manifolds as the gap decreases with a critical value $s_0 \sim 4$. Here one can no longer identify the separated bunches of states with closely well defined manifold number. The latter dynamical effects were already predicted in sec. 3.2. Note that independently of the class of initial state, for fully chaotic spectrum $s_0 = 5$, all final states are completely delocalized. Hence the equilibrium is ubiquitous in that regime of parameters. Some consequences of this final time behavior are still under study, for example, the resulting thermalization. We shall comment more precisely on this problem in the outlook of this thesis.

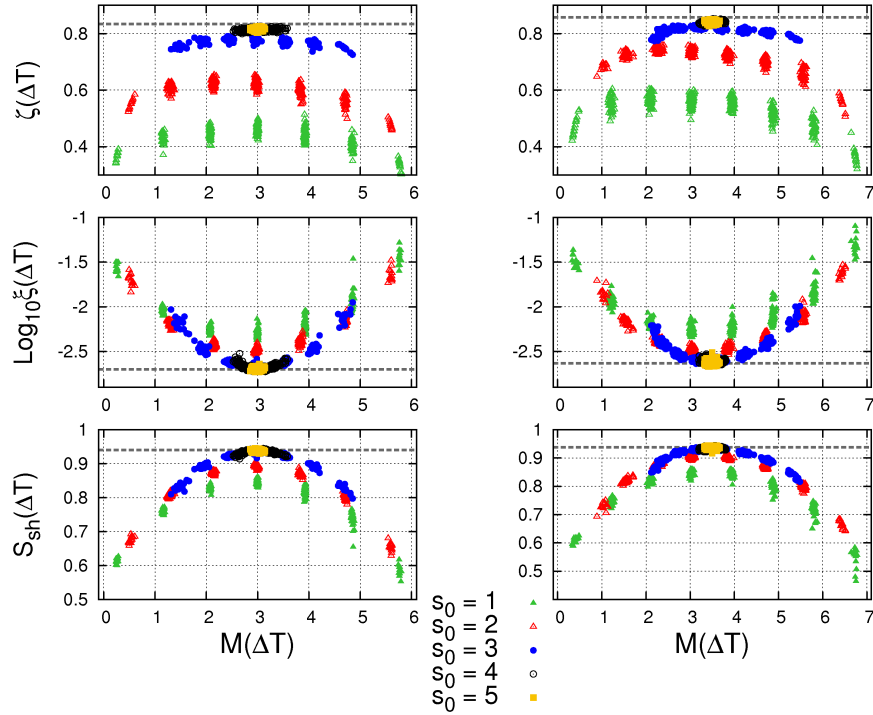


Figure 4.18: The same measures as in Fig. 4.17 for $N/L = 6/5, 7/4$.

4.4 Summary

Throughout this chapter, we have studied the dynamical properties of our many-body Wannier-Stark system by means of quantum sweeps of the Stark force. We presented two ways of studying the delocalization processes generated by the linear pulse $F(t)$, in analogy to the Landau-Zener problem, but in a many-body scenario. We have mostly numerically proven that:

- The system undergoes spectral ergodicity up to degeneracies and the strong mixing between the Bloch bands (represented by the manifold mixing) takes place. This is very important for the relaxation process.
- There exists a strong sensitivity of the delocalization and posterior equilibration on the statistical properties of the spectrum, here mainly induced by the decrease of the bandgap Δ_g , and also by changes of the filling factor. In the first case, the gap must be reduced to values comparable to the interparticle interaction, in order to obtain a fully quantum chaotic spectrum for any value of Stark force. Such a condition was referred to as *global mixing*. However, such a type of mixing can also be generated by increasing the filling factor and the interparticle interaction.
- We highlight that despite the complexity of our system, one can still read out useful information and predict about the underlying dynamics. For example, we have predicted the manifold formation across spectrum. The bunches of states with the same quantum number M manifest themselves by the localization properties of the evolved state $|\psi(t)\rangle$, whether in the final time results in Fig. 4.18, or before and right after the local resonant domain studied in the section 4.3.1.

- Finally the time scales for the occurrence of the different many-body effects studied in this chapter are small, which offers the possibility of experimental realization, for example of the maximally hybridized state or equilibrium state. This state very interesting, since after its preparation the system can be "trapped" in the spectrum by driving it until regions where the inter-manifold mixing is suppressed, i.e. in the off resonant regime. Apart from the fact that our model involves many different transition processes, we expect that the many-body effects presented in this chapter can be seen in a realistic implementation.

An Open Many-Body System: Decay-rate Analysis

In the previous chapter we have shown a detailed study of a closed system based on a two-band model for the many-body Wannier-Stark system. In this context, when a single-periodic potential is considered, one way to describe the system, taking into account decay, is by adding imaginary parts Γ_i to the diagonal of the Hamiltonian matrix. This transforms the unperturbed states into metastable ones [115]. An example of that method is reported in [75] for the single-band tilted Bose-Hubbard model. Therein, it is shown that the dissipation rates Γ_i can be well approximated by using perturbation theory under certain circumstances. Nowadays, there exist experiments, in which the dissipation processes can be manipulated (see ref. [27–29]) directly without an additional Stark force. In this chapter we study a non-hermitian effective single-band Bose-Hubbard Hamiltonian. We shall show that, by analyzing the quantum spectrum, useful information of the system, as state formation and their stability, can be extracted in the same way as already shown in the previous chapter. The direct access to the spectrum of the metastable many-body system allows us to easily identify relatively stable quantum states, corresponding to previously predicted solitonic many-body structures [31, 32].

5.1 Non-Hermitian Approach to a Noisy Bose-Hubbard Model

The microscopical behavior of a system coupled to its environment is certainly an important issue in quantum physics. It is a well established fact that, under this circumstances, the system will undergo changes, and in general it can no longer be represented in terms of unitary, Hamiltonian dynamics. To study an open quantum system, say, the system S plus its environment, there exist many successful approaches. Techniques based on the Master equation [116] are heavily used in quantum optics [117] to describe, for instance, loss and gain of photons, and dephasing mechanisms in micro- and nanocavities [118, 119]. Other methods are based on the theory of scattering (see refs. [120] for an overview).

Effective Hamiltonians containing absorbing boundary conditions [115] have shown themselves to be a very useful method to study the effect induced by the environment on the isolated system S . This latter approach has the advantage that it allows one to access a generalized quantum spectrum, thus it extends spectral methods as those applied to closed systems, to open ones. Keeping in mind that the method of effective non-hermitian Hamiltonians is based on perturbative arguments [75], such as a weak decay or coupling to the environment, it nevertheless gives the possibility to predict the evolution of the system for short times. The qualitative understanding based on the analysis of the spectrum is at least as useful as more

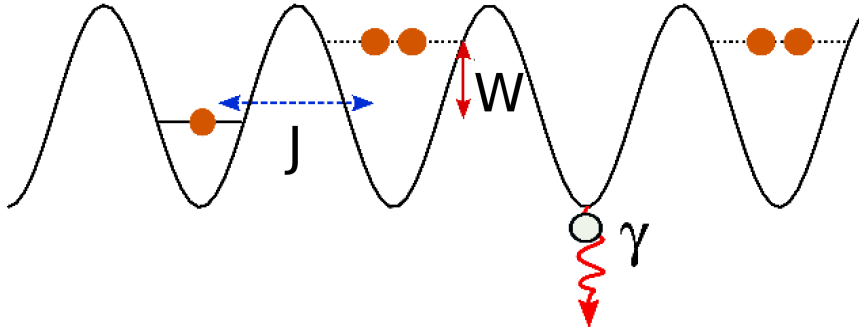


Figure 5.1: Sketch of a typical realization of strongly correlated many-body open quantum systems, including particle loss with decay rate γ in one of the potential wells, which can be experimentally engineered. J denotes the hopping term, i.e. transition strength for particle to jump between neighboring sites and W denotes on-site two-body interaction energy (see sec. 2.3 for more details). Interplay of the various processes can lead to interesting dynamics in the open many-body systems, as discussed in section 5.2.

accurate methods which are based on numerical propagation in most cases [121].

In contrast with the problem studied in Chapters 3 and 4, here we concentrate on systems of ultracold atoms loaded into single-periodic lattice structures. The optical potential is considered to be deep enough such that the single-band approximation described in sec 2.1.2 is valid. In more detail, we choose the ratio between the gaps Δ_1 and Δ_2 to be larger, which is easily implemented by setting $s_0 = 0$ and $V_0 > 10 E_R$. In addition, the external Stark force is disregarded, since our interest is to study the type of system investigated in ref. [27], but in one-dimension as sketched in Fig. 5.1. The system may be opened artificially to observe interesting effects induced by dissipation and/or quantum noise. This is investigated in the following section, by using an effective non-hermitian Hamiltonian for the many-body system. Experimentally, the loss of particles shown in figure 5.1 can be realized easily in a controlled manner. Single particle decay channels are provided by shining in appropriate laser beams [122] or even electronic beams [27–29]. The latter ionize single atoms in the condensate, which, together with the produced electrons, are afterwards accelerated by electric fields, hence they leave the system extremely fast without strong back-action to the remaining bosons in the lattice environment.

5.2 A Dissipative Bose-Hubbard System

In the single-band approximation, ultracold bosonic atoms at zero temperature can be described by the celebrated Bose-Hubbard Hamiltonian [12]

$$\hat{H} = \sum_{l=1}^L -J \left(\hat{a}_{l+1}^\dagger \hat{a}_l + h.c. \right) + \sum_{l=1}^L \frac{W}{2} \hat{n}_l (\hat{n}_l - 1), \quad (5.1)$$

provided the optical lattice holding them is sufficiently deep, such that the approximation by discrete modes denoted by the index l is good. Here \hat{a}_l and \hat{a}_l^\dagger are the bosonic annihilation and creation operators and we set \hbar to one measuring all energies in frequency units. This Hamiltonian can be made dimensionless by rescaling with one of the two energy scales J or W respectively. Hence, without loss of generality, we set $J = 1$ in the following, measuring all energies in units of J .

5. An Open Many-Body System: Decay-rate Analysis

As briefly mentioned in the introduction and motivated in a series of previous papers on dissipative Bose condensates [31, 32, 123–125], a tunable source of single-particle dissipation can be added to the system. With the spatially local dissipation rates γ_l , the dynamics is then best described by a quantum Master equation [116, 126] for the many-body density operator:

$$\dot{\hat{\rho}} = -i[\hat{H}, \hat{\rho}] - \frac{1}{2} \sum_l \gamma_l \left(\hat{a}_l^\dagger \hat{a}_l \hat{\rho} + \hat{\rho} \hat{a}_l^\dagger \hat{a}_l - 2\hat{a}_l \hat{\rho} \hat{a}_l^\dagger \right), \quad (5.2)$$

which can be equivalently written as

$$\dot{\hat{\rho}} = -i[\tilde{H}, \hat{\rho}] - \sum_l \gamma_l \left(\hat{\rho} \hat{a}_l^\dagger \hat{a}_l - \hat{a}_l \hat{\rho} \hat{a}_l^\dagger \right). \quad (5.3)$$

with

$$\tilde{H} = \hat{H} - \frac{i}{2} \sum_l \gamma_l \hat{a}_l^\dagger \hat{a}_l. \quad (5.4)$$

The Master equation can be numerically integrated by transforming it into a first order differential equation system for the reduced density matrix $\rho_S = \text{tr}_{\text{env}} \rho$, i.e.

$$\frac{d}{dt} \rho_S(t) = \mathcal{L} \rho_S(t), \quad (5.5)$$

usually called the Markovian quantum master equation. This representation is valid due to the existence of linear map \mathcal{L} , which allows one to write the evolution of $\rho_S(t)$ as

$$\rho_S(t) = \exp(\mathcal{L}t) \rho_S(0), \quad (5.6)$$

for time-independent Hamiltonians H . The generator \mathcal{L} of the quantum dynamical semigroup represents a super-operator, i.e. it transforms operators into operators.

Stochastic methods are also useful to solve (5.3). For instance, the quantum jump approach allows us to obtain the exact solution, by unravelling the Master equation [116]. Alternatively, it can be solved approximately by methods which take into account effects beyond the mean-field – see, e.g. [31, 32, 125], where results of both methods are shown and compared.

Here we will follow a different approach based on an effective Hamiltonian \tilde{H} in which the dissipative terms of equation (5.3) are included as complex absorbing potentials. In contrast to the above mentioned methods for solving the Master equation, this gives us access to the quantum spectrum of the non-hermitian Hamiltonian studied in the next subsection. Within this approximation, the real parts of the spectrum correspond to the energy levels – just as for any closed quantum system – and the imaginary parts describe the decay of the metastable eigenstates, i.e. their stability in the presence of losses [115].

5.2.1 A Spectral Approach

As a study case, we now look at a particular situation of three potential wells with relatively large filling factors, i.e. particles per site, of the order ten or larger. For this setup, reference [31] predicts the *dynamical* formation of very stable collective states of many bosons within a single well, despite strong atom losses. More precisely, we choose two types of decay along the sites:

- *Case* γ_{101} : $\gamma_1 = \gamma_3 = \gamma$ at the two boundary wells and $\gamma_2 = 0$ in the middle site.
- *Case* γ_{010} : $\gamma_1 = \gamma_3 = 0$ at the two boundary wells and $\gamma_2 = \gamma$ in the middle site.

For weak atomic interactions, i.e. for the limit $W \rightarrow 0$, all particles will be lost steadily as time evolves. This is just the situation for independent (almost) non-interacting particles. For strong interactions, i.e. $W > W_{\text{crit}}$, however, the particles at the leaky sites are quickly lost, while the remaining wells are protected against the decay. This may be expected by a simple mean-field argument, saying that the bosons cannot get rid of their high energy in the middle well by just gaining the energy $J = 1$ by hopping to the leaky sites. Then, $W_{\text{crit}} \bar{n} \gtrsim 2J$, which is the so-called self-trapping criterion where mean-field tunneling, is suppressed by the mentioned energetic argument [8,9]. \bar{n} is the filling factor of the corresponding well. The big surprise reported in [31,32] is yet that the surviving part of the initially prepared condensate is very coherent, implying that non-trivial many-body dynamics occurred during the formation of this very stable, so-called solitonic state. This strongly correlated state is well known for its stability with respect to decay [127], and we are going to use this property in order to identify such a state using our spectral analysis. Thus dissipation can be used to prepare almost pure condensed many-body states in the middle well [31,32].

Those solitonic states can be easily detected (without any time-propagation as done in [31,32]), by studying the spectrum of the following effective Hamiltonian

$$\tilde{H} = - \sum_{l=1}^3 \left(\hat{a}_{l+1}^\dagger \hat{a}_l + \hat{a}_l^\dagger \hat{a}_{l+1} - \frac{W}{2} \hat{a}_l^\dagger \hat{a}_l^\dagger \hat{a}_l \hat{a}_l + i \frac{\gamma_l}{2} \hat{n}_l \right), \quad (5.7)$$

with $\hat{n}_l = \hat{a}_l^\dagger \hat{a}_l$ being the number operator. In the framework of the quantum jump method, this effective Hamiltonian gives the continuous evolution between two quantum jumps (see [116], Chapter 6, pag. 307). Nevertheless, one can use it to identify and study the breather state, which is predicted as an attractively stable state of the evolution of the full open system.

We numerically diagonalize the Hamiltonian (5.7) by using the Fock basis, i.e. the Fock states $|\vec{n}\rangle = |n_1, n_2, n_3\rangle$, whose dimension is given by

$$\mathcal{N}_s = \frac{(N+L-1)!}{[N!(L-1)!]}, \quad (5.8)$$

where N is the total particle number and L is the number of lattice sites, here fixed to $L = 3$. The latter basis can be used to expand the respective eigenstates as

$$|E_k\rangle = \sum_{\alpha} C_{\alpha k} |n_1, n_2, n_3\rangle_{\alpha}, \quad (5.9)$$

where the coefficients $|C_{\alpha,k}|$ allow one to recognize the character or structure of stable states. The eigenvalues, which are complex numbers, can be separately studied by defining $\varepsilon_k = \text{Re}(E_k)$, and $\Gamma_k = -2\text{Im}(E_k)$. The time evolution of an initial state $|\psi(0)\rangle$ can be computed with help of complex eigenenergies and eigenstates of the Hamiltonian \tilde{H} , which reads

$$|\psi_t\rangle = \sum_k c_k e^{-iE_k t} |E_k\rangle = \sum_k c_k e^{-i\varepsilon_k t} e^{-\Gamma_k t/2} |E_k\rangle. \quad (5.10)$$

From this equation, one can easily notice that through the evolution the system initially prepared in $|\psi_0\rangle$ can be constrained to lie in a set of eigenstates with the smallest decay rates Γ_k 's. Without loss of generality this set can consist of only one eigenstate. This will depend on the difference between the minimal decay rate, here defined by Γ_1 , and the next one Γ_2 . If there exists more than one eigenstate with low decay rate comparable to Γ_1 the stability can be defined by an effective low decay $\bar{\Gamma}$ and the nearest largest one, where $\bar{\Gamma}$ is the average decay rate of the

5. An Open Many-Body System: Decay-rate Analysis

distribution in the vicinity Γ_1 . It will be shown later that the structure of the state with a low decay rate depends on the dissipation configuration, i.e. whether we use γ_{101} or γ_{010} , boundary conditions especially in the latter configuration, and other parameters. Likewise, the evolution in time of any observable \hat{O} is computed by

$$\langle \hat{O} \rangle_t = \frac{\langle \psi_t | \hat{O} | \psi_t \rangle}{\langle \psi_t | \psi_t \rangle} = \frac{\sum_{kk'} c_k c_{k'}^* e^{-i(\varepsilon_k - \varepsilon_{k'})t} e^{-(\Gamma_k + \Gamma_{k'})t/2} \langle E_k | \hat{O} | E_{k'} \rangle}{\sum_k |c_k|^2 e^{-\Gamma_k t}}, \quad (5.11)$$

which inherits the constraining on the evolution of the wave function. The complex energy spectrum can be computed by using standard diagonalization methods, as for instance, LAPACK subroutines or Lanczos algorithm B.2. In the rest of this chapter we discuss the results of the analysis for the characterization of the stable eigenstates.

Case γ_{101} : Solitonic States

Here, for simplicity, we use periodic boundary conditions for \tilde{H} , by identifying $\hat{a}_{L+1}^\dagger = \hat{a}_1^\dagger$. The results presented below qualitatively remain unchanged when using open (also called hard-wall) boundary conditions, since the decay affects both ends of the lattice in exactly the same way.

In order to see the effect of the dissipation on the system, we plot the decay rate as a function of γ for different values of the interaction strength W . Figure 5.2 shows the different processes taking place as the dissipation increases. It is possible to recognize that one eigenstate with the lowest decay rate separates from the rest and this effect is enhanced as the interparticle interaction increases. However this also occurs for $W = 0$ and $\gamma > 10$ (see panel (a) in Fig. 5.2). This is not a surprise since without interactions the particles behave as one with low energy, not enough to beat the dissipation rate and tunnel to the boundary wells. In this manner, the dissipation induces a screening which maintain the particle localized in the central well. This effect is usually referred to as *quantum Zeno effect* [128]. The states with largest decay rate form bunches of levels about $\log_{10} \Gamma_k \sim 1$. They are very leaky eigenstates, i.e. a large number of Fock states participate on the evolution, thus making it easy to remove all particles from the system. Conversely, the stable states in the configuration γ_{101} have as the highest contribution given by the state $|\phi\rangle \sim |0, N, 0\rangle$, which has been proven to be very stable [31].

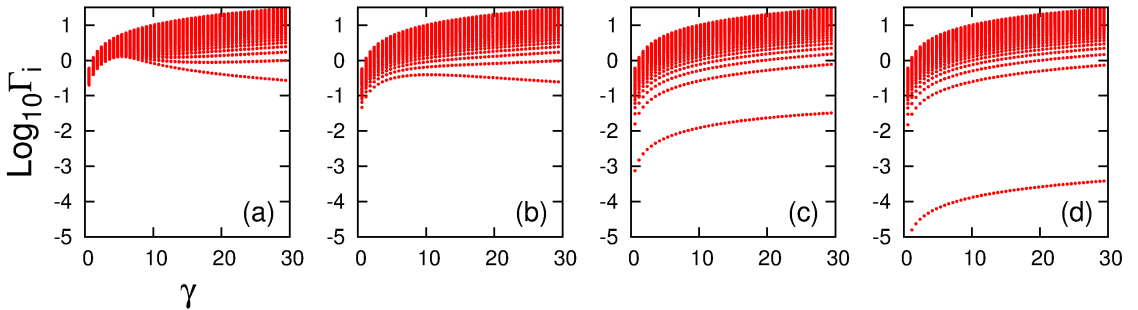


Figure 5.2: Log-plot of the decay rate as a function of γ , for $N = 40$ and interaction strength: (a) $W = 0$, (b) $W = 0.1$, (c) $W = 1$ and (d) $W = 10$. The figure shows clearly the separation of states with small decay rate, where the smallest one corresponds to the solitonic state $|E_k\rangle \sim |0, N, 0\rangle$ predicted by the time evolution in ref. [31].

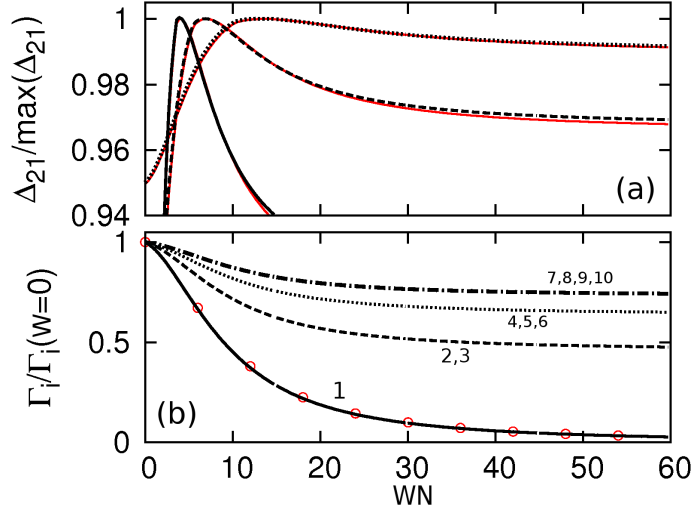


Figure 5.3: (a) The spectral gap Δ_{21} from (5.4-left) as a function of WN for $\gamma = 5$ (solid line), $\gamma = 10$ (dashed line), and $\gamma = 20$ (dotted line). The values on the y -axis are normalized with respect to their maximum in order to allow one a better comparison. (b) The decay rates of the four most stable states vs WN for $\gamma = 20$. In (a,b) $N = 60$ is always kept fixed and W was varied. Doing the same for a different value of $N \gg 1$ produces similar results (red lines in (a) and red circles in (b) for $N = 30$), hence the results are robust as long as $N \gg 1$ (which is necessary for the scaling with WN to be approximately valid).

The left panel in Fig. 5.4 shows the eigenspectrum $\{E_k\}_k$ for typical parameters. There, the decay rates, i.e. Γ_k , are plotted versus the real parts of the spectrum ε_k . One observes immediately the state, in the bottom-right corner of the graph, which is far separated from the rest of the spectrum. Here the structure of the solitonic state is recognized, as discussed before, through the expansion coefficients $|C_{\alpha,k}|$. These are represented by the black dot-line in the right panel (Γ_1). Its stability is given by the rate Γ_1 , where the index starts to count from the most stable state. Therefore the distance of the imaginary parts from the next stable state is a criterion for the stability. It is seen that the next stable states are actually closely degenerate because of the spatial symmetry of the problem, i.e. their projections in the Fock states is nearly given by the linear combination of the states

$$\begin{aligned}
 |\phi(\Gamma_{2,3})\rangle &\rightarrow \{|1, N-1, 0\rangle, |0, N-1, 1\rangle\} \\
 |\phi(\Gamma_{4,5,6})\rangle &\rightarrow \{|1, N-2, 1\rangle, |0, N-2, 2\rangle, |2, N-2, 0\rangle\} \\
 |\phi(\Gamma_{7,8,9,10})\rangle &\rightarrow \{|0, N-3, 3\rangle, |1, N-3, 2\rangle, |2, N-3, 1\rangle, |3, N-3, 0\rangle\}.
 \end{aligned} \tag{5.12}$$

There corresponding prefactors, $C_{\alpha,k} = e^{i\lambda_\alpha} |C_{\alpha,k}|$, are almost equal in magnitude in many of the cases and with normalization $\sum_\alpha |C_{\alpha,k}|^2 \approx 1$. This is shown in the right panel of Fig. 5.4, where only the projections onto the Fock states with decreasing n_2 are shown, but the calculation is done using the complete Fock states.

The spectral gap $\Delta_{21} = \Gamma_2 - \Gamma_1$, is plotted in Fig. 5.3(a) as a function of the effective interaction WN , where N denotes the total particle number in the system (which is fixed to a specific value). We can indeed confirm that the breather state forms for a sufficiently large effective interaction strength. The critical value may be estimated by the maxima of the curves shown in the same panel. These maxima come about because all lower lying states in the spectrum have decreasing decay rates Γ_k as a function of WN , yet the one which decreases fastest is exactly the state, the one with minimal Γ_1 in panel (b).

5. An Open Many-Body System: Decay-rate Analysis

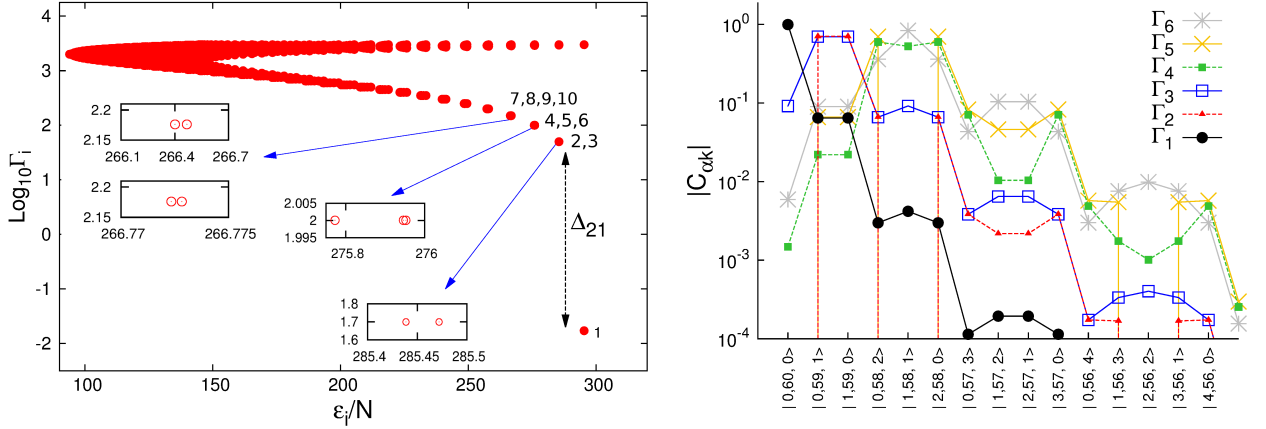


Figure 5.4: (Left) Spectrum of the effective Hamiltonian (5.7) for a loss rate $\gamma = 20$, interaction strength $W = 2$ and fixed number of particles $N = 60$. Shown are $\Gamma_i = -2\text{Im}(E_i)$ vs $\epsilon_i/N = \text{Re}(E_i)/N$. (Right) Expansion coefficients $|C_{\alpha,k}|$ for the first stable states. The Fock basis is ordered with respect to decreasing occupation number n_2 as shown in the x -axis. Note that not all states are plotted, but only the interesting ones.

The qualitative picture remains unchanged for a large range of single-particle loss rates γ in the effective Hamiltonian of equation (5.7), as shown in figure 5.3(a). Increasing γ tends to widen the peak in the spectral gap $\Delta_{21} = \Gamma_2 - \Gamma_1$ and to shift the peak position toward larger values of WN , since more interaction energy is necessary to balance the increasing loss at the outer sites, i.e. to avoid decay into them. An interesting effect can be observed for the very large dissipation rate $\gamma = 20$. As one can see in figure 5.3(a), the normalized spectral gap is almost one even for zero interaction in this case. This means that the decay rate is almost independent of the interaction strength. This happens because strong dissipation blocks the tunneling to the two leaky sites, an effect discussed in detail already in [31, 32].

Case γ_{010} : Effects of the Boundary conditions

The other interesting case of study is the effect of the dissipation in the central well, i.e. $\gamma_2 = \gamma$ and with no dissipation in the boundary wells – see Fig. 5.5. Here the choice of the boundary conditions influences the formation of the type of many-body structures. As before, we show in Fig. 5.6 the behavior of the decay rate as the dissipation increases. The panels (a-d) show

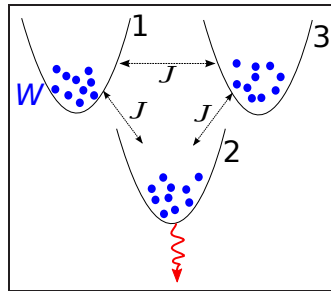


Figure 5.5: Schematic representation of three well system with dissipation in the central well $\gamma_2 = \gamma$. Hard-walls boundary conditions imply no hopping between the well 1 and 3. J and W represent the hopping and the interaction strengths. This figure is a replica from ref. [125] with kind permission of the authors.

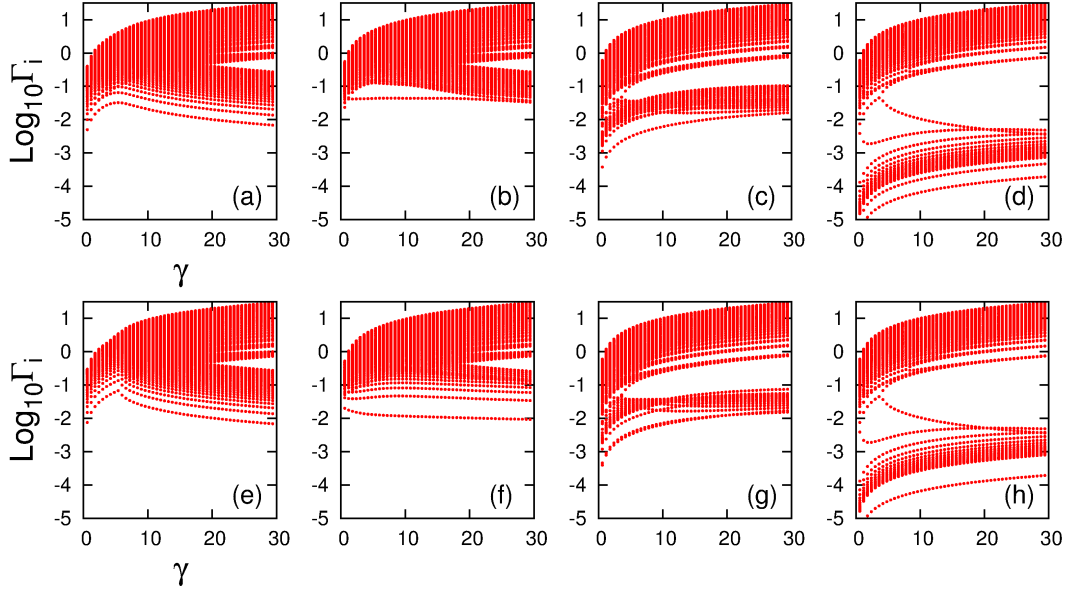


Figure 5.6: (upper panels) Log-plot of the decay rates of the eigenstates with increasing γ , for interaction strength (a,e) $W = 0$, (b,f) $W = 0.1$, (c,g) $W = 1$, (d,h) $W = 10$, with periodic boundary conditions. (lower panels) The same as in the upper panels but hard-walls boundary condition. Note that the spectrum remains almost unaffected by the boundary conditions, however difference appears when studying the structure of the eigenstates $\{|E_k\rangle\}$.

the log-plot of Γ_k as a function of γ , for increasing interaction strengths. Furthermore, periodic boundary conditions (PBC) are used to compute the spectra. Likewise, panels (e-h) show the spectra but using hard-walls. Here we note that the change of boundary condition slightly modifies the results, especially for the case $W = 0.1$, which is below the critical self-trapping limit since $W\bar{n} = 0.2$.

For those values, the lowest eigenstate in Fig. 5.6(b) is favored by the latter superfluid condition $W\bar{n} < J$ and then the particles move almost free in the lattice for weak dissipation and for strong dissipation the state is more leaky. In this manner, the lowest decay rate state is no longer stable. In case of hard-walls the state is more stable for all values of the dissipation rate, since the particle get practically trapped in the boundary wells, therefore it becomes less leaky.

Yet, the differences between the system with PBC and with hard-walls are clearly seen when the structure of the states is studied. For example, in Fig. 5.7-(left) we show the quantum spectrum of the system in both cases, for $\gamma = 20$ and $W = 2$. The regime of interaction strengths is the same shown in Fig. 5.6(c,g), where one can observe two branches: one for most stable eigenstates and the other for the very leaky ones. Notice that the spectrum ε_i vs Γ_i has still a gap which separates these branches, and which increases with γ . By inspecting the expansion coefficients of the eigenstates with the lowest decay rates (Fig. 5.7(b,c)), we see the following structures for PBC:

$$\begin{aligned}
 |\phi(\Gamma_1)\rangle &\rightarrow |N, 0, 0\rangle \\
 |\phi(\Gamma_2)\rangle &\rightarrow |0, 0, N\rangle \\
 |\phi(\Gamma_{3,4})\rangle &\rightarrow \{|N/2, 0, N/2\rangle, |N/2 + 1, 0, N/2 - 1\rangle, |N/2 - 1, 0, N/2 + 1\rangle, \dots\} \\
 |\phi(\Gamma_{5,6})\rangle &\rightarrow \{|N/2 + 1, 0, N/2 - 1\rangle, |N/2 - 1, 0, N/2 + 1\rangle, \dots\}.
 \end{aligned} \tag{5.13}$$

5. An Open Many-Body System: Decay-rate Analysis

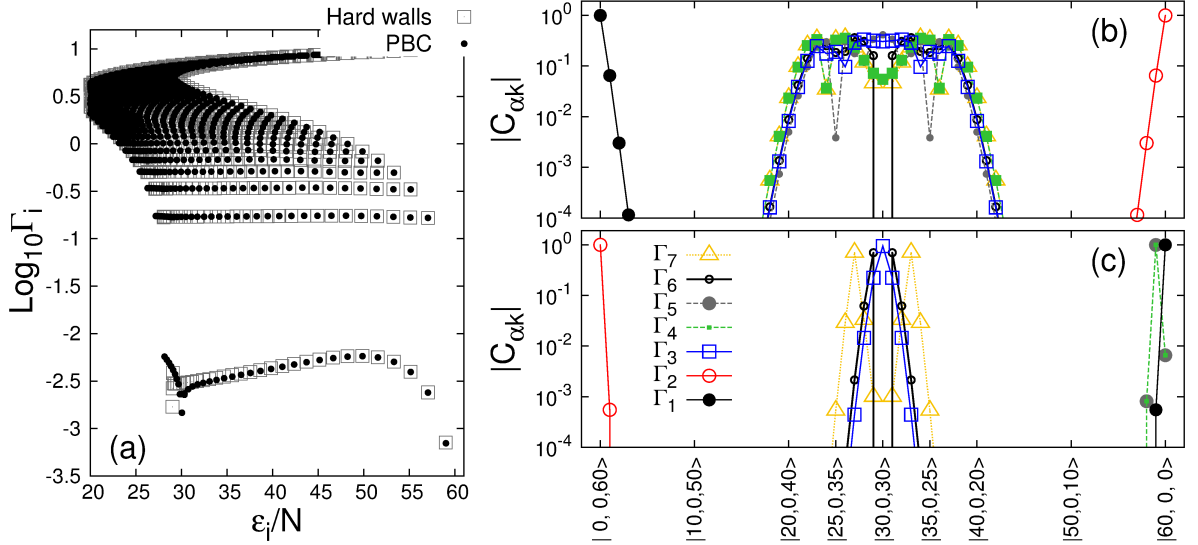


Figure 5.7: (Left) Spectrum of the effective Hamiltonian (5.7) for a loss rate $\gamma = 20$, interaction strength $W = 2$ and fixed number of particles $N = 60$. Shown are $\Gamma_i = -2\text{Im}(E_i)$ vs $\epsilon_i/N = \text{Re}(E_i)/N$. The black dots represent the spectrum with periodic boundary conditions and the grey boxes for hard-wall boundary conditions. (Right) Expansion coefficients $|C_{\alpha,k}|$ for the first six stable states: (b) with PBC and (c) for Hard-walls. The Fock basis is ordered with respect to increasing occupation number n_1 as shown in the x-axis. We only show the projection on states with $n_1 = 0$.

In the case of hard-walls (Fig. 5.8(c)), we obtain

$$\begin{aligned}
 |\phi'(\Gamma_1)\rangle &\rightarrow |N, 0, 0\rangle \\
 |\phi'(\Gamma_2)\rangle &\rightarrow |0, 0, N\rangle \\
 |\phi'(\Gamma_3)\rangle &\rightarrow \{|N/2, 0, N/2\rangle, |N/2 + 1, 0, N/2 - 1\rangle, |N/2 - 1, 0, N/2 + 1\rangle, \dots\} \\
 |\phi'(\Gamma_{4,5})\rangle &\rightarrow \{|N - 1, 0, 1\rangle, |N - 2, 0, 2\rangle, |N, 0, 0\rangle, \dots\}.
 \end{aligned} \tag{5.14}$$

We see that, in the regime of strong dissipation and interparticle interaction, a linear combination of different states with no particles in the central well is obtained, and it is robust with respect to the increasing interparticle interaction.

Note that in case $\gamma = 5$ and $W = 0.1$ (see Fig. 5.6(b)) the results are different in the sense that there exists only one state with the lowest decay rate regardless of the boundary conditions. In this case, the first stable eigenstates have a very interesting structure when expanded in the Fock states (Fig. 5.8(b)), for both conditions, we can see a very symmetric gaussian-shaped expansion of $|\phi(\Gamma_1)\rangle$ and $|\phi'(\Gamma_1)\rangle$ with center in the state $|N/2, 0, N/2\rangle$, i.e.

$$\{|\phi(\Gamma_1)\rangle, |\phi'(\Gamma_1)\rangle\} \rightarrow \{|N/2, 0, N/2\rangle, |N/2 + 1, 0, N/2 - 1\rangle, |N/2 - 1, 0, N/2 + 1\rangle, \dots\} \tag{5.15}$$

However, in the case of PBC the gaussian profile is wider than for hard-walls. This is because of the fact that the particles are forbidden to tunnel from the well 1 to 3 and viceversa, therefore the maximal contribution is from the central state $|N/2, 0, N/2\rangle$. Such a behavior is referred to as *fragmentation of the Bose-Einstein condensate* in ref. [125], where the structure of the eigenstate resembles the Fock state

$$|\phi\rangle = \frac{1}{\sqrt{2^N N!}} (a_1^\dagger \pm a_3^\dagger)^N |0, 0, 0\rangle. \tag{5.16}$$

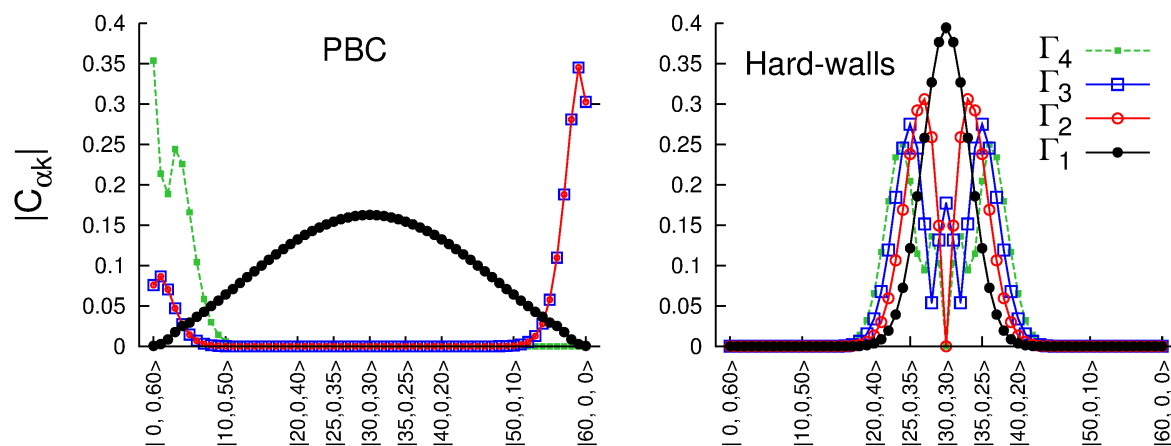


Figure 5.8: Expansion coefficients $|C_{\alpha,k}|$ for the first four stable states, with periodic boundary conditions (left) and hard-wall (right) boundary conditions. The Fock basis is ordered with respect to increasing occupation number n_1 as shown on the x -axis.

An additional noon-type state, $|N,0,0\rangle + |0,0,N\rangle$, is predicted in the PBC case. However, in the approach implemented, such a state is not found to be the most stable, but rather one of the states $|N,0,0\rangle$ or $|0,0,N\rangle$, which we found to be the ones with the lowest Γ_k . We claim that such a kind of state is only obtained after a long-time evolution, which, as mentioned before, cannot be described by our effective Hamiltonian.

5.3 Summary

We have shown that the method based on effective Hamiltonians, as the one of equation (5.7), is a useful tool for the quick identification of states with certain properties, in our case very stable many-body modes. A direct diagonalisation is always possible for small systems, i.e. not too many bosons and lattice sites. For larger many-body systems, a diagonalisation based on the Lanczos method may be used to find interesting states locally in the energy spectrum [20]. To do so, the scaling of eigenstates with the system size for smaller systems can guide the search for the position in the complex energy plane.

Conclusions and Outlook

In this thesis, we have studied two different many-body systems based on experiments with ultracold bosonic atoms and optical lattices. Both of them, with possible experimental realization, which would verify our predictions of emerging many-particle effects [10, 13, 27, 36].

The first system is an extension of the single-band tilted Bose-Hubbard Hamiltonian, which has been amply studied (see ref. [59] and references therein). Motivated by the state-of-the-art experiments with ultracold atoms in higher bands, we modelled a realistic two-band Wannier-Stark system. The optical potential was engineered in order to get rid off higher bands effects, which can be straightforward set up by using bichromatic optical potentials. The parameters of the two-band Bose-Hubbard model were computed using single particle Wannier functions. They can be modified by varying the lattice parameters.

In chapter 3, we studied in detail the spectral properties of the two-band Wannier-Stark system, especially focused on the regime of strongly correlated ultracold bosonic atoms. We implemented numerical techniques to characterize the system. One of them is the Bloch-Floquet-Lanczos formalism, which is a sophisticated method combining diagonalization of large sparse matrices with the very efficient Lanczos algorithm. This method has allowed us to go deeper into the analysis of the eigenspectrum, by computing eigenvalues in different spectral regions defined mainly by the external Stark force. It also brings the possibility of studying large systems reducing the computation times as compared to methods based on the diagonalization of the time evolution operator.

The energy spectrum has been studied in detail in terms of a few system parameters, say, the energy separation between the Bloch bands (Δ_g), the filling factor (N/L) and the resonance order (r). These three parameters, for which the spectrum shows a sensitive dependence, allowed us to study the main features of our many-body system. We have introduced the *man-*

ifold approach that serves to improve the understanding of single- and many-particle effects emerging in the analysis the Wannier-Stark spectrum. In this manner, the system properties can be explained in terms of upperband excitation characterized by the manifold number M , and the manifold degree of mixing ζ . These two quantities have been extensively studied to understand mainly two effects: *local and global spectral mixing*. In the static case, when scanning the many-body spectrum by diagonalization of the Floquet Hamiltonian, local mixing was defined by the intermanifold coupling, which takes place within the resonant regime. As consequence of the weak mixing, the off resonant regime is characterized by the manifolds, where the Floquet eigenstates inherit the properties of the unperturbed basis (see basis). Therefore, it has been shown that they can be mapped with high probability onto the Fock (seed) states. This effect is stronger, the larger the energy bandgap ($\Delta_g \gtrsim 1$). Conversely, global mixing occurs for smaller values the bandgap, typically for $\Delta_g < 0.5$. Therefore, the manifold character of the eigenstate is washed-out for larger forces comparable to Δ_g . Here, a first definition of equilibrium was extracted from the spectral analysis, which is related to the two-state (two-mode) nature of our system. Equilibrium thus occurs in those regimes where the *manifold balance* effect occurs. This implies that both bands are equally populated and there is no longer a one- or two-particle exchange. It was shown that locally the occurrence and clustering of avoided crossings plays a fundamental role to define concepts as *equilibrium and quantum chaos*. The onset of quantum chaos was determined by the filling factor and the gap (at RET domain). This transition is characterized by the competition between one- and two-particle exchange processes between the different manifolds. The critical values for fully chaotic RET regime were found to be $N/L \sim 1$ and $W_x/2\Delta_g \sim 0.1$, where W_x is the interband coupling induced by the interparticle interaction. To characterize the *sea of ACs*, we further developed an efficient method to detect avoided crossings, which is based on the probability vectors and has an explicit connection with the mixing properties of our problem. This method can be implemented for other quantum system as well.

In chapter 4, we studied the dynamical features of the Wannier-Stark system. The main motivation lies in the fact that the quantum evolution by sweeping/quenching appropriated system parameters can actually be implemented in experiments (see [10, 13]). We therefore studied the evolution by quantum sweeps, which was useful to verify mostly all predicted results in the static analysis, that is: the manifold formation, the sensitivity of the quantum chaos emergence on the filling factor and Δ_g , and the relaxation towards equilibrium, which can take place in two instances: (i) by the transit across the chaotic resonant regimes, and also by suddenly quenching the system until the single-particle resonance position is reached and then let the system freely evolve with F fixed. The latter technique was very useful because one can probe the underlying ergodicity¹ in presence of mixing. From this study we recognized the limit for which the system relaxes and reaches a statistical equilibrium at final time. This equilibrium was defined by the gaussian average of the localization measures (GOE and GUE limits). Exactly the same phenomena was seen when sweeping non-adiabatically many different initial conditions, from which equilibrium was defined as the *invariant basis measure* effect. The results are in full agreement with the maximal entropy principle, which establishes a precise definition for the equilibrium state of a quantum system. Here, the most interesting consequence is the fact that in the non-adiabatic limit, one can prepare/obtain such a state via quantum sweeps, across the chaotic RET regime, in finite time evolution, $\sim 100 T_B$. Usually, such a state is only reached in the very long-time evolution after a quench. Furthermore, the relaxation can be engineered as shown throughout the chapters 3 and 4.

¹Spectral average equals the long-time average.

5. An Open Many-Body System: Decay-rate Analysis

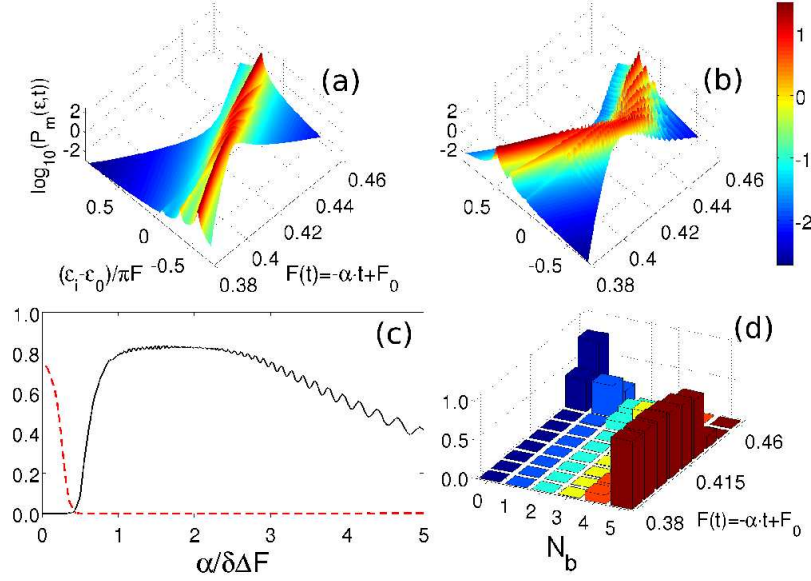


Figure 5.9: State preparation: (a,b) Non-adiabatic evolution of a Mott-like state $|\Phi_0(0)\rangle \approx |111\dots; 000\dots\rangle$ across the resonance regime around $F_{r=1} = 0.4244$. (c) Successful probability of Mott-like $|000\dots; 111\dots\rangle$ for the initial state $|\Phi_0(0)\rangle$ (red) from the left and (black) from the right. (d) Averaged manifold population $P(M)$ for critical value $\alpha_c = 1.2$ with the time evolution from left to right (see [20] for details). Here the long-range coefficients $C_{s>0} = 0$.

Secondly, we have proven the correspondence between spectral and dynamical properties, which allows one to obtain equivalence between the different definitions of equilibrium. This means, in the static analysis equilibrium was defined as *manifold balance* ($M \rightarrow N/2$ and $\zeta \rightarrow 1 - 1/N$), while in the time-domain the equilibrium was defined, firstly as the statistical equilibrium whose signature is the gaussian limits for the delocalization measures, and secondly, by the invariant basis measures, or the equivalence between the coefficients A_ν and C_i . In the last part of the chapter 4, we have seen that all three definitions are equivalent, i.e. we have

$$\text{Manifold balance} \iff \text{GOE (GUE) limits} \iff \text{basis invariance.} \quad (5.17)$$

In this way, we can conclude that quantum chaos can be detected via non-adiabatic dynamics across the RET domain, whose "robust" signature is the formation of the equilibrium state, which can be tested by using the manifold measures. The results here exposed are in good agreement with the energy shell approach [110]. A natural question comes thus into play: reached the equilibrium, does our system *thermalize*? The short answer would be: probably, according to detailed study presented in this thesis. Nevertheless, we must exhaustively prove the occurrence of thermalization by the different analyses done, e.g. in [110, 129–131], and other authors.

In previous works [121], we have found that one can prepare other types of states, for example that shown in Fig. 5.9. That result is, unfortunately, very sensitive to the long-range couplings, i.e. the dipole-induced terms $C_{s>1}$, likewise for some dynamical features reported in previous works [64]. We therefore have still some open questions: (a) Is it still possible to prepare specific upper band states as shown in Fig. 5.9? (b) Can we construct effective models that describe the evolution at fixed forces (in the regular regime), thus reducing the complexity when analytically dealing with the many-body Wannier-Stark system? (c) does really thermalization happen in our closed system, and how can be define it?

Finally, in the last chapter we have characterized the behavior of the decay rate of a leaky single-band Bose-Hubbard Hamiltonian. This system is investigated in the static context, i.e. in the same way as we studied the many-body system in chapter 3. As well as the Wannier-Stark system, the type of system here studied has immediate experimental applications (see ref. [27, 28]). In general terms, we showed that very stable macrostates can be created as a result of the interplay between dissipation and interparticle interaction. Stability criteria can be set by studying the quantum spectrum, which can be obtained by diagonalization of an effective Hamiltonian. That Hamiltonian is the sum of the closed system plus an absorbing potential, which models the dissipation. As an example, we studied a three-well case, for which two different types of dissipation were allowed. Only with this Hamiltonian one can easily recognize some of those predicted states [31, 32], i.e. discrete solitons, fragmented states among others, without time-consuming Monte-Carlo simulations.

As a final remark of the chapter 5, one may find analogies to the phenomenon of resonance trapping in open systems often described by effective non-hermitian Hamiltonians [115, 132]. This phenomenon describes the formation of a gap in the imaginary parts of the spectrum when the opening of the system is increased. The consequence is that very few very stable states exist as compared with a large number of fast decay ones. This effect appears as the opening, described by γ in our case, increases, whilst in our problem presented before, the stable breather state rather forms when increasing the interparticle interaction strength (and remaining qualitative unchanged over a wide range of γ). Nevertheless it would certainly be interesting to further investigate this analogy for many-body quantum systems.

APPENDIX

Band Structure, Wannier functions and Bose-Hubbard Parameters

A.1 Band Structure

Consider an one-dimensional bichromatic optical potential obtained by superposing two sinusoidal functions with different spatial periods

$$V(x) = -(V_0 \cos(2k_L x) + V_1 \cos(4k_L x + \phi)), \quad (\text{A.1})$$

where k_L stands for the recoil momentum. The potential $V(x)$ is particularly interesting, since the lattice depths V_0 , $s_0 = V_1/V_0$ and the phase difference ϕ are easily controlled in the experiment (see Ref. [42]). We can engineer a miniband structure, for which the two lowest Bloch energy bands are well separated from the third and further higher bands. The parameters of the Bose-Hubbard Hamiltonian [54, 133] are conventionally computed by using the eigenvalues and eigenenergies of the spinless single particle Hamiltonian

$$\hat{H}_0 = -\frac{\hbar^2}{2m_0} \frac{\partial^2}{\partial x^2} + V(x), \quad \text{with } V(x + d_L) = V(x), \quad (\text{A.2})$$

with d_L being the spatial period of the lattice. The eigenfunctions of the latter Hamiltonian are the well-known Bloch functions given by

$$\psi_k^\alpha(x) = e^{ikx} u_k^\alpha(x), \quad \text{with } u_k^\alpha(x + d_L) = u_k^\alpha(x), \quad (\text{A.3})$$

where k is the magnitude of the momentum of the particle in the system, commonly called quasimomentum. α is the band index. Following the standard procedure, we can find the differential equation for $u_k^\alpha(x)$ by using the relation $H\psi_k^\alpha(x) = E_k^\alpha \psi_k^\alpha(x)$, thus arriving at the formula

$$\left[\frac{(p + \hbar k)^2}{2m_0} + V(x) \right] u_k^\alpha(x) = E_k^\alpha u_k^\alpha(x), \quad (\text{A.4})$$

which is reduced to an eigenvalue problem. In the first step, we use the Fourier expansion $u_k^\alpha(x) = \sum_n u_n(\alpha, k) e^{i2\pi n \frac{x}{d_L}}$ and secondly, after multiplying by $\exp(-i2\pi m \frac{x}{d_L})$ and integrating over a unit cell, we thereby obtain the matrix

$$M_{nm}^{(k)} = \frac{1}{2m_0} \left(\hbar k + 2\pi \hbar \frac{n}{d_L} \right)^2 \delta_{nm} + V_{nm}, \quad \text{with } V_{nm} = \int_{-d_L}^{d_L} dx e^{i2\pi(n-m)\frac{x}{d_L}} V(x). \quad (\text{A.5})$$

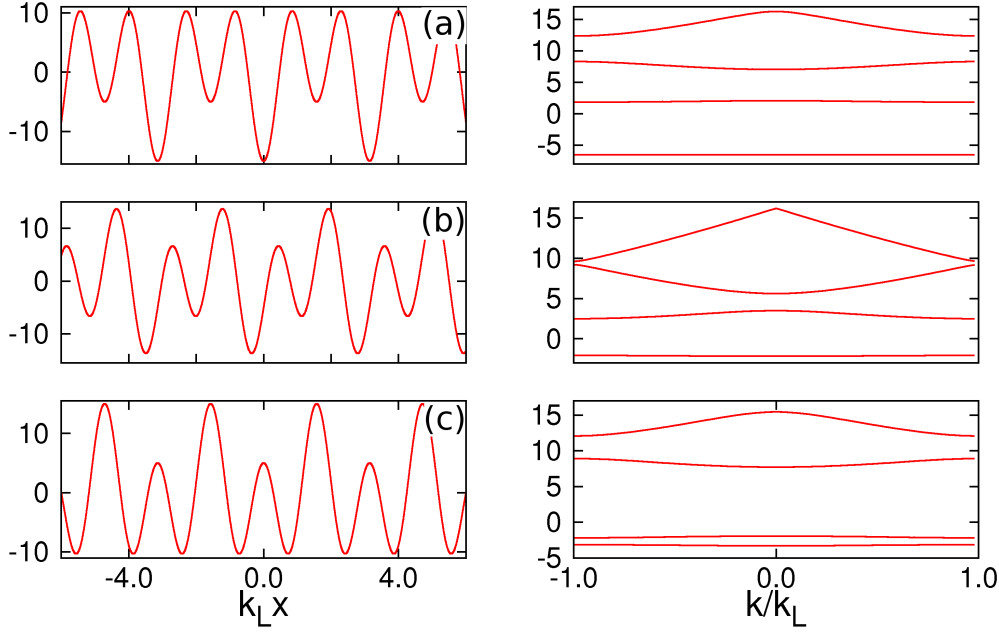


Figure A.1: Dependence of the band structure on ϕ . (left) Potential profile and (right) the corresponding band structure. (a) $\phi = 0$, (b) $\phi = \pi/2$ and (c) $\phi = \pi$.

Hereafter we use the recoil energy $E_r = \hbar^2 k_L^2 / 2m_0$ as the energy unit, with the momentum recoil $k_L = \pi/d_L$ and $\hbar = 1$. For simplicity we use the rescaling

$$k \rightarrow k/k_L, \quad x \rightarrow k_L x, \quad V_i \rightarrow V_i/E_r. \quad (\text{A.6})$$

The characteristic eigenvalue equation is given by

$$[(k + 2n)^2 - \epsilon_k^\alpha] u_n(\alpha, k) + \sum_n \tilde{V}_{nm} u_n(\alpha, k) = 0, \quad (\text{A.7})$$

with \tilde{V}_{nm} being the matrix elements of the potential $V(x)$ obtained from the formula

$$\tilde{V}_{nm} = -\frac{V_0}{2}(\delta_{n,m+1} + \delta_{n,m-1}) - \frac{V_1}{2}(\delta_{n,m+2} e^{i\phi} + \delta_{n,m-2} e^{-i\phi}). \quad (\text{A.8})$$

The Fourier components $u_n(\alpha, k)$ and the energy ϵ_k^α are computed by solving the Eq. A.7, and any other bandstructure property can be expressed as a function of the triple $(V_0, s_0 = V_1/V_0, \phi)$. For instance, in Fig. A.1 we show in the left panels the potential profile for phase differences $\phi = \{0, \pi/2, \pi\}$. In our realization, we choose the potential with $\phi = \pi$, since the two lowest Bloch bands become well separated from the rest of the spectrum as shown in right panel of the Fig. A.1-(c).

We characterize the range of parameter, for which the miniband structure is valid through the energy gaps between the Bloch bands, especially at the center and at the edge of the Brillouin Zone, i.e. $\Delta_0 = \epsilon_{k=0}^2 - \epsilon_{k=0}^1$, $\Delta_1 = \epsilon_{k=1}^2 - \epsilon_{k=1}^1$ and $\Delta_2 = \epsilon_{k=0}^3 - \epsilon_{k=0}^2$. The behavior of these parameters is shown in Fig. A.2 as a function of the relative lattice depth $s_0 = V_1/V_0$ (left panel) given different fixed values of V_0 , and as a function of the V_0 for $s_0 = 1, 3$ and 4 . In the first case we see that the ratio Δ_2/Δ_0 increases faster as s_0 or (and) V_0 increase(s), therefore a realistic isolated two-band model is also set for not necessary deeper lattice well as in the case of a one-period optical lattice, i.e. for $V_1 = 0$.

A. Band Structure, Wannier functions and Bose-Hubbard Parameters

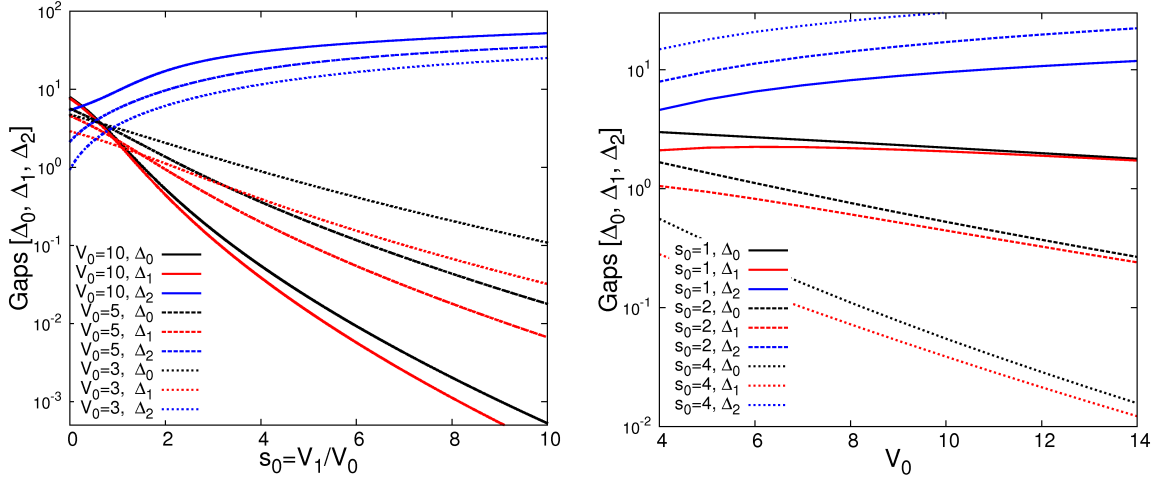


Figure A.2: The miniband structure. Energy Gaps Δ_0 , Δ_1 and Δ_2 , as defined in the main text, as a function of: (left) the relative lattice depths $s_0 = V_1/V_0$ for $V_0 = 3, 5, 10$ and (right) the lattice depth V_0 for $s_0 = 1, 3$ and 4 .

Along of this thesis we restrict the values of $V_0 < 15$, since by increasing s_0 the gaps $\Delta_{0,1}$ become smaller and this can entangled the energy Bloch bands, thus the treatment implemented here must be changed. In this way, we set $\Delta_{0,1} \geq 0.1$.

A.2 Wannier Functions

The tight-binding approach is based on the highly localized Wannier functions, see Ref. [46–48]. Under the assumption of non-entangled energy bands, these functions are defined as Fourier transform of the Bloch functions Eq. (A.3) as follows

$$\chi_{\alpha,l}(x) = \sqrt{\frac{d_L}{2\pi}} \int_{-1}^1 e^{-ix_l k} \psi_k^\alpha(x) dk, \quad (\text{A.9})$$

with $x_l = d_L l$. In order to obtain the optimal highly localized Wannier functions, we must notice that the quasimomentum in Eq. (A.3) is just a parameter. It means that in general, the Bloch functions can be written as

$$\Psi_k^\alpha(x) = e^{i\theta(k)} \psi_k^\alpha(x), \quad \theta(k+2) = \theta(k), \quad (\text{A.10})$$

for any arbitrary function $\theta(k)$. A clever choice of the latter brings us to optimally localized Wannier functions which drop exponentially as $|x| > d_L$. This means

$$\lim_{x \rightarrow \pm\infty} \chi_\alpha^l(x) \sim e^{-h|x|}. \quad (\text{A.11})$$

Unfortunately, the choice of the phase prefactor is not a trivial task, so we can find a variety of proposals in the literature (see Ref. [47–50]) to construct these functions. The most conventional implementation is based on the optimization algorithm introduced by Vanderbilt et al. [49, 50] for composite and entangled bands. In the 50's W. Kohn et al. presented a receipt for the construction of Wannier functions by considering the properties of the Bloch functions into the first Brillouin Zone. In Ref. [58] the Wannier functions for one-period optical lattice are computed by choosing the phase factor such that the Bloch functions are continuous on k for every x , which is obtained by setting

$$u_j(1, k) \rightarrow |u_j(1, k)|, \quad u_j(2, k) \rightarrow |u_j(2, k)| \text{sign}(2j + u_j(1, k)). \quad (\text{A.12})$$

Thereby, the Wannier functions for the two lowest bands in the well $l = 0$ read

$$\begin{aligned} \chi_{1,0}(x) &= N_1 \sum_{k_j, n} |u_n(1, k_j)| e^{i(2k_j+n)x} \\ \chi_{2,0}(x) &= N_2 \sum_{k_j, n} |u_n(2, k_j)| \text{sign}(2j + k) e^{i(2k_j+n)x} \end{aligned} \quad (\text{A.13})$$

with N_i 's being normalization constants. This latter choice ensures that the Wannier functions have a maxima at $x = 0$ and preserve their symmetry properties, $\chi_{\alpha,l}(-x) = (-1)^{\alpha-1} \chi_{\alpha,l}(x)$. For the case $V_1 \neq 0$ such that choice does not work out, nevertheless the Wannier functions for the two-period optical lattice inside of a unit cell must behave as the wavefunctions of a single double-well potential. Thus, the Wannier functions have a maxima at the minimum of $V(x)$, $x_0 = \pm \frac{1}{2} \cos^{-1}(1/4s_0)$. To obtain these functions we consider the invariance of the eigenenergies ε_k^α under the shift $x \rightarrow x \pm x_0$. The Bloch functions simply become globally maximal at $\pm x_0$ and are smooth function on k . In this way, we define new Bloch functions as following

$$\psi_k^{1,2}(x) = \frac{1}{\sqrt{2}} \left(\psi_k^{1,2}(x + x_0) \pm \psi_k^{1,2}(x - x_0) \right), \quad (\text{A.14})$$

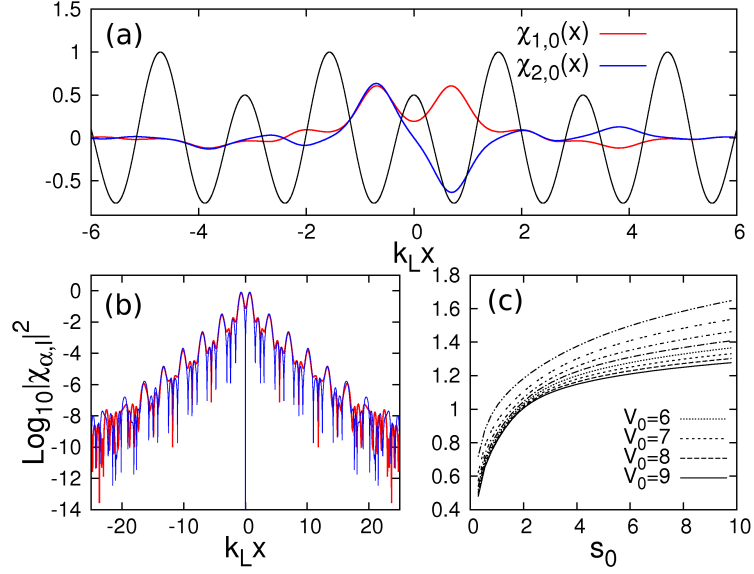


Figure A.3: (a) Wannier functions for the two lowest Bloch bands with $V_0 = 5$ and $s_0 = 3$. (b) This panel shows the exponential decay of the Wannier functions from panel (a). (c) dispersion $\sigma = \sqrt{\langle x^2 \rangle - \langle x \rangle^2}$ for the Wannier functions as a function of the relative lattice depths s_0 , with fixed $V_0 = 1, 2, \dots, 9$.

and the phase prefactor is defined such that $u_j(\alpha, k) \rightarrow |u_j(\alpha, k)|$. The double-Well Wannier functions are therefor given by

$$\begin{aligned} \chi_{1,0}(x) &= N_1 \sum_{k_j, n} |u_n(1, k_j)| \cos[(2n + k_j)x_0] \cos[(2n + k_j)x] \\ \chi_{2,0}(x) &= iN_2 \sum_{k_j, n} |u_n(2, k_j)| \sin[(2n + k_j)x_0] \sin[(2n + k_j)x]. \end{aligned} \quad (\text{A.15})$$

In Fig. A.2 we show an example of above functions for some bandstructure paramters. We see that our choice satisfy the symmetry properties of $\chi_{\alpha,l}$, and additionally these are well localized in the unit cell centered at $x = 0$. In panel (c) we show the localization parameter $\sigma = \sqrt{\langle x^2 \rangle - \langle x \rangle^2}$, with $\langle x^n \rangle \equiv \int x^n |\chi_{\alpha,l}|^2 dx$ being the nth-moment.

So far we have shown how to engineer an optical potential that allows to isolate the two lowest Bloch bands. We compute the respective Wannier functions, which are very important in the implementation of tight-binding approach. In the next section we show how compute the Bose-Hubbard coefficients by using the single particle Wannier functions.

A.3 Seed basis and Bose-Hubbard Parameters

As defined in the main text (sec. 3.1.1), the gauge-transformed Hamiltonian, with periodic boundary condition can be treated using the translationally invariant Fock space basis, i.e. the seed states basis [58, 59] defined as follows

$$|s, \kappa_j\rangle = \frac{1}{\sqrt{M(s)}} \sum_{l=1}^{M(s)} e^{i2\pi\kappa_j l} \hat{S}^l |\vec{n}_{ab}\rangle, \quad (\text{A.16})$$

A.3. Seed basis and Bose-Hubbard Parameters

$\kappa = 0$	$L = 1$	$L = 2$	$L = 3$	$L = 4$	$L = 5$	$L = 6$	$L = 7$	$L = 8$	$L = 9$
$N = 1$	2	2	2	2	2	2	2	2	2
$N = 2$	3	6	7	10	11	14	15	18	19
$N = 3$	4	10	20	30	44	62	80	102	128
$N = 4$	5	19	42	86	143	231	340	490	665
$N = 5$	6	28	84	198	402	728	1224	1938	2926
$N = 6$	7	44	156	434	1001	2076	3876	6798	11221
$N = 7$	8	60	264	858	2288	5304	11076	21318	38456
$N = 8$	9	85	429	1619	4862	12618	29070	61334	120175

Table A.1: Dimension of the Hilbert space expanded by the seed states basis.

where \hat{S} is the translation operator, $\kappa_j = \frac{j}{M(s)}$, $j = 1, \dots, M(s)$, and $M(s)$ is the number of cyclic permutations of the fock state $|\vec{n}_{ab}\rangle = |n_1^a n_2^a \dots n_L^a\rangle \otimes |n_1^b n_2^b \dots n_L^b\rangle$. In table Tab. A.1 we show the size of the Hilbert space expanded by the seed states, with reduced dimension $\mathcal{N}_s \approx \dim(\mathcal{H})/L$.

The Bose-Hubbard coefficients, sketched in Fig. 3.1(a) and Fig. 2.4, are obtained from the following relations:

- hopping strengths J_β :

$$J_{l-l'}^\beta \equiv \int \chi_\beta(x-x_l) H_0(x) \chi_\beta(x-x_{l'}) dx = \epsilon_{l-l'}^\beta, \quad (\text{A.17})$$

where $J_a \equiv J_1^{\beta=a}$, $J_b \equiv J_1^{\beta=b}$, and $\Delta_g = |\epsilon^b - \epsilon^a| = |J_0^{\beta=b} - J_0^{\beta=a}|$.

- The dipole-like coupling strength C_0 :

$$C_s^{\beta\beta'} \equiv \int \chi_\beta(x) x \chi_{\beta'}(x-d_L s) dx = \int \chi_\beta(x) x \chi_{\beta'}(x+d_L s) dx, \text{ with } C_s \equiv C_s^{ab}. \quad (\text{A.18})$$

Because of the localization of the Wannier functions, coefficient with $s = |l-l'| > 2$ are at most two orders of magnitude smaller than $C_{0,1,2}$ and thus we do not take them into account. Furthermore, due to the symmetry properties of the Wannier function all the coefficients for $\beta = \beta'$ are zero. Note that in the single particle case at the exact resonance only the coupling $s = 0, r$ are relevant and we get RWA-type of Hamiltonian.

- Finally, the repulsive, intraband, on-site inter-particle interaction terms are given by,

$$W_\beta \equiv g_{1D} \int \chi_\beta^4(x) dx. \quad (\text{A.19})$$

The interband on-site inter-particle interaction is

$$W_x \equiv g_{1D} \int \chi_a^2(x) \chi_b^2(x) dx. \quad (\text{A.20})$$

The interaction strength is defined by $g_{1D} = 4\pi a_{1D}/m_0$, with a_{1D} the one-dimensional scattering constant and m_0 the mass of the atoms [7, 134].

Some values of these parameters are shown in the tables A.2 and A.3.

A. Band Structure, Wannier functions and Bose-Hubbard Parameters

V_0	Δ_g	J_a	J_b	W_a	W_b	W_x	C_0	$ C_1 $	$ C_2 $	$ C_3 $
2.0	1.380	0.203	-0.372	0.017	0.022	0.019	-0.094	0.054	0.0169	0.0087
3.0	1.026	0.135	-0.203	0.020	0.025	0.022	-0.095	0.049	0.0111	0.0051
4.0	0.754	0.089	-0.118	0.023	0.026	0.024	-0.095	0.046	0.0078	0.0034
5.0	0.556	0.059	-0.072	0.025	0.028	0.026	-0.096	0.043	0.0055	0.0024
6.0	0.413	0.040	-0.045	0.027	0.029	0.028	-0.096	0.041	0.0039	0.0018
7.0	0.310	0.027	-0.029	0.029	0.030	0.029	-0.097	0.040	0.0027	0.0015
8.0	0.235	0.018	-0.020	0.030	0.031	0.031	-0.097	0.039	0.0018	0.0012
9.0	0.180	0.013	-0.013	0.031	0.032	0.032	-0.098	0.038	0.0011	0.0010
10.0	0.139	0.009	-0.009	0.033	0.033	0.033	-0.098	0.037	0.0005	0.0009
11.0	0.108	0.006	-0.006	0.034	0.034	0.034	-0.098	0.036	0.0001	0.0008
12.0	0.084	0.005	-0.005	0.034	0.035	0.035	-0.098	0.035	0.0004	0.0007
13.0	0.067	0.003	-0.003	0.035	0.036	0.035	-0.098	0.035	0.0007	0.0007
14.0	0.053	0.002	-0.002	0.036	0.036	0.036	-0.099	0.034	0.0010	0.0006
15.0	0.042	0.002	-0.002	0.037	0.037	0.037	-0.099	0.034	0.0012	0.0006

Table A.2: Bose-Hubbard parameters for $s_0 = 3$, in recoil energy.

s_0	Δ_g	J_a	J_b	W_a	W_b	W_x	C_0	$ C_1 $	$ C_2 $	$ C_3 $
0.5	3.661	0.0593	-0.3389	0.0210	0.0249	0.0184	-0.0841	0.0365	0.0055	0.0026
1.0	2.532	0.0776	-0.2402	0.0185	0.0246	0.0191	-0.0901	0.0351	0.0029	0.0021
1.5	1.714	0.0852	-0.1736	0.0193	0.0252	0.0211	-0.0922	0.0364	0.0002	0.0023
2.0	1.161	0.0815	-0.1276	0.0212	0.0261	0.0231	-0.0939	0.0388	0.0021	0.0022
2.5	0.796	0.0713	-0.0950	0.0232	0.0270	0.0248	-0.0951	0.0412	0.0040	0.0022
3.0	0.556	0.0593	-0.0716	0.0250	0.0279	0.0263	-0.0959	0.0433	0.0055	0.0024
3.5	0.395	0.0479	-0.0544	0.0266	0.0287	0.0276	-0.0963	0.0451	0.0069	0.0028
4.0	0.285	0.0382	-0.0417	0.0279	0.0295	0.0287	-0.0966	0.0466	0.0082	0.0033
4.5	0.209	0.0303	-0.0322	0.0291	0.0302	0.0296	-0.0967	0.0479	0.0094	0.0038
5.0	0.155	0.0240	-0.0251	0.0300	0.0309	0.0305	-0.0968	0.0490	0.0105	0.0044
5.5	0.117	0.0190	-0.0196	0.0309	0.0315	0.0312	-0.0968	0.0499	0.0115	0.0049
6.0	0.089	0.0151	-0.0155	0.0316	0.0321	0.0318	-0.0967	0.0507	0.0125	0.0055

Table A.3: Bose-Hubbard parameters for $V_0 = 3$, in recoil energy.

Floquet-Lanczos Diagonalization

B.1 Floquet Bose-Hubbard Hamiltonian

The time-dependent Hamiltonian $\hat{H}(t)$ (see main text) has a number s of frequencies $\omega_i = \omega_B, 2\omega_B, \dots, (L+1)\omega_B$, all of them being multiples of the fundamental Bloch frequency ω_B , i.e. $\hat{H}(t)$ is periodic in time. We can avoid the time integration of the evolution operator as done in [59] by equivalently diagonalizing the matrix representation of the Floquet operator [101, 135, 136]

$$H_f = \hat{H}(t) - i\partial_t, \rightarrow H_f|\varepsilon_i(t)\rangle = \varepsilon_i|\varepsilon_i(t)\rangle. \quad (\text{B.1})$$

The eigenstates $|\varepsilon_i(t)\rangle$ have the same periodicity of the Hamiltonian and can be expanded in multi-mode Fourier decomposition ([137]) as follows

$$|\varepsilon_n(t)\rangle = \sum_{k_1} \sum_{k_2} \dots \sum_{k_{s_{max}}} e^{-i(k_1\omega_1 + k_2\omega_2 + \dots + k_{s_{max}}\omega_{s_{max}})t} |\phi_{\varepsilon_n}^{k_1 k_2 \dots k_{s_{max}}}\rangle = \sum_{k_s} e^{-ik_s\omega_B t} |\phi_{\varepsilon_n}^{k_s}\rangle. \quad (\text{B.2})$$

with $k_s = k_1 + 2k_2 + \dots + (L+1)k_{L+1}$. By using (B.1) and (B.2), the Floquet matrix reads

$$(\mathbf{H}_0 - 2\pi k F \hat{\mathbf{I}}) |\phi_{\varepsilon_n}^k\rangle + \mathbf{J} |\phi_{\varepsilon_n}^{k-1}\rangle + \mathbf{J}^\dagger |\phi_{\varepsilon_n}^{k+1}\rangle + \sum_{s=1}^L \left[\mathbf{C}_s |\phi_{\varepsilon_n}^{k-s}\rangle + \mathbf{C}_s^\dagger |\phi_{\varepsilon_n}^{k+s}\rangle \right] = \varepsilon_n \hat{\mathbf{I}} |\phi_{\varepsilon_n}^k\rangle \quad (\text{B.3})$$

where the operators \mathbf{J} and \mathbf{C}_s are defined by the formulae

$$\mathbf{J} = \frac{1}{2} \sum_l (J_a a_{l+1}^\dagger a_l + J_b b_{l+1}^\dagger b_l) \quad \text{and} \quad \mathbf{C}_s = F C_s \sum_l a_{l+s}^\dagger b_l. \quad (\text{B.4})$$

The operator \mathbf{H}_0 contains the time-independent part of $\hat{H}(t)$. The problem now is reduced to compute the fourier states $|\phi_{\varepsilon_n}^k\rangle$ which is done by numerical diagonalization of the following $(2L+1)$ -diagonal block matrix

$$\mathcal{M}_F^{(s)} = \begin{bmatrix} \mathbf{H}_0 - \omega_B(k-2)\mathbb{1} & \mathbf{J}^\dagger + \mathbf{C}_1 & \mathbf{C}_2^\dagger & \dots & \\ \mathbf{J} + \mathbf{C}_1 & \mathbf{H}_0 - \omega_B(k-1)\mathbb{1} & \mathbf{J}^\dagger + \mathbf{C}_1 & \mathbf{C}_2^\dagger & \vdots \\ \mathbf{C}_2 & \mathbf{J} + \mathbf{C}_1 & \mathbf{H}_0 - \omega_B k \mathbb{1} & \mathbf{J}^\dagger + \mathbf{C}_1 & \mathbf{C}_2^\dagger \\ \vdots & \mathbf{C}_2 & \mathbf{J} + \mathbf{C}_1 & \mathbf{H}_0 - \omega_B(k+1)\mathbb{1} & \mathbf{J}^\dagger + \mathbf{C}_1 \\ \dots & \dots & \mathbf{C}_2 & \mathbf{J} + \mathbf{C}_1 & \mathbf{H}_0 - \omega_B(k+2)\mathbb{1} \end{bmatrix},$$

with every block having the same dimension of the original Hamiltonian, i.e. $\dim = \mathcal{N}_S$. As said in the main text (see Sec. 3.1.1), we can disregard those blocks with $s > 2$ since the coefficients

$C_s \ll 1$, therefore the the eigensystem to solve is given for the matrix $\mathcal{M}^{(s_{max}=2)}$. The eigenenergies lie within the so-called Floquet zone: $\varepsilon_i \in [\varepsilon_0 - \omega_B/2, \varepsilon_0 + \omega_B/2]$ of width ω_B , and centered at ε_0 , where ε_0 can be conveniently set as a function of any free parameter, e.g. F . Due to the periodicity of the eigenenergies, the extended spectrum can be obtained just by shifting the Floquet zone as $\varepsilon_i \rightarrow \varepsilon_i + n_{Fl}\omega_B$. The integer n_{Fl} label the Floquet zone. The eigenstates of the matrix $\mathcal{M}^{(s)}$ can be expanded in the seed basis by writting the k -components as $|\phi_{\varepsilon_j}^k\rangle = \sum_k c_{k,\lambda} |s_\lambda\rangle$, where the coefficients $c_{k,\lambda}$ are obtained through the diagonalization. Therefore we can write

$$|\varepsilon_i\rangle = \sum_{k,\lambda} c_{k,\lambda} |s_\lambda\rangle = \sum_{\lambda} \left(\sum_k c_{k,\lambda} \right) |s_\lambda\rangle = \sum_{\lambda} c_{\lambda} |s_\lambda\rangle, \quad (\text{B.5})$$

with the contraction $c_{\lambda} = \sum_k c_{k,\lambda}$. Additionally in this formalism the evolution operator reads

$$\hat{U}(t_2, t_1) = \sum_{j,k,k'} e^{-i\varepsilon_j(t_2-t_1)} e^{-i\omega_B k t_1} e^{i\omega_B k' t_2} |\phi_{\varepsilon_j}^{k'}\rangle \langle \phi_{\varepsilon_j}^k| \quad (\text{B.6})$$

and any general time-dependent wave function, with initial condition $|\phi(0)\rangle$, can be written as

$$|\psi(t,0)\rangle = \sum_j c_{j,0} \sum_k e^{-i(\varepsilon_j + \omega_B k)t} |\phi_{\varepsilon_j}^k\rangle, \quad c_{j,0} = \sum_{k'} \langle \phi_{\varepsilon_j}^{k'} | \phi(0) \rangle. \quad (\text{B.7})$$

The diagonalization of the Floquet matrix demands a huge memory usage, especially for larger system and/or $s_{max} > 2$. Therefore some conventional diagonalization methods are inefficient since those have to compute the whole set of eigenenergies of the system. In our case, we only need those that lie inside of a Floquet zone, from which we can construct the complete spectrum as explained above. We then implement a Lanczos algorithm [136, 138–140] which is more suitable for our numerical calculations.

B.2 Lanczos Algorithm

The dimension of the Floquet matrix $\mathcal{M}_F^{(2)}$ is given by $dim_F = \mathcal{N}_s \Delta k$, with Δk the number of Fourier components needed to obtain good convergence of \mathcal{N}_s eigenvalues. Furthermore, $\mathcal{M}_F^{(2)}$ is a very sparse matrix, which is an usefull property for the Lanczos diagonalization algorithm. This algorithm is a powerfull method for computing a certain number of eigenenergies in the vicinity of some predefined energy position ε_0 , and it has been amply used especially to find the eigenvalues of large symmetric matrices [138, 140]. This routine can also be used to solve a general eigenvalue problem, i.e. $\mathcal{A}\mathbf{x} = \varepsilon\mathcal{B}\mathbf{x}$.

Let ε_0 be the position in the energy axis. We now shift the matrix \mathcal{A} as follows

$$\mathcal{A} \rightarrow \mathcal{A} + \varepsilon_0 \mathcal{B}, \quad (\text{B.8})$$

and then we multiply from the left by \mathcal{A}^{-1} . By defining $\mu = 1/\lambda = 1/(\varepsilon - \varepsilon_0)$, we get an equivalent eigensystem

$$\mathcal{A}^{-1} \mathcal{B} \mathbf{x} = \mu \mathbf{x}, \quad (\text{B.9})$$

which is the general eigenvalue problem that we are interested to solve. Lanczos method belongs to the family of diagonalization algorithm, so-called power methods, which are very usefull to compute the maximal modulus eigenvalue of a matrix. In our case, when finding

B. Floquet-Lanczos Diagonalization

out μ_{max} , we immediately obtain the smallest λ which is the closest eigenvalue to the initial position ε_0 . At this part, by redefining the initial guess as the found eigenvalue and start again the previous process. After n_{lancz} iterations of this procedure, we can then compute M convergent eigenvalues that lie into the vicinity of ε_0 , in general $M < n_{lancz}$. Other parameter control is the number of Fourier components Δ_k , which also enhances the performance of the algorithm, i.e. M increases.

The Lanczos algorithm is base on the construction of the Krylov subspace

$$K_{n_{lancz}}[\mathcal{A}^{-1}\mathcal{B}, \eta_1] = \text{span}\{\eta_1, \mathcal{A}^{-1}\mathcal{B}\eta_1, (\mathcal{A}^{-1}\mathcal{B})^2\eta_1, \dots, (\mathcal{A}^{-1}\mathcal{B})^{n_{lancz}-1}\eta_1\} \quad (\text{B.10})$$

where η_1 is an initialization vector, with $\|\eta_1\| = 1$ and n_{lancz} is the dimension of the Krylov subspace, which in our case is called the number of Lanczos iterations. The matrix $\mathcal{P} = (\eta_1, \eta_2, \dots, \eta_{n_{lancz}-1})$ is an ortogonal matrix with respect to \mathcal{B} , i.e. $\mathcal{P}^T \mathcal{B} \mathcal{P} = 1$. Furthermore, by using the matrix \mathcal{P} , the matrix $\mathcal{A}^{-1}\mathcal{B}$ is transformed in a tridiagonal symmetric matrix $\mathcal{T} = \mathcal{P}^{-1} \mathcal{A}^{-1} \mathcal{B} \mathcal{P}$, which is then diagonalized by standard diagonalization routine, e.g. QR-decomposition, in order to obtain the largest eigenvalues μ_i . The matrix elements of \mathcal{T} are given by the formulae [136]

$$\begin{aligned} \alpha_j &= \eta_j^T \mathcal{B} \mathcal{A}^{-1} \mathcal{B} \eta_j, \\ \beta_j &= \|\mathbf{t}_{j+1}^T \mathcal{B} \mathbf{t}_{j+1}\|, \text{ with } \mathbf{t}_{j+1} = \mathcal{A}^{-1} \mathcal{B} \eta_j - \alpha_j \eta_j - \beta_{j-1} \eta_{j-1}, \\ \eta_{j+1} &= \frac{1}{\beta_{j+1}} \mathbf{t}_{j+1}, \end{aligned} \quad (\text{B.11})$$

with $\mathcal{T}_{i,i} = \alpha_i$ and $\mathcal{T}_{i,i+1} = \beta_i$. For the initialization of the algorithm, we set $\eta_1 = (1, 1, 1, \dots, 1)^T$ and the normalization of any η_j is computed respect to the matrix $\mathcal{B} = \mathbb{1}$, with $\mathbb{1}$ the identity matrix.

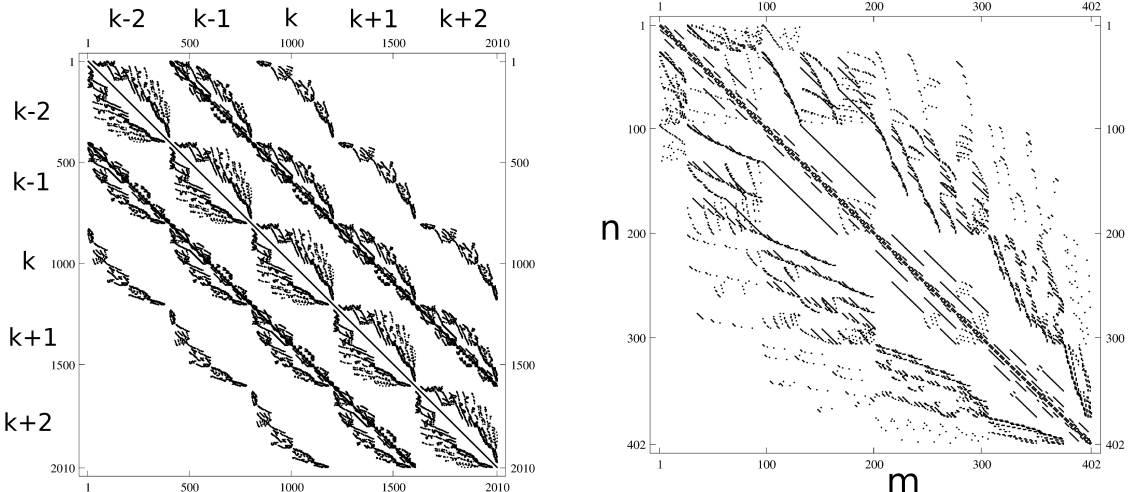


Figure B.1: Sparseness of the characteristic matrices. (left) Floquet matrix \mathcal{M}_F (see Eq. B.3) for $N/L = 5/5$. Each block with a dimension \mathcal{N}_S . (right) Hamiltonian matrix with $t = 0$ (ref. Hamiltonian) for the same system in the left panel.

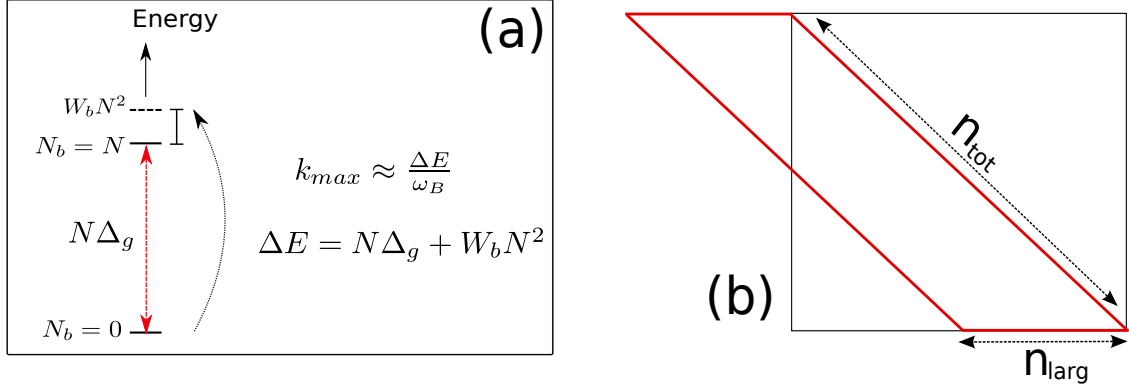


Figure B.2: (a) Banded Lanczos matrix used for diagonalization.

Numerical implementation

As seen previously, the Floquet matrix is a large sparse array, as shown in Fig. B.1-(left) for $N/L = 5/5$, with $\mathcal{N}_s = 402$. The dimension of $\mathcal{M}_F^{(2)}$

$$n_{tot} = \mathcal{N}_s(k_{max} - k_{min} + 1), \quad (\text{B.12})$$

where k_{min} and k_{max} are the number of left and right Fourier components needed to get M convergent eigenenergies into the Floquet zone, i.e. $M = \mathcal{N}_s$. We can estimate k_{max} by using the maximal diagonal element of the Hamiltonian \hat{H}_0 , which is the gap $N\Delta_g$ plus a correction given by the energy of the upperband state with the total particle number N particles in a single lattice site, i.e. $\sim W_b N^2$ (see Fig. B.2-(a)). Therefore, we define k_{max} as the number of Floquet zone needed to get a transition from the lowest diagonal element of \hat{H}_0 to the maximal one. This reads

$$k_{max} \approx \frac{N\Delta_g + W_b N^2}{\omega_B}, \quad k_{min} = - \left[\frac{k_{max}}{n} \right], \quad n = 1, \dots, 5., \quad (\text{B.13})$$

where $[\dots]$ stands for the interger part function. Note that k_{min} and k_{max} does not have to be equals to get very good convergence, which is an advantage when diagonalizing larger system, especially for smaller values of the Stark force since $k_{max} \sim 1/F$.

The Lanczos algorithm implementation needs an additional transformation of \mathcal{M}_F , which is done as follows

$$A_r(n_{larg} + j - i, i) = \text{Re}(\mathcal{M}_F)_{i,j}, \quad A_i(n_{larg} + j - i, i) = \text{Im}(\mathcal{M}_F)_{i,j}, \quad (\text{B.14})$$

thus the routine takes only into account the information into the banded lower diagonal as sketched in Fig. B.2-(b). The memory storage MS is given by the formula

$$MS = \frac{n_{tot} n_{larg} \times 16}{10^9}, \quad (\text{B.15})$$

where $n_{larg} = 3\mathcal{N}_s$ is the lateral size of the Lanczos matrix. The table B.2 shows MS for different system with fixed Stark force F , V_0 and s_0 .

We have seen that the numerical implementation of the Floquet-Lanczos routine has very good advantages as we summarize now:

B. Floquet-Lanczos Diagonalization

N/L	\mathcal{N}_s	k_{max}	k_{min}	n_{tot}	MS (GB)
7/4	858	7	1	7722	0.32
6/5	1001	6	1	8008	0.38
7/5	2288	7	1	20592	2.26
5/9	2926	5	1	20482	2.88
9/4	2860	9	2	34320	4.71
7/8	21318	7	1	191862	196.33
6/11	26910	6	1	215280	278.07
9/7	71060	9	2	852720	2908.53

Table B.1: Memory storage (MS) different N/L systems needed for computing \mathcal{N}_s eigenenergies into the Floquet zone. Here $F_r = 0.42$, with $r = 1$, $V_0 = 5$ and $s_0 = 1$.

1. Fast convergence since the dimension of the Krylov subspace (n_{lancz}) needed to compute the convergent eigenenergies is smaller than the dimension of the matrix \mathcal{M}_F . In most of the cases by setting $n_{lancz} \approx 3\mathcal{N}_s$ we can get the complete spectrum into the Floquet zone. This also depends on the position in the spectrum ε_0 for the initialization of the algorithm. This can be set using the physical concepts of the current problem, for instance, by setting ε_0 to be in the center of the energetic separation between the lowest and highest manifold, plus the energy of the lower band state with the total number of particle in the same site:

$$\varepsilon_0(F) = \frac{1}{2}W_a n(n-1) + \frac{1}{2}n\Delta_g \left(1 - \frac{F}{F_r}\right), \quad (\text{B.16})$$

with Δ_r as defined in Sec. 3.2.1.

2. It is “fully” parallelizable and the computation time is shorter compared with the integration of the evolution operator, since the time of integration is larger as the Stark force decrease. Nevertheless the memory expended gets larger in the latter regime.
3. Since the center of the Floquet zone is a predefined variable, we can used to compute the spectrum not only in one diagonalization process, but in m parallel processes which compute the whole spectrum by using the concept of n -manifold the quasi-symmetry above exposed.

Random Matrix Theory: Some Tools

C.1 Random Matrix Theory

Random matrix theory is a well-known theory that offers universal predictions of physical phenomena, which are described by Hamiltonian matrix with large degree of randomness. During the last years, it has been shown that this theory works out, especially in nuclear physics [72–74]. However, most of its measures can be implemented to analyze and characterize spectral properties of highly complex Hamiltonian system without classical analog, for instance, the Bose-Hubbard Hamiltonian which has no classical analog for few particle systems. In this appendix, we summarize the principal RMT (tools) measures used in this work in order to study the spectra properties of the two-band many-body Wannier-Stark system.

Unfolding Of The Spectrum

In order to compare the universal properties of the our system with the RMT measures, we must transform the spectrum, i.e. we must rescale it in such a way that the density of states, $\rho(E)$ is a constant. As explained in ref. [70], such a process, usually called unfolding, is possible by means of the integrated density of states $N_\rho(E)$ defined by

$$N(E) = \int_{-\infty}^E \rho(E') dE', \quad \text{with } \rho(E) = \sum \delta(E - E_n). \quad (\text{C.1})$$

and thus the unfolded energies are given by

$$\epsilon_i = N_\rho(E_i). \quad (\text{C.2})$$

The latter guarantees that the set of level spacings $\{s_i = \epsilon_{i+1} - \epsilon_i\}$ has mean value $\langle s \rangle = 1$. In the case of the Floquet spectra, this process is not necessary only if the quasienergies lie uniformly distributed over the Floquet zone ω_B . However, we have seen that the resonance width ΔE is usually smaller than ω_B , therefore an unfolding process is necessary. We use the *Lorenzian broadening method* to unfold the spectrum, for which the average density of states is defined as

$$\bar{\rho}_\gamma(E) = \frac{1}{\pi} \sum_n \frac{\gamma}{(E - E_n)^2 + \gamma^2}, \quad (\text{C.3})$$

where γ is an optimization parameter, with a minimal value $\gamma_{min} \gtrsim \langle \{s_i\} \rangle$, where $\langle \{s_i\} \rangle$ is the mean level spacing of the original spectrum.

Level Spacing Statistics

In RMT the simplest and robustest quantity is the Nearest Neighbor spacing distribution $P(\{s_i\})$. Systems with time-reversal invariance ($t \rightarrow -t$ and $p \rightarrow -p$) is known to transform under a canonical transformation

$$OHO^T = H', \quad (\text{C.4})$$

where O is an orthogonal operator, i.e. $O^{-1} = O^T$. This is the usual case of real symmetric matrices, which are part of the Gaussian Orthogonal Ensemble (GOE). Matrices that break the time-reversal symmetry transform then under unitary transformation and the ensemble is called Gaussian Unitary Ensemble (GUE). The matrix elements are complex and the matrix Hermitian. By assuming sufficient randomness of the Hamiltonian matrix, the set $\{s_i\}$ follows the RMT $P(s)$ distributions given by

$$\begin{aligned} P(s) &= \exp(-s), & (\text{Poisson}) \\ P(s) &= \frac{\pi}{2} s \exp\left(-\frac{\pi}{4} s^2\right), & (\text{GOE}) \end{aligned} \quad (\text{C.5})$$

$$P(s) = \frac{32}{\pi} s^2 \exp\left(-\frac{4}{\pi} s^2\right), \quad (\text{GUE}) \quad (\text{C.6})$$

and Intermediate regimes between the Poisson and GOE distribution are interpolated by using the empirical Brody distribution [74]

$$P(s; \omega) = \alpha(\omega + 1) s^\omega \exp(-\alpha s^{\omega+1}), \quad \alpha \equiv \left[\Gamma\left(\frac{\omega + 2}{\omega + 1}\right) \right]^{\omega+1} \quad (\text{C.7})$$

where $\omega = 0$ leads to the Poisson distribution and $\omega = 1$ results in the GOE limit, commonly called Wigner surmise.

Porter-Thomas Distribution

The eigenvectors also contain important information about the spectrum, since for a given set of eigenstates $|\varepsilon_i\rangle$'s, their projections onto an arbitrary vector of the Hilbert space follow the Porter-thomas distribution [73, 74]. For Gaussian ensemble this distributions are defined by the relations

$$\begin{aligned} P_{goe}(y) &= \frac{1}{\sqrt{2\pi y}} e^{-y/2} \\ P_{gue}(y) &= e^{-y}, \end{aligned} \quad (\text{C.8})$$

and

$$y \equiv \frac{|\langle \alpha | \varepsilon_i \rangle|^2}{\langle c^2 \rangle}, \quad \langle c^2 \rangle \equiv \langle |\langle \alpha | \varepsilon_i \rangle|^2 \rangle. \quad (\text{C.9})$$

$\langle \dots \rangle$ stands for the mean value of the projections. Mean values of the localization measures are computed in the main text are given by the formulae

$$\xi = \mathcal{N}_s \langle c^2 \rangle^2 \int_0^\infty dy P(y) y^2, \quad (\text{C.10})$$

C. Random Matrix Theory: Some Tools

and

$$S_{\text{sh}} = \mathcal{N}_s \int_0^\infty dy P(y) y \langle c^2 \rangle \ln(y \langle c^2 \rangle), \quad (\text{C.11})$$

keeping in mind that the \mathcal{N}_s is the dimension of the Hilbert space. In case of complete delocalization the coefficients fluctuate about $\langle c^2 \rangle = 1/\mathcal{N}_s$, and the corresponding values of the measures defined in the above equations are given by

$$\xi_{\text{goe}}^{-1} = 3/\mathcal{N}_s, \quad \xi_{\text{gue}}^{-1} = 2/\mathcal{N}_s \quad (\text{C.12})$$

and

$$S_{\text{sh}}^{\text{goe}} = \ln(0.48\mathcal{N}_s), \quad S_{\text{sh}}^{\text{gue}} = \ln(\mathcal{N}_s) - \gamma_c, \quad \text{with } \gamma_c = 0.422784\dots \quad (\text{C.13})$$

Avoided Crossings widths Statistics

In chapter 3.2 we study the importance of the manifold mixing and the density of ACs about and between the resonance position. The avoided crossings structure is robust in the many-body regime, then the ACs width distribution $P(c)$ [30, 105, 141–143] in the vicinity of F_r becomes very useful to characterize locally quantum chaotic regimes. The distribution $P(c)$ is computed for the 2×2 matrix Hamiltonian, for which the energy levels repel each other at the AC value of the free parameter λ [141]. The Hamiltonian $H_{2 \times 2}$ reads

$$H = \begin{pmatrix} a + \lambda v_1 & g \\ g & b + \lambda v_2 \end{pmatrix},$$

an after the normalization $\langle c \rangle = 1$ and $\int P(c) dc = 1$, the RMT predicts the distribution

$$P(c) = \frac{2}{\pi} \exp\left(-\frac{c^2}{\pi}\right), \quad \text{for GOE ensembles.} \quad (\text{C.14})$$

For nearly integrable systems $P(c)$ is approximated a delta function $\delta(c)$, then intermediated regime must follows the distribution [105]

$$P(C) = (1 - \gamma)\delta(C - C_0) + \gamma \left(\frac{4D}{\pi}\right)^{1/2} \exp(-DC^2), \quad \text{with } D = \frac{\gamma}{\langle C \rangle^2 \pi}. \quad (\text{C.15})$$

Number Variance

Another measure of correlations between energy levels is the so-called number variance defined by

$$\Sigma^2(L) = \langle (N(\epsilon_0, L) - L)^2 \rangle_{\epsilon_0} \quad (\text{C.16})$$

where L is the an energy interval and the energy levels taking into account are those already unfolded. This quantity is a fluctuation measure that contains information about long-range correlations [70, 74]. This function is also called the "spectral rigidity" and for GOE spectra grows propotional to $\ln(2\pi L)$ and for poissonian-distributed spectra it is just a linear function of L

$$\begin{aligned} \Sigma^2(L) &= L, \quad \text{Poisson ensembles} \\ \Sigma^2(L) &= \frac{2}{\pi^2} \left(\ln(2\pi L) + \gamma + 1 - \frac{1}{8}\pi^2 \right), \quad \text{GOE.} \end{aligned} \quad (\text{C.17})$$

AC Detection by Fidelity Change

In this appendix, we present the basis of the method used in ref. [30, 81] to characterize quantum spectra with high degree of level repulsion. The method is based on the concept of quantum *fidelity*. We show how avoided crossings can be detected in the framework of the Floquet theory, described in detail in App. B.2. This is an alternative method in comparison with the method exposed in Chapter 3, which is based on the fidelity of probability vectors. The boundary conditions plays a an important role for the implementation of this method that in case of quasienergies an explicit ordering of the of the spectrum is needed, which is not straight forward set.

D.1 Fidelity Change

Let us then introduce the method by following the development done in ref. [81]. The fidelity function is defined by the expression

$$f_n(\lambda, \delta\lambda) \equiv |\langle \varepsilon_n(\lambda) | \varepsilon_n(\lambda + \delta\lambda) \rangle|, \quad (\text{D.1})$$

where

$$\hat{H}(\lambda) |\varepsilon_n(\lambda)\rangle = \varepsilon_n(\lambda) |\varepsilon_n(\lambda)\rangle, \quad \hat{H}(\lambda + \delta\lambda) |\varepsilon_n(\lambda + \delta\lambda)\rangle = \varepsilon_n(\lambda + \delta\lambda) |\varepsilon_n(\lambda + \delta\lambda)\rangle \quad (\text{D.2})$$

The detection of avoided crossing is made by the *fidelity change* function defined by

$$S_n(\lambda, \delta\lambda) \equiv \frac{1 - f_n(\lambda, \delta\lambda)}{(\delta\lambda)^2}, \quad (\text{D.3})$$

where in the limit $\delta\lambda \ll 1$, this quantity does not dependent on $\delta\lambda$. The eigenstate $|\varepsilon_n(\lambda + \delta\lambda)\rangle$ is expanded up to second order of perturbation theory, which reduces the fidelity change to

$$S_n(\lambda) = \frac{1}{2} \sum_{n \neq m} \frac{|\langle \varepsilon_m(\lambda) | \hat{V} | \varepsilon_n(\lambda) \rangle|^2}{[\varepsilon_m - \varepsilon_n]^2}. \quad (\text{D.4})$$

Now the question is how to define \hat{V} . Back to the equation (B.3), i.e. the Floquet matrix to be diagonalized, one can rewrite the Eq. D.4 in terms of $\lambda + \delta\lambda$. By recognizing $\lambda \equiv F$ and regarding only the largest dipole-induced transition C_0 , we obtain the expression

$$(\mathbf{H}_0(F + \delta F) - 2\pi K(F + \delta F) \hat{\mathbf{1}}) |\phi_{\varepsilon_n}^K\rangle + \mathbf{J} |\phi_{\varepsilon_n}^{K-1}\rangle + \mathbf{J}^\dagger |\phi_{\varepsilon_n}^{K+1}\rangle = \varepsilon_n \hat{\mathbf{b}} |\phi_{\varepsilon_n}^K\rangle, \quad (\text{D.5})$$

where $\mathbf{H}_0(F + \delta F) = \mathbf{H}'_0 + \delta F \mathbf{V}$ is the time-independent Hamiltonian. In this way the equation (D.5) can be rewritten as

$$(\mathbf{H}'_0 - KF\hat{\mathbf{I}})|\phi_{\varepsilon_n}^K\rangle + 2\pi\delta F(\mathbf{V} - K\hat{\mathbf{I}})|\phi_{\varepsilon_n}^K\rangle + \mathbf{J}|\phi_{\varepsilon_n}^{K-1}\rangle + \mathbf{J}^\dagger|\phi_{\varepsilon_n}^{K+1}\rangle = \varepsilon_n\hat{\mathbf{I}}|\phi_{\varepsilon_n}^K\rangle, \quad (\text{D.6})$$

therefore, we can define $\hat{\mathbf{V}} = \mathbf{V} - K\hat{\mathbf{I}}$, with \mathbf{V} defined as in Eq. (3.1) as

$$\mathbf{V} = \omega_B C_0 \sum_l \left(a_l^{(2)\dagger} \hat{a}_l + h.c. \right) \mathbb{1}. \quad (\text{D.7})$$

The term K in $\hat{\mathbf{V}}$ can be neglected without loss of generality, since $\langle \varepsilon_m | \mathbf{V} | \varepsilon_n \rangle \gg \langle \varepsilon_m | K | \varepsilon_n \rangle$ about a local AC, i.e. $S_n \rightarrow 0$ in region where any AC occurs. Finally, the expression (D.4) can be transformed in term of the eigenstates of the Floquet Hamiltonian as follows

$$S_n(F) = \frac{1}{2} \sum_{m \neq n} \frac{|\sum_{\alpha, \alpha'} \tilde{c}_{\alpha'}^{\varepsilon_n} \tilde{c}_{\alpha'}^{\varepsilon_m} \tilde{V}_{\alpha, \alpha'}|^2}{[\varepsilon_m - \varepsilon_n]^2} \quad (\text{D.8})$$

where $\tilde{c}_{\alpha'}^{\varepsilon_n} = \sum_K c_{\alpha'}^{K, \varepsilon_n}$ and $\tilde{V}_{\alpha, \alpha'} = \langle s_{\alpha} | \mathbf{V} | s_{\alpha'} \rangle$. In figure D.1 we show a simple example of the implementation of this method. For more details about the properties of the fidelity change we suggest ref. [30]

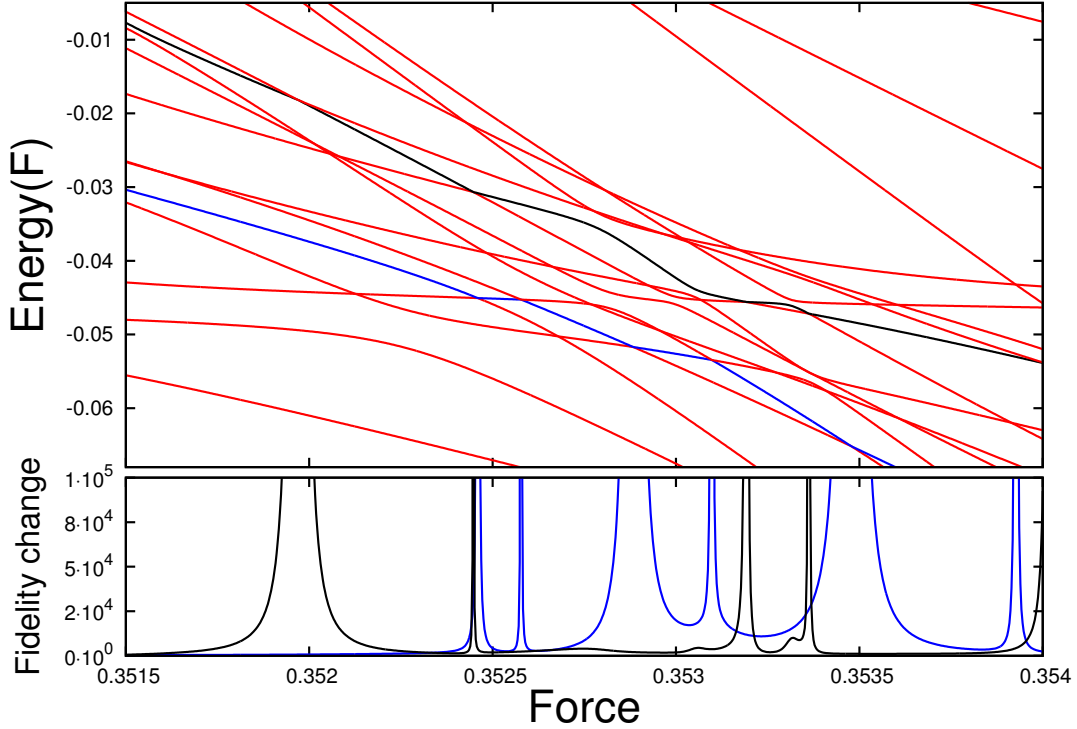


Figure D.1: Fidelity change as function of F for $N/L = 3/3$, with $V_0 = 5$ and $s_0 = 1$. The peaks represent the position of the avoided crossing occurs. The maxima of the fidelity change function and the respective width of the lorezian peaks are related to the AC width as shown in ref. [30].

Bibliography

- [1] S. N. Bose. *Z. Phys.*, **26**:178, 1924.
- [2] A. Einstein. *Sitzungsber. preuss. Akad. Wiss.*, **1**:3, 1925.
- [3] M. H. Anderson, J. R. Ensher, M. R. Matthews, C. E. Wieman, and E. A. Cornell. *Science*, **269**:198–201, Jul 1995.
- [4] W. Petrich, M. H. Anderson, J. R. Ensher, and E. A. Cornell. *Phys. Rev. Lett.*, **74**:3352–3355, Apr 1995.
- [5] K. B. Davis, M. O. Mewes, M. R. Andrews, N. J. van Druten, D. S. Durfee, D. M. Kurn, and W. Ketterle. *Phys. Rev. Lett.*, **75**:3969–3973, Nov 1995.
- [6] C. C. Bradley, C. A. Sackett, and R. G. Hulet. *Phys. Rev. Lett.*, **78**:985–989, Feb 1997.
- [7] I. Bloch, J. Dalibard, and W. Zwerger. *Rev. Mod. Phys.*, **80**:885–964, Jul 2008.
- [8] A. J. Leggett. *Rev. Mod. Phys.*, **73**:307, 2001.
- [9] O. Morsch and M. Oberthaler. *Rev. Mod. Phys.*, **78**:179–215, Feb 2006.
- [10] M. Bason, M. Viteau, N. Malossi, P. Huillery, E. Arimondo, D. Ciampini, R. Fazio, V. Giovannetti, R. Mannella, and O. Morsch. *Nat. Phys.*, **8**:147, 2011.
- [11] R. P. Feynman. *International Journal of Theoretical Physics*, **21**:467–488, Jun. 1982.
- [12] D. Jaksch, C. Bruder, J. I. Cirac, C. W. Gardiner, and P. Zoller. *Phys. Rev. Lett.*, **81**:3108–3111, Oct 1998.
- [13] M. Greiner, O. Mandel, T. Esslinger, T.W. Hänsch, and I. Bloch. *Nature*, **415**:39, 2002.
- [14] K. Kim, M.-S. Chang, S. Korenblit, R. Islam, E. E. Edwards, J. K. Freericks, G.-D. Lin, L.-M. Duan, and C. Monroe. *Nature*, **465**:590–593, Aug 2010.
- [15] M. Aidelsburger, M. Atala, S. Nascimbène, S. Trotzky, Y.-A. Chen, and I. Bloch. *Phys. Rev. Lett.*, **107**:255301, Dec 2011.
- [16] M. Endres, T. Fukuhara, D. Pekker, M. Cheneau, P. Schauß, C. Gross, E. Demler, S. Kuhr, and Bloch I. *Nature*, **487**:454–458, 2012.
- [17] A. Polkovnikov. *Phys. Rev. B*, **72**:161201–1(R), Oct 2005.
- [18] W. Wilkinson. *J. Phys. A: Math. Gen.*, **21**:4021, Nov. 1988.

- [19] M. Hiller, H. Venzl, T. Zech, B. Oleś, F. Mintert, and A. J. *Phys. B: At. Mol. Opt. Phys.*, **45**:095301, 2012.
- [20] C. A. Parra-Murillo, J. Madroñero, and S. Wimberger. *arXiv:1207.4699 [cond-mat.quant-gas]*, 2012.
- [21] A. R. Kolovsky. *Europhys. Lett.*, **68**:632, Dec 2004.
- [22] R. Marcos, D Vanja, and M. Olshanii. *Nature*, **452**:854–858, Jan 2012.
- [23] M. Rigol and M. Srednicki. *Phys. Rev. Lett.*, **108**:110601, Mar 2012.
- [24] J. M. Deutsch. *Phys. Rev. A*, **43**:2046–2049, Feb 1991.
- [25] G. Wirth, M. Ölschläger, and A. Hemmerich. *Nature Phys.*, **7**:147, Aug 2011.
- [26] T. Müller, S. Fölling, A. Widera, and I. Bloch. *Phys. Rev. Lett.*, **99**:200405, Nov 2007.
- [27] T. Gericke, P. Würtz, D. Reitz, T. Langen, and H. Ott. *Nat. Phys.*, **4**:949, 2008.
- [28] P. Würtz, T. Langen, T. Gericke, A. Koglbauer, and H. Ott. *Phys. Rev. Lett.*, **103**:080404, 2009.
- [29] G. Barontini, R. Labouvie, F. Stubenrauch, A. Vogler, V. Guarrera, and H. Ott. *Phys. Rev. Lett.*, **110**:035302, Jan 2013.
- [30] P. Plötz, M. Lubasch, and S. Wimberger. *Physica A*, **390**:1363, 2011.
- [31] D. Witthaut, F. Trimborn, H. Hennig, G. Kordas, T. Geisel, and S. Wimberger. *Phys. Rev. A*, **83**:063608, 2011.
- [32] F. Trimborn, D. Witthaut, H. Hennig, G. Kordas, T. Geisel, and S. Wimberger. *Eur. Phys. J. D*, **63**:63, 2011.
- [33] T. Rom, T. Best, O. Mandel, A. Widera, M. Greiner, Th. W. Hänsch, and I. Bloch. *Phys. Rev. Lett.*, **93**:073002, Aug 2004.
- [34] J. G. Danzl, M. J. Mark, E. Haller, M. Gustavsson, R. Hart, J. Aldegunde, J. M. Hutson, and H. C. Nägerl. *Nat. Phys.*, **6**:265–270, Feb. 2010.
- [35] T. Sowiński, O. Dutta, P. Hauke, L. Tagliacozzo, and M. Lewenstein. *Phys. Rev. Lett.*, **108**:115301, Mar 2012.
- [36] C. Sherson, J. F. Weitenberg, M. Endres, , T. Cheneau, I. Bloch, and S. Kuhr. *Nature Letters*, **467**:68, Sep. 2010.
- [37] R. J. Donnelly. *Physics Today*, **48**:30–36, 1995.
- [38] J. C. Pethick and Smith H. *Bose-Einstein Condensation in Dilutes Gases*. Cambridge University Press, Cambridge, 2001.
- [39] O. Penrose and L. Onsager. *Phys. Rev.*, **104**:574, 1956.
- [40] H. Feshbach. *Phys.*, **5**:357, 1958.

- [41] Rekishu Yamazaki, Shintaro Taie, Seiji Sugawa, Katsunari Enomoto, and Yoshiro Takahashi. *Phys. Rev. A*, 87:010704, Jan 2013.
- [42] R. B. Diener, G. A. Georgakis, J. Zhong, M. Raizen, and Q. Niu. *Phys. Rev. A*, **64**:033416, Aug 2001.
- [43] A. R. Kolovsky. *Phys. Rep.*, **366**:103, 2002.
- [44] F. Bloch. *Zeitschrift für Physik*, **52**:555–600, 1929.
- [45] N. W. Ashcroft and N. D. Mermin. *Solid State Physics*. Orlando: Harcour, 2 edition edition, 1976.
- [46] G. H. Wannier. *Phys. Rev.*, **52**(3):191–197, Aug 1937.
- [47] W. Kohn. *Phys. Rev. B*, **7**(10):4388–4398, May 1973.
- [48] W. Kohn. *Phys. Rev.*, **115**(4):809–821, Aug 1959.
- [49] N. Marzari and D. Vanderbilt. *Phys. Rev. B*, **56**:12847–12865, Nov 1997.
- [50] I. Souza, N. Marzari, and D. Vanderbilt. *Phys. Rev. B*, **65**:035109, Dec 2001.
- [51] B. L. Altshuler, Y. Gefen, A. Kamenev, and L. S. Levitov. *Phys. Rev. Lett.*, **78**:2803–2806, Apr 1997.
- [52] F. M. Izrailev. *Physica Scripta*, **T90**:95–104, Aug. 2001.
- [53] V. V. Flambaum and F. M. Izrailev. *Phys. Rev. E*, **61**:2539, Dec. 2000.
- [54] P. W. Anderson. *Basic Notions Of Condensed Matter Physics*. Westview Press / Addison-Wesley, 2 edition edition, 1997.
- [55] P. W. Anderson. *Phys. Rev.*, **109**:1492–1505, Mar 1958.
- [56] A. Zenesini, H. Lignier, G. Tayebirad, J. Radogostowicz, D. Ciampini, R. Mannella, S. Wimberger, O. Morsch, and E. Arimondo. *Phys. Rev. Lett.*, **103**:090403, Aug 2009.
- [57] E. Haller, R. Hart, M. J. Mark, J. G. Danzl, L. Reichsöllner, and H. C. Nägerl. *Phys. Rev. Lett.*, **104**:200403, May 2010.
- [58] A. Tomadin. *Quantum Chaos with Ultracold Atoms in Optical Lattices*. Diploma Thesis, Pisa University, Italy, 2005.
- [59] A. R. Kolovsky and A. Buchleitner. *Phys. Rev. E*, **68**:056213, Nov 2003.
- [60] J. Simon, S. Bakr, M. Ruichao, M. E. Tai, M. Preiss, and M. Greiner. *Nature*, **472**:307, Apr 2011.
- [61] S. Sachdev, K. Sengupta, and S. M. Girvin. *Phys. Rev. B*, **66**:075128, Aug 2002.
- [62] P. Plötz, P. Schlagheck, and S. Wimberger. *Eur. Phys. J. D*, **63**:47, 2011.

- [63] M. Ben Dahan, E. Peik, J. Reichel, Y. Castin, and C. Salomon. *Phys. Rev. Lett.*, **76**:4508–4511, Jun 1996.
- [64] P. Plötz, J. Madroñero, and S. Wimberger. *J. Phys. B: At. Mol. Opt. Phys.*, **43**:081001, Mar 2010.
- [65] M. Holthaus. *J. Opt. B.: Quantum Semiclass. Opt.*, **2**:589–604, 2000.
- [66] A. Zenesini, H. Lignier, G. Tayebirad, J. Radogostowicz, D. Ciampini, R. Mannella, S. Wimberger, O. Morsch, and E. Arimondo. *Phys. Rev. Lett.*, **103**:090403, Aug 2009.
- [67] C. Sias, A. Zenesini, H. Lignier, S. Wimberger, D. Ciampini, O. Morsch, and E. Arimondo. *Phys. Rev. Lett.*, **98**:120403, Mar 2007.
- [68] N. Lörch, F. V. Pepe, H. Lignier, D. Ciampini, R. Mannella, O. Morsch, E. Arimondo, P. Facchi, G. Florio, S. Pascazio, and S. Wimberger. *Phys. Rev. A*, **85**:053602, May 2012.
- [69] M. Olshanii. *Phys. Rev. Lett.*, **81**:938–941, Aug 1998.
- [70] F. Haake. *Quantum signatures of chaos*. Springer series, second edition edition, 1991.
- [71] F. Tabor. *Chaos and Integrability in Nonlinear Dynamics*. John Wiley & Sons, 1989.
- [72] O. Bohigas, M. J. Giannoni, and C. Schmit. *Phys. Rev. Lett.*, **52**:1–4, Jan 1984.
- [73] C. E. Porter and R. G. Thomas. *Phys. Rev.*, **104**:483–491, Oct 1956.
- [74] G. E. Mitchell, A. Richter, and H. A. Weidenmüller. *Rev. Mod. Phys.*, **82**:2845–2901, Oct 2010.
- [75] A. Tomadin, R. Mannella, and S. Wimberger. *Phys. Rev. Lett.*, **98**:130402, Mar 2007.
- [76] J. D. Bodyfelt, M. Hiller, and T. Kottos. *Eur. Phys. Lett.*, **78**:50003, 2007.
- [77] M. Hiller, T. Kottos, and T. Geisel. *Phys. Rev. A*, **79**:023621, Feb 2009.
- [78] C. Kollath, G. Roux, G. Biroli, and A. M. Läuchli. *J. Stat. Mech.*, **78**:p08011, 2010.
- [79] F. Meinert, M. J. Mark, E. Kirilov, K. Lauber, P. Weinmann, A. D. Daley, and H.-C Nägerl. *arXiv:1304.2628 [cond-mat.quant-gas]*, 2013.
- [80] F. Dalfovo, S. Giorgini, L. P. Pitaevskii, and S. Stringari. *Rev. Mod. Phys.*, **71**:463, 1999.
- [81] P. Plötz. *Complex dynamics of ultracold atoms*. PhD Thesis, Heidelberg University, Germany, 2010.
- [82] T. Salger, C. Geckeler, Sebastian Kling, and M. Weitz. *Phys. Rev. Lett.*, **99**:190405, Nov 2007.
- [83] S. Kling, T. Salger, C. Grossert, and M. Weitz. *Phys. Rev. Lett.*, **105**:215301, Nov 2010.
- [84] A. Zenesini, D. Ciampini, O. Morsch, and E. Arimondo. *Phys. Rev. A*, **82**:065601, Dec 2010.
- [85] D. Witthaut, F. Trimborn, V. Kegel, and H. J. Korsch. *Phys. Rev. A*, **83**:013609, Jan 2011.

- [86] B. M. Breid, D. Witthaut, and H. J. Korsch. *New J. Phys.*, **9**:62, Mar 2007.
- [87] P. Plötz and S. Wimberger. *Eur. Phys. Jour. D*, **65**:199, Nov 2011.
- [88] B. E. Sherlock, M. Gildemeister, E. Owen, E. Nugent, and C. J. Foot. *Phys. Rev. A*, **83**:043408, Apr 2011.
- [89] A. Ramanathan, K. C. Wright, S. R. Muniz, M. Zelan, W. T. Hill, C. J. Lobb, K. Helmerson, W. D. Phillips, and G. K. Campbell. *Phys. Rev. Lett.*, **106**:130401, Mar 2011.
- [90] K. C. Wright, R. B. Blakestad, C. J. Lobb, W. D. Phillips, and G. K. Campbell. *Phys. Rev. Lett.*, **110**:025302, Jan 2013.
- [91] J. D. Pritchard, A. N. Dinkelaker, A. S. Arnold, P. F. Griffin, and E. Riis. *New J. Phys.*, **14**:103047, Oct 2012.
- [92] A. L. Gaunt and Z. Hadzibabic. *Scientific Reports*, **2**:721, 2011.
- [93] S. Trotzky, Y.-A. Chen, A. Flesch, I. McCulloch, U. Schollwöck, J. Eisert, and I. Bloch. *Nat. Phys.*, **8**:325, 2012.
- [94] U. Schollwöck. *Rev. Mod. Phys.*, **77**:259–315, Apr 2005.
- [95] A. Eckardt and M. Holthaus. *Phys. Rev. Lett.*, **101**:245302, Dec 2008.
- [96] A. Eckardt, C. Weiss, and M. Holthaus. *Phys. Rev. Lett.*, **95**:260404, Dec 2005.
- [97] A. Isacson and S. M. Girvin. *Phys. Rev. A*, **72**:053604, Nov 2005.
- [98] W. V. Liu and C. Wu. *Phys. Rev. A*, **74**:013607, Jul 2006.
- [99] F. Serwane, G. G. Zürn, T. Lompe, T. B. Ottenstein, A. N. Wenz, and S. Jochim. *Science*, **332**, Apr. 2011.
- [100] A. Tomadin, R. Mannella, and S. Wimberger. *Phys. Rev. A*, **77**:013606, Jan 2008.
- [101] J. H. Shirley. *Phys. Rev.*, **138**:B979–B987, May 1965.
- [102] M. Kuś. *Journal of Modern Optics*, **49**(12):1979–1985, Feb 2002.
- [103] T. Dittrich and U. Smilansky. *Nonlinearity*, **4**:54, 1991.
- [104] B. Georgeot and D. L. Shepelyansky. *Phys. Rev. E*, **62**:3504–3507, Sep 2000.
- [105] X. Yang and J. Burgdörfer. *Phys. Rev. A*, **48**(1):83–87, Jul 1993.
- [106] T. Kato. *J. Phys. Soc. Jpn.*, **5**:435–439, 1950.
- [107] D. A. Harmin. *Phys. Rev. A*, **44**:433–461, Jul 1991.
- [108] Y. N. Demkov and V. N. Ostrovsky. *J. Phys. B: At. Mol. Opt. Phys.*, **34**:2419, Apr 2001.
- [109] A. V. Shytov. *Phys. Rev. A*, **70**:052708, Nov 2004.
- [110] L. F. Santos, F. Borgonovi, and F. M. Izrailev. *Phys. Rev. Lett.*, **108**:094102, Mar 2012.

- [111] L. F. Santos, F. Borgonovi, and F. M. Izrailev. *Phys. Rev. E*, **85**:036209, Mar 2012.
- [112] G. Breit and E. Wigner. *Phys. Rev.*, **49**:519–531, Apr 1936.
- [113] X.-P. Wang M. Klein, D. Robert. *Communications in Mathematical Physics*, **131**:109–124, Jul 1990.
- [114] F. I. Fisher. *Statistical Analysis of Circular Data*. Cambridge University Press, 1996.
- [115] I. Rotter. *J. Phys. A*, **42**:153001, 2009.
- [116] H. P. Breuer and F. Petruccione. *The theory of open quantum systems*. Oxford University Press, Oxford, 2007.
- [117] D. F. Walls and G. J. Milburn. *Quantum optics*. Springer, Heidelberg, 1995.
- [118] A. Laucht, N. Hauke, J. M. Villas-Bôas, F. Hofbauer, G. Böhm, M. Kaniber, and J. J. Finley. *Phys. Rev. Lett.*, **103**:087405, Aug 2009.
- [119] J. P. Reithmaier, B. Sk, A. Löffler, C. Hofmann, S. Kuhn, S. Reitzenstein, L. V. Keldysh, V. D. Kulakovskii, T. L. Reinecke, and A. Forchel. *Nature (London)*, **432**:197–200, Nov. 2004.
- [120] J. R. Taylor. *Scattering theory: the quantum theory on nonrelativistic collisions*. Wiley, New York, 1972.
- [121] S. Wimberger, C. A. Parra-Murillo, and G. Kordas. *J. Phys. Conf. Series, in press*, 2013.
- [122] J. F. Sherson, C. Weitenberg, M. Endres, M. Cheneau, I. Bloch, and S. Kuhr. *Nature*, **467**, 2010.
- [123] D. Witthaut, F. Trimborn, and S. Wimberger. *Phys. Rev. Lett.*, **101**:200402, 2008.
- [124] D. Witthaut, F. Trimborn, and S. Wimberger. *Phys. Rev. A*, **79**:033621, 2009.
- [125] G. Kordas, S. Wimberger, and D. Witthaut. *Eur. Phys. Lett.*, **100**:30007, 2012.
- [126] J. Anglin. *Phys. Rev. Lett.*, **79**:6, 1997.
- [127] S. Flach and A. V. Gorbach. *Phys. Rep.*, (**467**) **1**, 2008.
- [128] B. Misra and E. C. G. Sudarshan. *J. Stat. Mech.*, **18**:756, 1977.
- [129] M. Srednicki. *Phys. Rev. E*, **50**:888–901, Aug 1994.
- [130] S. Goldstein, J. L. Lebowitz, R. Tumulka, and N. Zanghì. *Phys. Rev. Lett.*, 96:050403, Feb 2006.
- [131] J. Berges, Sz. Borsányi, and C. Wetterich. *Phys. Rev. Lett.*, 93:142002, Sep 2004.
- [132] E. Persson, I. Rotter, H. J. Stöckmann, and M. Barth. *Phys. Rev. Lett.*, **85**:2478, 2000.
- [133] M. P. A. Fisher, P. B. Weichman, G. Grinstein, and D. S. Fisher. *Phys. Rev. B*, **40**:546–570, Jul 1989.

- [134] M. Olshanii. *Phys. Rev. Lett.*, **81**(5):938–941, Aug 1998.
- [135] A. Buchleitner, D. Delande, and J.-C. Gay. *JOSA B*, **12**(4):505–519, Apr 1995.
- [136] J. Madro nero. *Spectral properties of planar helium under periodic driving*. PhD Thesis, Ludwig-Maximilians-Universität München, Germany, 2004.
- [137] T.-S. Ho and S.-I. Chu. *Phys. Rev. A*, **31**:659–676, Feb 1985.
- [138] C. J. Lanczos. *Res. Nat. Bur. Standards, Sect. B*, **45**:225, 1950.
- [139] A. Krug. *Alkali Rydberg states in electromagnetic fields: computational physics meets experiment*. Ludwig-Maximilians-Universität München, Germany, 2001.
- [140] B. N. Parlett and D. S. Scott. *Math. Compu.*, **33**:217–238, 1979.
- [141] J. Zakrzewski and M. Kuś. *Phys. Rev. Lett.*, **67**(20):2749–2752, Nov 1991.
- [142] C. Poli, B. Dietz, O. Legrand, F. Mortessagne, and A. Richter. *Phys. Rev. E*, **80**:035204, Sep 2009.
- [143] B. Dietz, A. Heine, A. Richter, O. Bohigas, and P. Leboeuf. *Phys. Rev. E*, **73**:035201, Mar 2006.